ANALYSIS OF THE UNWIND SECTION OF AN INDUSTRIAL WEB PROCESSING LINE

By

BENJAMIN PACINI

Bachelor of Science Mechanical and Aerospace Engineering
University of Colorado at Colorado Springs
Colorado Springs, CO, USA
2008

Submitted to the Faculty of the
Graduate College of
Oklahoma State University
in partial fulfillment of
the requirements for
the Degree of
MASTER OF SCIENCE
July, 2011

ANALYSIS OF THE UNWIND SECTION OF AN INDUSTRIAL WEB PROCESSING LINE

Thesis Approved:

Dr. Prabhakar R. Pagilla

Thesis Advisor

Dr. Gary E. Young

Committe Member

Dr. Lawrence L. Hoberock

Committe Member

Dr. Mark E. Payton

Dean of the Graduate College

ACKNOWLEDGMENTS

There are several people I would like to thank for their contributions to my thesis. First and foremost I would like to express my greatest appreciation to my advisor Dr. Prabhakar R. Pagilla for his invaluable guidance, supervision, and friendship throughout my graduate studies. I am extremely grateful for his support, encouragement, and technical insights.

I would like to extend my thanks to my master's committee members: Dr. Gary E. Young for his friendship and guidance throughout my graduate studies and Dr. Lawrence L. Hoberock for his support and suggestions in completion of this work. Their guidance and understanding made the development of this thesis a positive learning experience.

I would also like to thank my colleagues at Oklahoma State University: Pramod Raul, Muthappa Ponjanda-Madappa, Youwei Lu, Kadhim Jabbar, Shyam Konduri, Mauro Cimino, Carlo Branca, Aravind Seshadri, and Supraj Paleti. Their friendship and support (both technical and moral) have been an essential part of my graduate studies.

I owe a special debt of gratitude to Jamie Lynch, Tim Gottlob, and the other employees at Armstrong World Industries for their invaluable assistance throughout the duration of this project. Additionally, I would like to thank the Oklahoma Center for the Advancement of Science and Technology (OCAST) and the National Science Foundation (NSF) for their funding throughout the project.

TABLE OF CONTENTS

LIST OF TABLES

LIST OF FIGURES

NOMENCLATURE

Chapters 2 and 3

A	Cross sectional area of the web
b	Damping constant in Maxwell element
b_w	Lateral width of the web
d_x	Dancer 1 trim
E	Spring constant in Maxwell element
E_v	Spring constant in Maxwell element
F	Force applied to keep Dancer 1 vertical
F_c	Interaction force between accumulator carriage and motor
F_{gc}	Gravitational force of accumulator carriage and rollers
g	Acceleration due to gravity
J_i	Inertia of element i
J_c	Equivalent inertia of accumulator motor, gears, carriage, and rollers
J_{mc}	Inertia of accumulator motor
$K_{i,UW}$	Integral PI gain
$K_{p,UW}$	Proportional PI gain
$K_{d,D1}$	Derivative gain of Dancer 1 PID
$K_{i,AC}$	Integral gain of accumulator speed loop PI
$K_{i,D1}$	Integral gain of Dancer 1 PID
$K_{i,PR1}$	Integral gain of Pull Roll 1 speed loop PI
$K_{i,PR2}$	Integral gain of Pull Roll 2 speed loop PI

$K_{p,AC}$	Proportional gain of accumulator speed loop PI
$K_{p,D1}$	Proportional gain of Dancer 1 PID
$K_{p,PR1}$	Proportional gain of Pull Roll 1 speed loop PI
$K_{p,PR2}$	Proportional gain of Pull Roll 2 speed loop PI
K_{pm}	Scale factor used during manual control for the Unwind Roll
k_n	Unit conversion from Control Variable to brake pressure
l	Length from the dancer pivot to the dancer roller center
l_F	Length from the dancer pivot to the point where F is applied
L_i	Length of span i
l_L	Length from the dancer pivot to the center of gravity of the dancer lever arm
l_x	Length from the dancer pivot to the point where dancer linear displacement is measured
$MAXI$	Maximum process variable
$MINI$	Minimum process variable
$MAXS$	Maximum engineering unit scaling value
$MINS$	Minimum engineering unit scaling value
$MAXCV$	Maximum control variable
$MINCV$	Minimum control variable
m_c	Mass of accumulator carriage
n	Number of stress measurements from tensile test
N	Number of stress measurements in random subset
n_c	Gear ratio between accumulator motor angular velocity and carriage linear velocity
N_{Ac}	Number of spans in the Unwind Accumulator
n_i	Gear ratio of the motor to roller i for driven rollers
$O_{PI,UW}$	PI output percentage of the Unwind Roll controller

$O_{PID,D1}$	PID output percentage of the Dancer 1 PID
r	Ratio statistic used to determine steady state
R_{c0}	Radius of spindle that Unwind Roll is would upon
R_c	Radius of roller in accumulator carriage i
R_i	Radius of Roller i
$RRMS_i$,$RRMS_{fi}$	i^{th} root mean square of random subset and its filtered value
RMS_i	i^{th} root mean square
$\overline{RRMS}$	Average root mean square of random subset
S_i	Scale factors used in the PI controllers. $i = t1, b$
t_i	Tension in span i
t_{3_i}	Tension of i^{th} span in the accumulator
t_{ci}	Tension in span i of Unwind Accumulator
t_w	Thickness of the web
T_{tix}	Torque due to x direction component of tension i about the dancer pivot
T_{tiy}	Torque due to y direction component of tension i about the dancer pivot
t_{meas}	Averaged measured tension used in the Unwind Roll control
t_r	Reference tension
u_i	Control input to roller i
v_i	Velocity of roller i
v_c	Velocity of the accumulator carriage
v_{cr}	Reference velocity of the accumulator carriage
v_{iref}, v_{ir}	Velocity reference of roller i
v_{ls}	Line speed reference
v_{1r}	Speed reference for Pull Roll 1
v_{1rr}	Ramped speed reference for Pull Roll 1

v_{3_i}	Velocity of i^{th} roller in the accumulator
x_c	Position of the accumulator carriage
x_t	Measured linear displacement of the dancer roller
$x_{t,max}$	Maximum linear displacement of Dancer 1
x_{tr}	Reference displacement of Dancer 1
α_i	Angle from horizontal that tension i is applied on the dancer roller
γ_i	Wrap angle of the web around the dancer from horizontal to the point where tension i is applied on the dancer roller
λ_i	Filter factors
$\nu_{fi}^2, \delta_{fi}^2$	i^{th} filtered numerator and denominator variance
ω_i	Angular velocity of Roller i
ω_c	Angular velocity of accumulator motor shaft
ρ_w	Density of the web
$\bar{\sigma}$	Model value of stress during tensile test
σ_i	Web stress of Span i
σ_{mi}	i^{th} Web stress measurement during tensile test
σ_n^2, σ_d^2	Numerator and denominator variances
τ_{mc}	Torque produced by the accumulator motor
$\tau_{cmd,i}$	Commanded torque of element i
τ_f	Friction torque
τ_p	Time constant for brake pneumatic device
θ_d	Angular displacement of the dancer roll from vertical
θ_n	Angular displacement of the dancer roll from dancer's zero position to vertical
ε_i	Strain in span i
ε_{3_i}	Strain of i^{th} span in the accumulator

Chapter 4

A	Cross sectional area of the web
b	Damping constant in Maxwell element
b_w	Lateral width of the web
d_x	Dancer 1 trim
C_{ij}	Controller for loop i (tension/velocity) and control strategy j (velocity/torque)
E	Spring constant in Maxwell element
E_v	Spring constant in Maxwell element
E_{vel}	Variational velocity error
J_i	Inertia of roller i
K_{ijk}	Integral PI gain of loop j (tension/velocity) and control strategy k (velocity/torque)
K_{pjk}	Proportional PI gain of loop j (tension/velocity) and control strategy k (velocity/torque)
L_1	Length of Span 1
R_i	Radius of roller i
t_r	Reference tension
v_i	Velocity of roller i
v_r	Velocity reference
δ_{rjk}	Real component of the characteristic equation of loop j (tension/velocity) and control strategy k (velocity/torque)
δ_{ijk}	Imaginary component of the characteristic equation of loop j (tension/velocity) and control strategy k (velocity/torque)
τ_i	i^{th} time constant
ε_i	Strain in span i
ε_r	Reference strain

Chapter 5

d_x	Dancer 1 trim
F	Force applied to keep Dancer 1 vertical
g	Acceleration due to gravity
J_i	Inertia of element i
J_c	Inertia of accumulator motor, gears, carriage, and rollers
$K_{d,D1}$	Derivative gain of Dancer 1 PID
$K_{i,AC}$	Integral gain of accumulator speed loop PI
$K_{i,D1}$	Integral gain of Dancer 1 PID
$K_{i,PR1}$	Integral gain of Pull Roll 1 speed loop PI
$K_{i,PR2}$	Integral gain of Pull Roll 2 speed loop PI
$K_{p,AC}$	Proportional gain of accumulator speed loop PI
$K_{p,D1}$	Proportional gain of Dancer 1 PID
$K_{p,PR1}$	Proportional gain of Pull Roll 1 speed loop PI
$K_{p,PR2}$	Proportional gain of Pull Roll 2 speed loop PI
L_i	Length of span i
m_{gc}	Mass of accumulator carriage and rollers
n_c	Gear ratio between accumulator motor angular velocity and carriage linear velocity
N_{Ac}	Number of spans in the Unwind Accumulator
n_i	Gear ratio of the motor to roller i for driven rollers
R_c	Radius of roller in accumulator carriage i
R_i	Radius of Roller i
t_i	Tension in span i
t_{3_i}	Tension of i^{th} span in the accumulator
t_r	Reference tension
u_i	Control input to roller i

v_i	Velocity of roller i
v_{3_i}	Velocity of i^{th} roller in the accumulator
v_c	Velocity of the accumulator carriage
v_{ls}	Line speed reference
v_{ref}, v_r	Velocity reference
x_c	Position of the accumulator carriage
x_t	Measured linear displacement of the dancer roller
τ_f	Friction torque

CHAPTER 1

Introduction

1.1 Background

Any material that is produced in continuous flexible form in a roll-to-roll fashion is known as web and the manufacturing of such materials is referred to as web handling. Many of the consumer products today, such as paper, diapers, textiles, and laminate flooring, are made in web form. In the manufacture of such products, control of the longitudinal dynamics is essential to ensure high quality goods. The most important facet of longitudinal control is maintaining web tension at appropriate values. If web tension is not well regulated, there is a high potential for damaging the product and the web handling machinery, resulting in extra costs for the manufacturing company and, consequently, higher prices for the consumer.

A web line is the series of processes and components that are used in the production of the web material. The typical processes include printing, coating, heating, and cooling of the web, and these operations are essential in the manufacture of the product. The standard components of a web line include an unwinder, accumulators, pull rollers, idle rollers, dancers, load-cell rollers, a winder, and other machinery used in the processing of the web material such as ovens, printers, coaters, and heating/cooling rollers. The unwind section of a web line consists of the elements that aid in dispensing web into the web line. These components include the unwinder, accumulator, pull rollers, idle rollers, dancers, and load-cell rollers and they are discussed below.

The unwinder is an apparatus that contains a roll of web material (referred to as

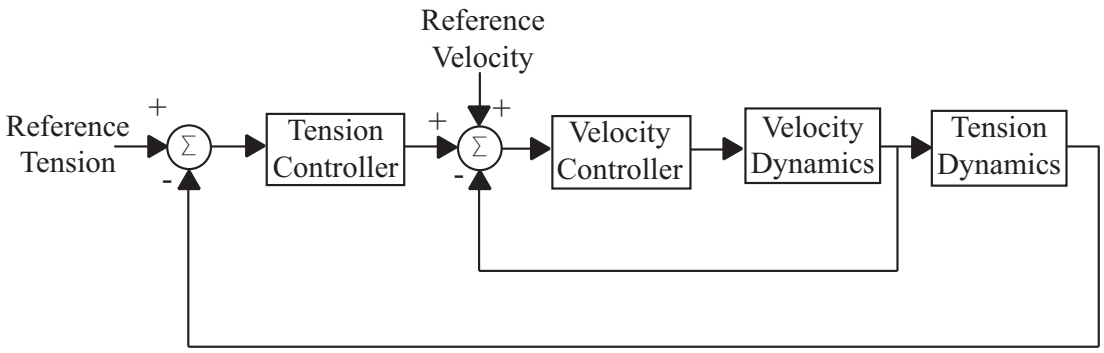

Figure 1.1: Control system with outer tension loop and inner velocity loop

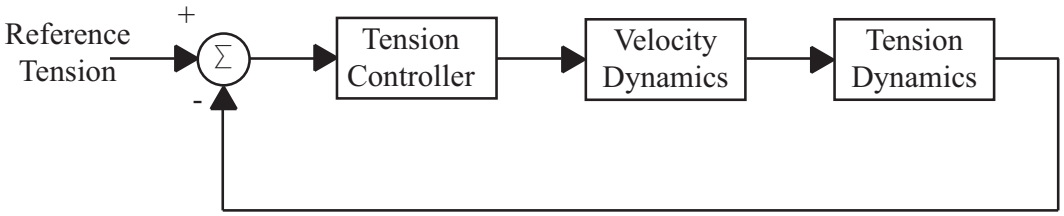

Figure 1.2: Control system with tension loop only

the unwind roll) and a corresponding control device. This is always the first element since it supplies the material for the entire web line. The control of this component can be achieved using either of the two methods presented below.

1. An outer loop that utilizes web tension feedback to provide a correction to the reference of an inner loop that controls the speed of the unwind roll (see Fig. 1.1)

2. A single tension loop that controls the torque applied to the unwind roll (see Fig. 1.2)

The first approach uses a motor attached to the material roll whereas the latter utilizes only a brake. During the operation of the web line, the unwind roll will eventually be depleted and will need to be replaced. Additionally, the material from the new roll must be affixed to the previous web material in a process called splicing. There are two types of splicing: (1) a static method called the zero-speed splicing where both the previous and new webs are stationary when they are connected and (2) an "on

the fly" method where both webs are moving as they are attached to one another. This process provides the continuity in the manufacture of web product.

However, during the changing of these rolls, the operation of the processing portion of the line must not be interrupted or else the web may be damaged. If the operation of the line is halted the web may overheat from being in an oven for too long or a coating may be too thick from being stopped at a printing station. To ensure the continuity of the web line, the accumulator is utilized. An accumulator is a structure that contains two sets of parallel idle rollers with one set fixed and the other on an extendable carriage. The carriage will move either vertically or horizontally depending on the size of the accumulator and the weight of the material. The web is alternately wound about a fixed and then a mobile roller so that the accumulator is able to either supply the rest of the line with web (in the case of an accumulator downstream of the unwinder) or receive web from the line (in the case of an accumulator upstream of the winder). In the former case, when the unwinder stops for a roll change, the accumulator carriage descends (contracts towards the fixed rollers) at a rate so that web is supplied at the correct speed. When the new roll is ready, the web upstream of the accumulator is driven faster than the web downstream which allows the carriage to move upwards (extend away from the fixed rollers), restoring the accumulator to its original height so that it is reset for the next roll change. The converse motions are seen for the case of the winder.

Pull rolls are driven rollers that propel the web through the line. They are most often controlled in a similar fashion to the type (1) unwinder, with an outer tension loop that provides a correction to the reference for the inner speed loop. This speed reference modification alters the speed of the pull roll in order to correct a tension error. However, there is one type of pull roll that does not use a tension loop and is strictly under velocity control. This roller is called the master speed roller and it dictates the process speed for the entire line. Not every roller is driven, however.

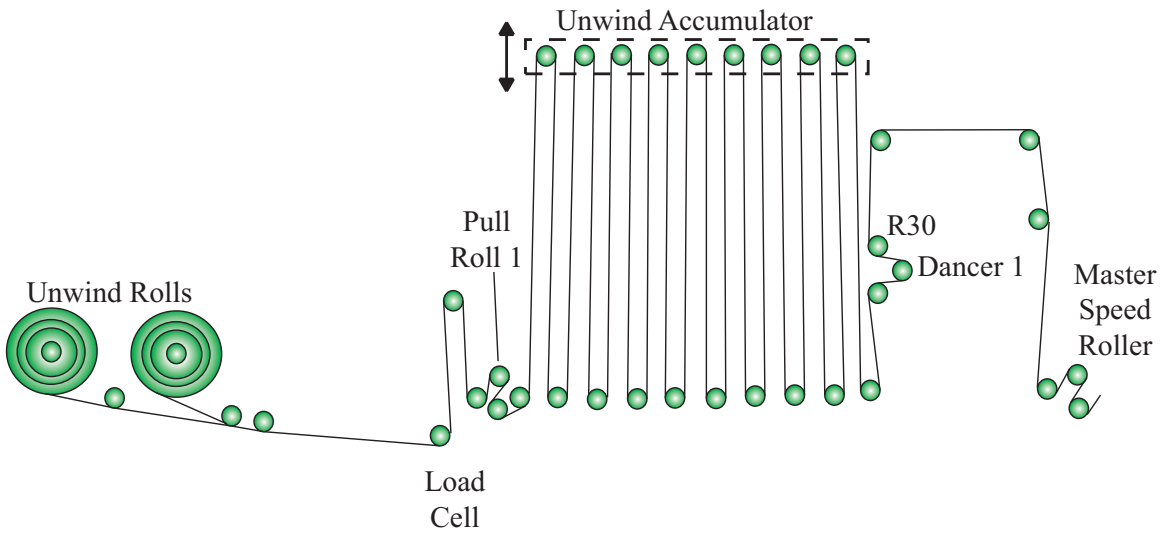

Figure 1.3: Unwind section of the CFL

Those that are not driven are referred to as idle rollers, and their purpose is to support the web as it travels through the web line.

There are two types of dancers, active and passive. Active dancers are rollers that displace (either linearly or rotationally) in order to vary the adjacent span lengths as a method to control tension. Passive dancers are components that use transducers to measure the displacement resulting from variations in tension, thus providing an indirect method for determining web tension. The motion can be either linear or rotational and for each type there is a normalizing force that is applied such that the passive dancer is at equilibrium in the nominal position when the tensions in the adjacent spans are at the reference value. Thus, if the tension changes, the balance of forces will be disrupted and the dancer will move. Load cells are elements that are also used for measuring web tension. They are attached to idle rollers and display the numerical value of the force the web is applying to the roller.

1.2 Coating and Fusion Line

The focus of this thesis is on the unwind section of a Coating and Fusion Line (CFL) of the Armstrong World Industries plant located in Stillwater, Oklahoma. The CFL is the final web line in the manufacture of several different brands of laminate flooring material. The main purpose of this line is to apply a coating that provides a protective layer for the printed laminate material.

The unwind section of the CFL is shown in Fig. 1.3 and includes two Unwind Rolls, Pull Roll 1, the 18-span Unwind Accumulator, Dancer 1, and the Master Speed Roller (also known as Pull Roll 2). The two Unwind Rolls are alternately used to supply web for the rest of the line. They are the type (2) unwinders from the above discussion and each are controlled by separate brakes that utilize the same algorithm. Since the Unwind Rolls are brake controlled, Pull Roll 1 is their sole means of rotation; the Unwind Rolls rotate as Pull Roll 1 draws the web. This driven roller is controlled in the typical fashion and uses position measurements from Dancer 1 as feedback for the outer tension loop. Similar to Pull Roll 1, the Unwind Accumulator has a controller with an outer loop that uses tension feedback from Dancer 1 to correct the reference for the inner speed loop for the carriage. Dancer 1 is of the passive pendulum type but provides translational displacement data. This is accomplished by a linear transducer that measures the movement of a point on the pivot lever. The final component of the unwind section is Pull Roll 2. This is the master speed roller for the entire CFL and as such is only under velocity control. Note that the control structure utilized in all of the controllers are the Proportional-Integral-Derivative (PID) type.

1.3 Thesis Outline

The main purpose of this thesis is to analyze and improve upon the current control strategies of the unwind section of the CFL. This web line was developed in an ad

hoc manner so the analysis contained herein gives a greater understanding of how the system operates. Additionally, the improvements suggested in this thesis will prove useful in increasing the functionality of the CFL and the overall quality of the flooring products.

Chapter 2 discusses the longitudinal web dynamics, the current control strategies employed on the CFL, and the parameter evaluations. References [1], [2], [4], and [3] are used in the development of the dynamic equations. Reference [1], which discussed a method for decentralized control of a web line, provided the equations for the velocity of an unwind roll and for the rate of change of the unwind roll radius. Additionally, the dynamics for driven and idle rollers were presented. The velocity of the rollers within the accumulator were given in Reference [2], which compared an industrial accumulator controller to one developed using Lyapunov's second method. The web used in the CFL is assumed to be viscoelastic, so Hooke's Law cannot be used to relate stress and strain for a span with fixed length, as was done in Reference [1]. To describe the viscoelastic behavior, Reference [4] is utilized. This article detailed the relationship between web tension and strain for a viscoelastic material. Reference [3] is used to derive the strain dynamics for spans of varying length (i.e., for spans within an accumulator and those immediately adjacent to a dancer). After the dynamics are derived, the control strategies for the Unwind Roll, Pull Rolls 1 and 2, and the Unwind Accumulator are discussed. The tension loop calculations are performed in the RSLogix5000 software, the operation of which is detailed in References [5] and [6]. The evaluation of the friction term and viscoelastic parameters are also included in this chapter. The friction is assumed to be a constant resistive torque and is determined via a test where an idler roller is accelerated to a predetermined velocity and then is allowed to slow to a stop using only friction. The time required for this deceleration is recorded and used in the friction torque calculation. The viscoelastic parameters are determined using the results of tensile

tests of the flooring material from Reference [12]. A heuristic optimization method developed in Reference [9] is used to fit a viscoelastic stress equation to the tensile test data. The model parameters that produce a stress curve that best matches the tensile test data are selected. This method is similar to that used in Reference [7] which developed a procedure for modeling biological tissues. Reference [10] is used to determine the stopping criteria for the optimizer.

In Chapter 3, the control strategy of the Unwind Roll is analyzed. First, a simplified system model containing the Unwind Roll and Pull Roll 1 is constructed and then verified by comparing simulation results with data collected from the CFL. Three new strategies are proposed in an effort to improve certain disadvantageous aspects of the current control strategy. The first strategy decreases the web tension sampling time and increases the resolution of the tension measurements and controller output. The second strategy utilizes time-varying PID gains and each of the modifications from the first strategy. The third strategy uses feed-forward control with corrections provided by a PID in addition to the modifications from the first strategy. These improvements are verified by simulations and subsequently employed on the CFL. The results of these experiments are compared against the performance of the current strategy, and based on this, a recommendation that will improve the tension performance is given.

Chapter 4 discusses the comparison between the type (1) and (2) unwinder control strategies. The control structure for each scenario is developed as well as their corresponding closed loop characteristic equation for the tension dynamics. The basis for this analysis is the stability regions of their respective controller parameter spaces. The procedure outlined in Reference [11] is used to map the stability boundary in the root space to each of the controller parameter spaces using their closed loop characteristic equations of the tension dynamics.

Chapter 5 describes the analysis and improvements of the control strategies for

Pull Roll 1 and the Unwind Accumulator. First a simplified model is developed that includes the major elements from Pull Roll 1 to Pull Roll 2. This is compared with data measured from the CFL for model verification. Subsequently, one improvement is suggested that will increase the tension regulation performance. A simulation is then used to demonstrate its effectiveness.

1.4 Contributions

The contributions of the work presented in this thesis are summarized below:

- The control strategies for the Unwind Roll, Pull Roll 1, and Unwind Accumulator were summarized into block diagram form. This will prove useful for the operators of the CFL to increase their understanding of the operation of these components.

- The disparity in the performance of the two brakes used to control the Unwind Roll was discovered during the work on this thesis. When using the same control algorithm, the controller output and tension performance for each brake can differ significantly.

- Three strategies for improving the control of the Unwind Roll are presented and supported by simulations. Additionally, the first two strategies were implemented onto the CFL and showed improvement over the current strategy. Based on the results of the experimentation, the strategy that most effectively increases the tension performance in this portion of the CFL is proposed as the recommended controller.

- While implementing the new control strategies for the Unwind Roll, the tension measurement resolution was increased by four times. This change was made permanent after the experimental employment of the first new strategy as it provides more accurate feedback for their controller.

- An algorithm to calculate the radius of the Unwind Roll was created in the controller software and is available for use. Each of the measurements required to compute this value were already accessible, however, through the implementation of the experiments, the radius calculation algorithm was generated.

- One improvement was suggested for Pull Roll 1 and the Unwind Accumulator to decrease the motion of Dancer 1. This modification requires altering the ramp rate of Pull Roll 1 and altering the deceleration profile of Pull Roll 1 during the initiation of the emptying procedure. Simulations show that this change results in decreased dancer motion and hence improved tension regulation.

CHAPTER 2

Models, Control Strategies, and Evaluation of Parameters for the Unwind Section of a Coating and Fusion Line

2.1 Introduction

This chapter details the development of a model for the portion of the Coating and Fusion Line (CFL) that includes all elements from the Unwind Roll to the Master Speed Roll. This includes the derivation of mathematical models that describe the dynamics of the web and of the web line components. Additionally, this model involves the evaluation of web parameters as well as the description of the control strategies employed on the CFL. In subsequent chapters, this model will be used to analyze the existing control strategies and will also be utilized in the development and evaluation of improvements to the control of specific elements of the CFL.

The simplification of the unwind section of the CFL is presented in Section 2.2. Subsequently, Section 2.3 discusses the derivation of the strain, tension, and velocity equations of the web and the dynamic equations of certain components of the line (such as the dancer and the accumulator). Following this discussion, a description of the procedures used to evaluate the viscoelastic parameters and the friction torque is presented in Section 2.4. The control strategy for maintaining the web tension and velocity is then given for each of the controlled components in Section 2.5. Section 2.6 concludes this chapter with a discussion of the applicability of the material presented herein to the subsequent chapters.

2.2 Simplification of the CFL

For simulation and analysis purposes, the portion of the CFL shown in Fig. 1.3 was simplified in Fig. 2.1, which shows the section of the CFL under consideration following several modifications. The first alteration is that only the major components of the line will be considered, meaning that the simplified model will only contain the Unwind Roll, Pull Roll 1, the Unwind Accumulator, Dancer 1, and the Master Speed Roll. Additionally, the load cell roll is shown with dashed lines to signify that it will provide tension feedback for Span 1 but not contribute directly to the dynamics of the system. As can be seen in Fig. 2.1, other rolls are also included (such as Accumulator Entry/Exit Rolls) in an attempt to match the actual configuration as accurately as possible. It should be noted that both the span lengths between components and the wrap angle of the web around the rollers will be maintained even though this is not depicted. The last simplifying assumption is that the tensions within the wound material roll and the span after the Master Speed Roll are set to the reference tension value for their corresponding portions of the CFL.

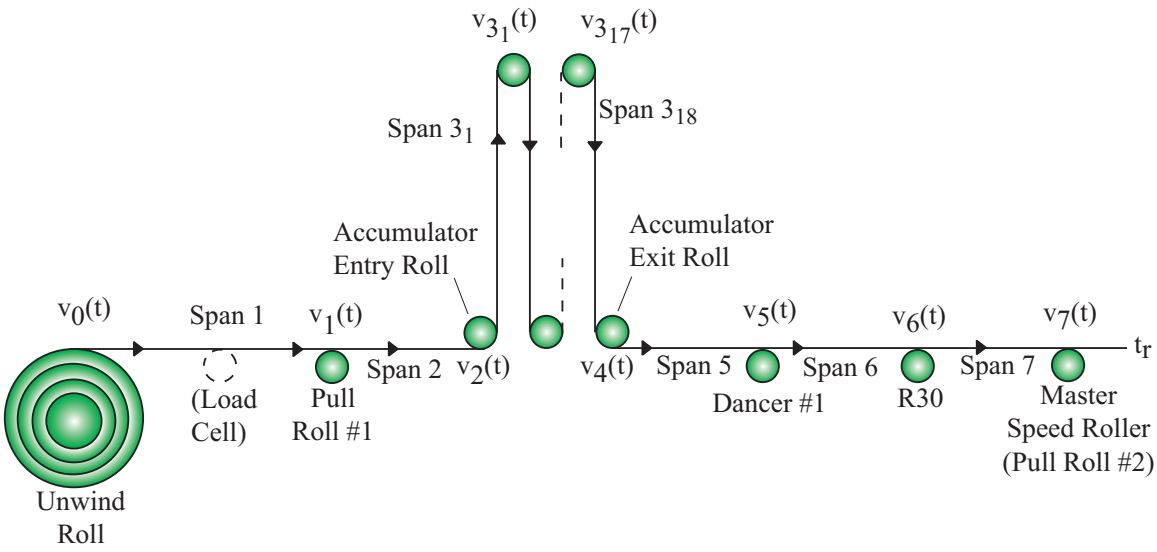

Figure 2.1: Simplified model of Unwind Roll to Pull Roll 2

2.3 Longitudinal Dynamics

This section describes the tension, velocity, and strain dynamic equations for the portion of the CFL shown in Fig. 2.1. Equation (2.1) given below describes the web velocity dynamics at the Unwind Roller with τ_{f0} as the friction term which can take several forms based on the friction model [1].

$$\dot{v}_0(t) = \frac{t_1(t)R_0^2(t)}{J_0(t)} - \frac{n_0 R_0(t)u_0(t)}{J_0(t)} - \frac{\tau_{f0}R_0(t)}{J_0(t)} - \frac{t_w v_0^2(t)}{2\pi J_0(t)}\left(\frac{J_0(t)}{R_0^2(t)} - 2\pi\rho_w b_w R_0^2(t)\right) \tag{2.1}$$

where v_0 is the peripheral velocity of the Unwind Roll, R_0 is the radius of the Unwind Roll, t_1 is the web tension in Span 1, J_0 is the inertia of the Unwind Roll, n_0 is the conversion between controller output and applied braking torque, u_0 is the control torque applied to the Unwind Roll, t_w is the web thickness, ρ_w is the web density, and b_w is the lateral web width. Notice in Equation (2.1) that the radius, R_0, and the inertia, J_0, are shown to vary with time. The reason is because the material roll radius (and hence the inertia) becomes smaller as material is released into the web line. This occurs at a rate given by the following equation [1].

$$\dot{R}_0(t) \approx -\frac{t_w v_0(t)}{2\pi R_0(t)} \tag{2.2}$$

The following equation describes the velocity dynamics for Rollers $i = 1$, 2, 4, 6, and 7 [1]. Note that rollers 2, 4, and 6 are idle rollers thus for $i = 2$, 4, and 6, $u_i(t) = 0$.

$$\frac{J_i}{R_i}\dot{v}_i(t) = (t_{i+1}(t) - t_i(t))R_i + n_i u_i(t) - \tau_f \tag{2.3}$$

where J_i is the inertia of Roller i, R_i is the radius of Roller i, v_i is the peripheral velocity of Roller i, t_i (t_{i+1}) is the web tension in Span i ($i+1$), n_i is the gear ratio

between the motor shaft and roller shaft of Roller i, u_i is the control input for Roller i, and τ_f is the constant friction torque applied to the roller.

Equation (2.4) describes the velocity of the web at the roller within the accumulator for $i = 1, ..., 17$ [2]. In actuality, the dynamics depend on the accumulator carriage velocity. However it is assumed that it does not significantly affect the value of $v_{3_i}(t)$ (the peripheral speed of Roller i within the accumulator) since the carriage velocity is much slower than that of $v_{3_i}(t)$. Note that $t_{3_{18}}(t) \equiv t_4(t)$.

$$\frac{J_{3_i}}{R_{3_i}}\dot{v}_{3_i}(t) = (t_{3_{i+1}}(t) - t_{3_i}(t))R_{3_i} - \tau_f \tag{2.4}$$

where J_{3_i} is the inertia of Roller i within the accumulator, R_{3_i} is the radius of Roller i within the accumulator, and t_{3_i} ($t_{3_{i+1}}$) is the web tension in Span i ($i + 1$) within the accumulator.

The velocity $v_5(t)$ (the peripheral speed of Dancer 1 roller) is dependent on the motion of the dancer roller. However, as in the case of the accumulator, the dancer roller motion does not significantly affect the velocity of the web, so it is ignored. The equation describing the dynamics of the web velocity at this location is given below [1].

$$\frac{J_5}{R_5}\dot{v}_5(t) = (t_6(t) - t_5(t))R_5 - \tau_f \tag{2.5}$$

where J_5 is the inertia of Dancer 1 roller, R_5 is the radius of Dancer 1 roller, and t_5 and t_6 are the web tensions in the spans upstream and downstream of Dancer 1, respectively.

The tension dynamics were derived by assuming that the web material exhibits viscoelastic behavior. The viscoelastic characteristics are captured using the model shown in Fig. 2.2 which shows a Maxwell model in parallel with a linear spring where E_v is the spring constant for the Maxwell component, b is the damping constant for the Maxwell component, and E is also a spring constant [4]. The stress and strain in

the model are related through Equation (2.6) [4].

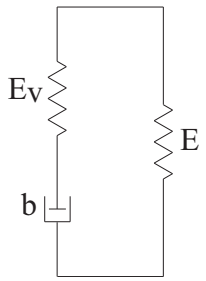

Figure 2.2: Maxwell element in parallel with a linear spring

$$\frac{1}{b}\sigma_i(t) + \frac{1}{E_v}\dot{\sigma}_i(t) = \frac{E}{b}\varepsilon_i(t) + \left(1 + \frac{E}{E_v}\right)\dot{\varepsilon}_i(t) \tag{2.6}$$

where σ_i is the web stress in Span i and ε_i is the web strain in Span i. Since $\sigma_i = t_i/A$ (A is the web cross-sectional area), the tension in Span i, for $i = 1, ..., 7$, is related to the strain by Equation (2.7).

$$\dot{t}_i(t) = -\frac{E_v}{b}t_i(t) + \frac{EE_vA}{b}\varepsilon_i(t) + (E_v + E)A\dot{\varepsilon}_i(t) \tag{2.7}$$

By using the law of conservation of mass around a control volume containing the span between two fixed adjacent rollers along with the assumptions that the strain is small and uniform along the span, the following relationship between the peripheral velocity of upstream and downstream rollers and the strain can be derived [4].

$$\dot{\varepsilon}_i(t) = \frac{v_i(t)}{L_i}(1 - \varepsilon_i(t)) - \frac{v_{i-1}(t)}{L_i}(1 - \varepsilon_{i-1}(t)) \tag{2.8}$$

where L_i is the length of Span i. Equation (2.8) describes the strain dynamics for $i = 1$, 2, and 7.

The strain dynamics for the spans in the accumulator can be derived from Reference [3]. Assuming that the density and viscoelastic parameters are constant over the web's cross section and assuming that the strain is small and constant along the

span, the conservation of mass relationship for the control volume shown in Fig. 2.3 can be written as shown in Equation (2.9) [3].

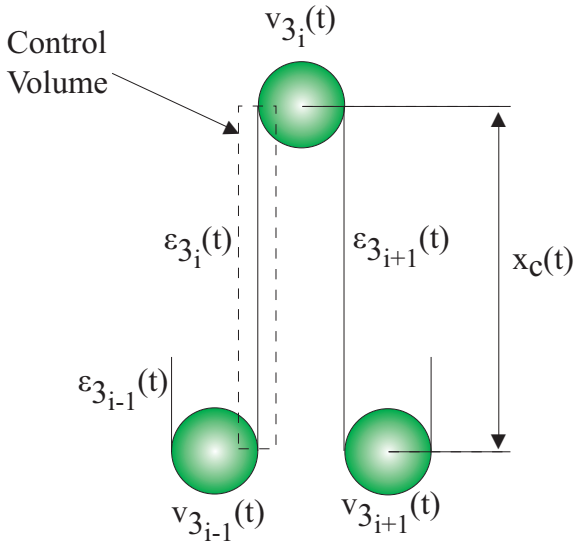

Figure 2.3: Two span accumulator with control volume

$$\left[\int_0^{x_c(t)} dx\right]\frac{d}{dt}\left(1-\varepsilon_{3_i}(t)\right)+\left(1-\varepsilon_{3_i}(t)\right)\frac{d}{dt}\left[\int_0^{x_c(t)} dx\right] \tag{2.9}$$
$$= v_{3_{i-1}}(t)\left[1-\varepsilon_{3_{i-1}}(t)\right]-v_{3_i}(t)\left[1-\varepsilon_{3_i}(t)\right]$$

where x_c is the accumulator carriage height and ε_{3_i} ($\varepsilon_{3_{i-1}}$) is the strain of Span i ($i-1$) within the accumulator. Using Leibnitz rule to perform the differentiation of the second term on the left hand side of Equation (2.9), the strain dynamics for spans within the accumulator can be derived [3].

$$\dot{\varepsilon}_{3_i}(t)=\frac{\left(1-\varepsilon_{3_i}(t)\right)\dot{x}_c(t)}{x_c(t)}+\frac{v_{3_i}(t)\ \left(1-\varepsilon_{3_i}(t)\right)}{x_c(t)}-\frac{\left(1-\varepsilon_{3_{i-1}}(t)\right)\ v_{3_{i-1}}(t)}{x_c(t)} \tag{2.10}$$

The linear velocity of the accumulator carriage, v_c, is related to the angular velocity of the motor that raises and lowers the carriage, ω_c, by Equation (2.11).

$$v_c(t)=n_c\omega_c(t) \tag{2.11}$$

where n_c has units of length. The motor dynamics is given by Equation (2.12) and the carriage dynamics is presented in Equations (2.13) and (2.14).

$$J_{cm}\dot{\omega}_c(t) = \tau_{mc}(t) - n_c F_c(t) \tag{2.12}$$

$$m_c\ddot{x}_c(t) = F_c(t) - \sum_{i=1}^{N_{Ac}} t_{3_i}(t) - F_{gc} \tag{2.13}$$

$$\dot{x}_c(t) = v_c(t) \tag{2.14}$$

where J_{cm} is the inertia of the accumulator carriage motor, τ_{mc} is the control torque applied to the accumulator motor shaft, $F_c(t)$ is the interaction force between the motor and the carriage, m_c is the mass of the accumulator carriage, N_{Ac} is the number of accumulator spans, and F_{gc} is the gravitational force of the accumulator carriage. Combining Equations (2.11) through (2.14) results in Equation (2.15) which shows the accumulator carriage dynamics reflected to the motor side. Note that $J_c = J_{cm}+n_c^2 m_c$.

$$J_c\dot{\omega}_c(t) = \tau_{mc}(t) - n_c \sum_{i=1}^{N_{Ac}} t_{3_i}(t) - n_c F_{gc} \tag{2.15}$$

To derive the equations for the strain dynamics for the spans immediately upstream and downstream of the dancer (Spans 5 and 6), the dancer is approximated as a two span accumulator. The strain equation for a span within an accumulator derived in Reference [3] will be used with the accumulator carriage position and velocity terms replaced with $L_i(t)$ and $\dot{L}_i(t)$, respectively, where $i = 5, 6$ for Spans 5 and 6, respectively. Thus the strain in Span 5 is given by Equation (2.16) [3] and that of Span 6 is presented in Equation (2.17) [3].

$$\dot{\varepsilon}_5(t) = \frac{(1-\varepsilon_5(t))\,\dot{L}_5(t)}{L_5(t)} + \frac{v_5(t)\;(1-\varepsilon_5(t))}{L_5(t)} - \frac{(1-\varepsilon_4(t))\,v_4(t)}{L_5(t)} \tag{2.16}$$

$$\dot{\varepsilon}_6(t) = \frac{(1-\varepsilon_6(t))\,\dot{L}_6(t)}{L_6(t)} + \frac{v_6(t)\;(1-\varepsilon_6(t))}{L_6(t)} - \frac{(1-\varepsilon_5(t))\,v_5(t)}{L_6(t)} \tag{2.17}$$

The lengths $L_5(t)$ and $L_6(t)$ can be represented as nominal lengths plus varying lengths. The nominal length of Span 5, L_{5n}, is distance AB from Fig. 2.4 and that of Span 6, L_{6n}, is CD. Although the dancer motion is purely rotational, it is assumed that the angular displacement of the dancer from vertical, $\theta_d(t)$, is small. Therefore, its displacement can be approximated as being the arc length from E to E' (see Fig. 2.4). This distance in terms of $\theta_d(t)$ is shown in Equation (2.18) below.

$$EE' = l\theta_d(t) \tag{2.18}$$

where l is the distance OE in Fig. 2.4. Thus, the total length of Spans 5 and 6 can be approximated as shown in Equations (2.19) and (2.20).

$$L_5(t) = L_{5n} + l\theta_d(t) \tag{2.19}$$

$$L_6(t) = L_{6n} + l\theta_d(t) \tag{2.20}$$

The first time derivative of Equations (2.19) and (2.20) are given below.

$$\dot{L}_5(t) = l\dot{\theta}_d(t) \tag{2.21}$$

$$\dot{L}_6(t) = l\dot{\theta}_d(t) \tag{2.22}$$

However, Dancer 1 does not have its zero position at vertical nor does it measure angular displacement; its zero position is a constant θ_n clockwise from vertical (see Fig. 2.5). The dancer displacement is measured with a linear transducer which is placed a distance l_x (distance OA in Fig. 2.5) down the lever arm from the pivot. This measured displacement, $x_t(t)$, is related to EE' and $\theta_d(t)$ by the following equation.

$$\theta_d(t) = \frac{EE'}{l} = \frac{x_t(t) - l_x \sin(\theta_n)}{l_x} \tag{2.23}$$

Thus $\theta_d(t)$ is related to $x_t(t)$ by the following.

$$\theta_d(t) = \frac{x_t(t) - l_x \sin(\theta_n)}{l_x} \tag{2.24}$$

The time derivative of Equation (2.24) is given below.

$$\dot{\theta}_d(t) = \frac{\dot{x}_t(t)}{l_x} \tag{2.25}$$

Thus, combing Equations (2.19) through (2.22) with (2.24) and (2.25), the total lengths of Spans 5 and 6 and their first time derivatives in terms of the measured displacement, $x_t(t)$, can be calculated as shown in Equations (2.26) through (2.29).

$$L_5(t) = L_{5n} + \frac{l}{l_x}(x_t(t) - l_x \sin(\theta_n)) \tag{2.26}$$

$$L_6(t) = L_{6n} + \frac{l}{l_x}(x_t(t) - l_x \sin(\theta_n)) \tag{2.27}$$

$$\dot{L}_5(t) = \frac{l}{l_x}\dot{x}_t(t) \tag{2.28}$$

$$\dot{L}_6(t) = \frac{l}{l_x}\dot{x}_t(t) \tag{2.29}$$

Substituting Equations (2.26) and (2.28) into Equation (2.16) and Equations (2.27) and (2.29) into Equation (2.17) gives the strain dynamics in Spans 5 and 6 in terms of the measured dancer displacement and are given in Equations (2.30) and (2.31), respectively.

$$\begin{aligned}\dot{\varepsilon}_5(t) = &\frac{(1-\varepsilon_5(t))\, l\dot{x}_t(t)}{L_{5n}\, l_x + l x_t(t) - l l_x \,\sin(\theta_n)} + \frac{(1-\varepsilon_5(t))\, l_x v_5(t)}{L_{5n} l_x + l x_t(t) - l l_x \,\sin(\theta_n)} \\ &- \frac{(1-\varepsilon_4(t))\, l_x v_4(t)}{L_{5n}\, l_x + l x_t(t) - l l_x \,\sin(\theta_n)}\end{aligned} \tag{2.30}$$

$$\dot{\varepsilon}_6(t) = \frac{(1-\varepsilon_6(t))\, l\dot{x}_t(t)}{L_{6n}\, l_x + lx_t(t) - ll_x\, \sin(\theta_n)} + \frac{(1-\varepsilon_6(t))\, l_x v_6(t)}{L_{6n} l_x + lx_t(t) - ll_x\, \sin(\theta_n)} - \frac{(1-\varepsilon_5(t))\, l_x v_5(t)}{L_{6n}\, l_x + lx_t(t) - ll_x\, \sin(\theta_n)} \tag{2.31}$$

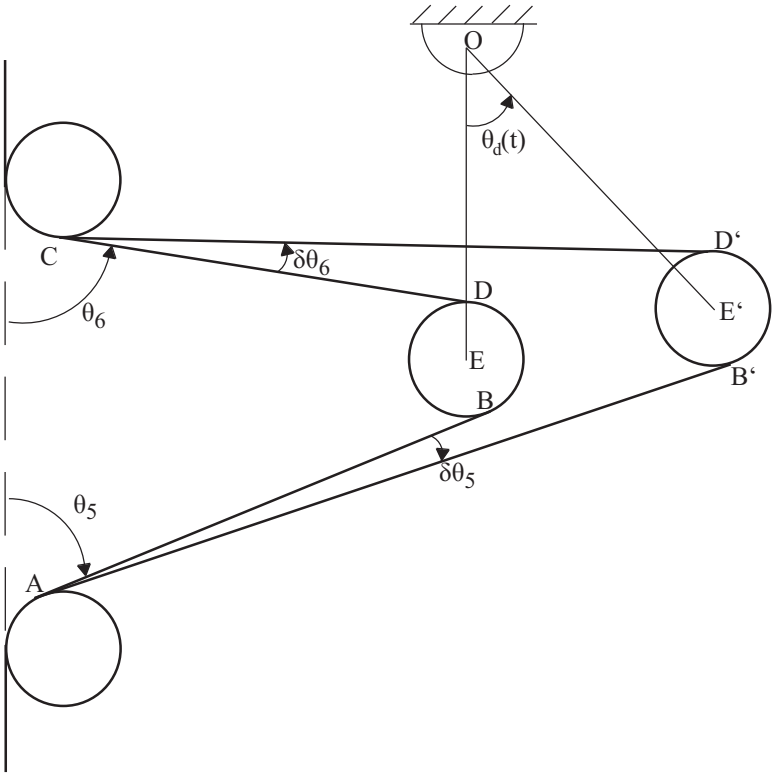

Figure 2.4: Displaced dancer

The dancer velocity dynamics are determined from the dancer free body diagram which is shown in Fig. 2.6. The constant applied force F is applied to keep the dancer vertical when the tension in Spans 5 and 6 are equal to the reference tension. This force is applied with a piston air cylinder device which is on a pivot so that F is not always completely horizontal. However, assuming small variations in tension such that the dancer movement is not significant, the direction of F can be approximated as being horizontal.

Note that the web wrap angle of the dancer is not 180 degrees. This means that $t_5(t)$ and $t_6(t)$ are not applied horizontally. Thus there is a vertical component associated with each tension. It is also assumed that due to the small dancer movement,

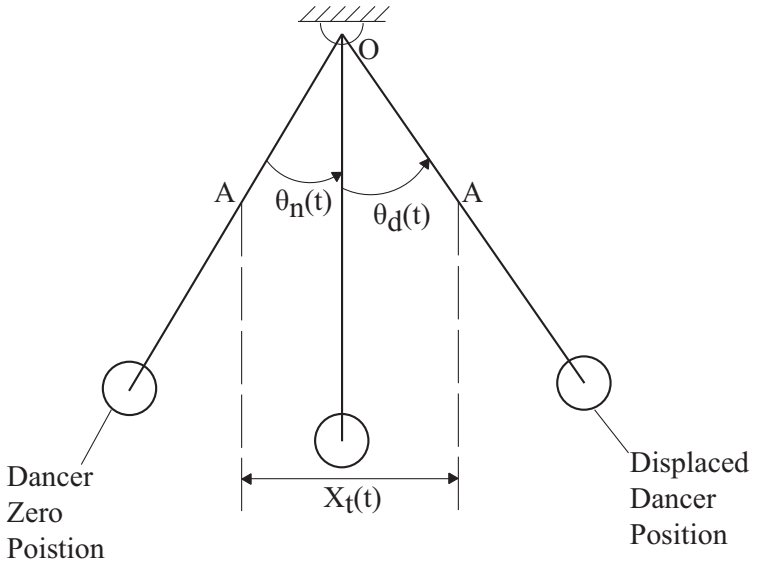

Figure 2.5: Zero, vertical, and displaced positions of Dancer 1

the angles with respect to horizontal at which $t_5(t)$ and $t_6(t)$ are applied at Dancer 1 remain constant. Using Fig. 2.6, the torques due to the horizontal and vertical components of $t_5(t)$ and $t_6(t)$ about the pivot point of Dancer 1 (point O from Fig. 2.6) are calculated to be as follows.

$$T_{t5x} = -(l\cos(\theta_d(t)) + R_d\sin(\gamma_5))t_5(t)\cos(\alpha_5) \tag{2.32}$$

$$T_{t5y} = -(l\sin(\theta_d(t)) + R_d\cos(\gamma_5))t_5(t)\sin(\alpha_5) \tag{2.33}$$

$$T_{t6x} = -(l\cos(\theta_d(t)) - R_d\sin(\gamma_6))t_6(t)\cos(\alpha_6) \tag{2.34}$$

$$T_{t6y} = (l\sin(\theta_d(t)) + R_d\cos(\gamma_6))t_6(t)\sin(\alpha_6) \tag{2.35}$$

where T_{t5x} is the torque at the dancer pivot (point O form Fig. 2.6) due to the horizontal component of $t_5(t)$, T_{t5y} is the torque at the dancer pivot due to the vertical component of $t_5(t)$, T_{t6x} is the torque at the dancer pivot due to the horizontal

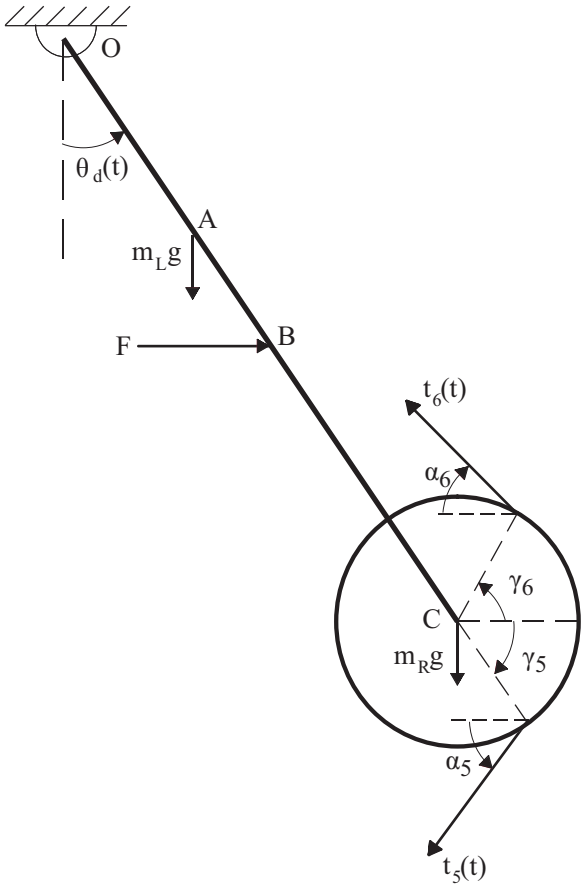

Figure 2.6: Free body diagram of Dancer 1

component of $t_6(t)$, T_{t6y} is the torque at the dancer pivot due to the vertical component of $t_6(t)$, α_i is the angle from horizontal that the tension in Span i is applied on the dancer roller, γ_i is the wrap angle of the web around the dancer from horizontal to the point where the tension in Span i is applied on the dancer roller, R_d is the radius of the Dancer 1 roller, and l is distance OC in Fig. 2.6. Using the above relations and Fig. 2.6, the equation of motion of Dancer 1 about O can be derived. The equation of motion in terms of $\theta_d(t)$ is as follows.

$$
\begin{aligned}
J_{dt}\ddot{\theta}_d(t) = {} & Fl_F\cos(\theta_d(t)) - l_L m_L g\sin(\theta_d(t)) - lm_R g\sin(\theta_d(t)) \\
& + (l\sin(\theta_d(t)) + R_d\cos(\gamma_6))t_6(t)\sin(\alpha_6) - (l\cos(\theta_d(t)) \\
& - R_d\sin(\gamma_6))t_6(t)\cos(\alpha_6) - (l\sin(\theta_d(t)) + R_d\cos(\gamma_5))t_5(t)\sin(\alpha_5) \\
& - (l\cos(\theta_d(t)) + R_d\sin(\gamma_5))t_5(t)\cos(\alpha_5) \qquad (2.36)
\end{aligned}
$$

where J_{dt} is the inertia of Dancer 1, m_L is the combined mass of both dancer pivot arms, m_R is the mass of the Dancer 1 roller, and l_L and l_F are distances OA and OB, respectively. Equation (2.25) gives the first time derivative of $\theta_d(t)$ in terms of $\dot{x}_t(t)$. Differentiating this equation again will result in Equation (2.37), the second derivative of $\theta_d(t)$ in terms of $\ddot{x}_t(t)$.

$$
\ddot{\theta}_d(t) = \frac{\ddot{x}_t(t)}{l_x} \qquad (2.37)
$$

Substituting Equations (2.24) and (2.37) into Equation (2.36) and assuming $\theta_d(t)$ is small so that $\cos(\theta_d(t)) \approx 1$ and $\sin(\theta_d(t)) \approx \theta_d(t)$ yields the equation of motion of Dancer 1 in terms of its measured linear displacement. This is given below.

$$
\begin{aligned}
\frac{J_{dt}}{l_x}\ddot{x}_t(t) = {} & Fl_F + \left(\frac{-l_L m_L g - lm_R g + l\sin(\alpha_6)t_6(t) - lt_5(t)\sin(\alpha_5)}{l_x}\right)x_t(t) \\
& + (-l\sin(\theta_n)\sin(\alpha_6) + R_d\cos(\gamma_6)\sin(\alpha_6) - l\cos(\alpha_6) + R_d\sin(\gamma_6)\cos(\alpha_6))t_6(t) \\
& + (l\sin(\theta_n)\sin(\alpha_5) - R_d\cos(\gamma_5)\sin(\alpha_5) - l\cos(\alpha_5) - R_d\sin(\gamma_5)\cos(\alpha_5))t_5(t) \\
& + l_L m_L g\sin(\theta_n) + lm_R g\sin(\theta_n) \qquad (2.38)
\end{aligned}
$$

2.3.1 Linearized Dynamics

This section describes the linearization of Equations (2.1), (2.7), and (2.8) for the simplified model shown in Fig. 2.7.

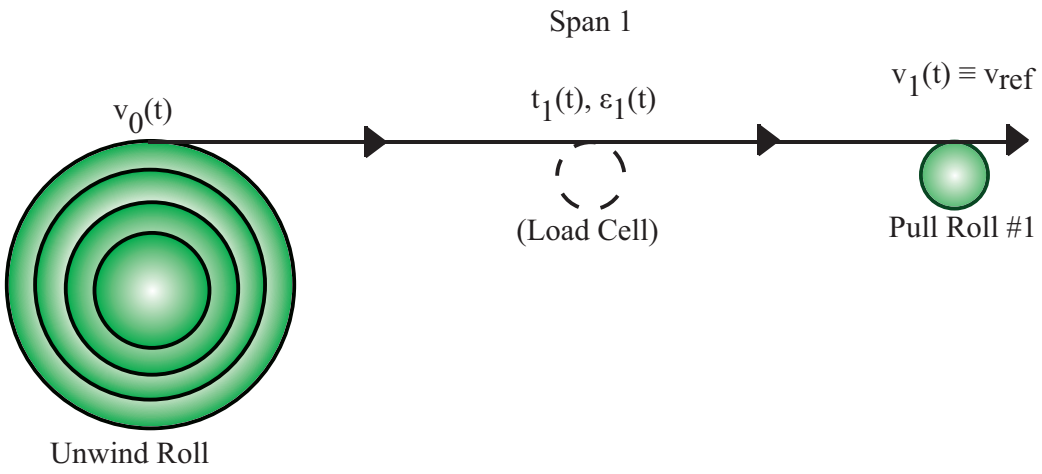

Figure 2.7: Section of web line for linearized dynamics

The first step is to assume that the Unwind Roll radius $R_0(t)$ is slowly changing so that $R_0(t) \approx$ constant. Additionally, it is assumed that the reference velocity for Pull Roll 1, v_r, is constant and the wound in strain, ε_0, is equal to the reference value and is also constant. Thus Equations (2.1) and (2.8) reduce to Equations (2.39) and (2.40).

$$\dot{v}_0(t) = \frac{t_1(t)R_0^2}{J_0} - \frac{n_0 R_0 u_0(t)}{J_0} - \frac{\tau_{f0} R_0}{J_0} \tag{2.39}$$

$$\dot{\varepsilon}_1(t) = \frac{v_r}{L_1}(1 - \varepsilon_1(t)) - \frac{v_0(t)}{L_1}(1 - \varepsilon_r) \tag{2.40}$$

The second step is to define the variational dynamics by using the following relationships: $v_0(t) = V_0(t) + v_r$, $t_1(t) = T_1(t) + t_r$, and $\varepsilon_1(t) = \epsilon_1(t) + \varepsilon_r$, where $V_0(t)$, $T_1(t)$, and $\epsilon_1(t)$ are, respectively, the velocity, tension, and strain deviations from their corresponding reference values. Additionally, $u_0(t) = U_0(t) + u_{0r}$, where u_{0r} is the control input required to maintain equilibrium and $U_0(t)$ is the deviation of the control input from the equilibrium value. With these substitutions, Equations (2.7), (2.39), and (2.40) become Equations (2.41) through (2.43).

$$\dot{V}_0(t) = \frac{R_0^2}{J_0}(T_1(t) + t_r) + \frac{n_0 R_0}{J_0}(U_0(t) + u_{0r}) - \frac{R_0}{J_0}\tau_f \tag{2.41}$$

$$\dot{T}_1(t) = -\frac{E_v}{b}(T_1(t) + t_r) + \frac{EE_vA}{b}(\epsilon_1(t) + \varepsilon_r) + (E_v + E)A\dot{\epsilon}_1(t) \tag{2.42}$$

$$\dot{\epsilon}_1(t) = \frac{v_r}{L_1}(1 - \epsilon_1(t) - \varepsilon_r) - \frac{V_0(t) + v_{0r}}{L_1}(1 - \varepsilon_r) \tag{2.43}$$

At equilibrium, $V_0(t)$, $\dot{V}_0(t)$, $T_1(t)$, $\dot{T}_1(t)$, $\epsilon_1(t)$, $\dot{\epsilon}_1(t)$, and $U_0(t)$ are all zero. Thus, the equilibrium conditions are as follows.

$$u_{0r} = \frac{-R_0 t_r + \tau_f}{n_0} \tag{2.44}$$

$$\varepsilon_r = \frac{t_r}{EA} \tag{2.45}$$

$$v_{r0} = v_r \tag{2.46}$$

Inserting the equilibrium conditions into Equations (2.41) through (2.43) yields the linearized variational dynamics given below.

$$\dot{V}_0(t) = \frac{R_0^2}{J_0}T_1(t) + \frac{n_0 R_0}{J_0}U_0(t) \tag{2.47}$$

$$\dot{T}_1(t) = -\frac{E_v}{b}T_1(t) + \frac{EE_vA}{b}\epsilon_1(t) + (E_v + E)A\dot{\epsilon}_1(t) \tag{2.48}$$

$$\dot{\epsilon}_1(t) = -\frac{v_r}{L_1}\epsilon_1(t) - \frac{(1 - \varepsilon_r)}{L_1}V_0(t) \tag{2.49}$$

2.4 Parameter Evaluation

This section describes the evaluation of the viscoelastic parameters and the friction torque found in the dynamic equations.

2.4.1 Viscoelastic Parameter Evaluation

The terms E, E_v, and b are obtained by using nonlinear regression analysis to match a stress model derived from Equation (2.6) to data from tensile test results of two web materials. The tensile tests were conducted in Reference [12]. This procedure is similar to one conducted in Reference [7]. The two materials tested were the Felt, Hot Melt Calendar, Gel (FHG) composite and the Royelle Felt and Gel (RFG) composite. These materials were chosen because they are indicative of the materials that are used in the unwind section of the CFL. The tensile tests were conducted per ASTM D638.

Stress Model Derivation

Before the regression analysis can be discussed, the model of the web stress during the tensile tests, $\bar{\sigma}(t)$, must be derived. A tensile test consists of loading a strip of material in tension such that the strain rate is constant until the specimen ruptures [8]. After each test, the strain data was plotted versus time. These plots showed that all of the strain data had the form of a straight line with zero intercept and a slope of 0.0024 $\frac{in/in}{s}$. Hence, Equation (2.6) becomes a first order differential equation as given below.

$$\frac{1}{b}\bar{\sigma}(t) + \frac{1}{E_v}\dot{\bar{\sigma}}(t) = \frac{0.0024E}{b}t + 0.0024\left(1 + \frac{E}{E_v}\right) \tag{2.50}$$

The solution to Equation (2.50) gives the web stress as a function of time during the tensile tests and is given below.

$$\bar{\sigma}(t) = 0.0024Et + 0.0024b - 0.0024be^{-\frac{E_v}{b}t} \tag{2.51}$$

Regression Analysis

Now that the stress model has been chosen, the regression analysis procedure can be discussed. The objective of the regression analysis is to find the viscoelastic parame-

ters such that

$$\min_{\{E,E_v,b\}} J = \sqrt{\sum_{i=1}^{n} \frac{(\bar{\sigma}_i - \sigma_{mi})^2}{n}} \tag{2.52}$$

where σ_{mi} is the i^{th} stress measurement from the tensile test, $\bar{\sigma}_i$ is the corresponding model stress value, and n is the total number of measurements. J represents the root-mean-square (RMS) value between the measured data and the model values. $\bar{\sigma}_i$ is calculated using Equation (2.51) and the time stamp corresponding to σ_{mi}.

The method chosen to solve the optimization statement given in Equation (2.52) is the Cyclic Heuristic Search [9]. The procedure for this method is as follows. Initial values for E, E_v, and b are randomly selected and are used to calculate the n $\bar{\sigma}_i$ values. These are used in Equation (2.52) to determine the base objective function value, J_0. E is then incremented by dE, the n $\bar{\sigma}_i$ values are calculated using Equation (2.51), and the trial objective function value, J_t, is determined using Equation (2.52). If $J_t < J_0$, then J_t becomes the new base objective function value and dE is increased. Otherwise, J_0 remains the base objective function value and dE decreases in magnitude and changes sign. This procedure is repeated with E_v and b, which completes one optimization cycle. The above procedure is repeated until the stopping criterion is satisfied, thus yielding the E, E_v, and b set that best matches the model described by Equation (2.51) to the tensile test data.

The selected stopping criterion for the optimization procedure defined in Reference [10], will now be described. The RMS between the measured data and the model will generally asymptotically decrease with each optimizer iteration to the minimum. Likewise, the RMS of a random sampling (RRMS) of a random subset of the data will also show this trend and will have random perturbations. Viewing the RRMS over progressive iterations gives the optimization process the appearance of a noisy system transitioning from transient to a steady state value. If the steady state condition is detected, then the minimum defined by Equation (2.52) has been found and

optimization iterations should cease. The method for determining steady state is summarized below. Let r, the ratio statistic that determines steady state, be defined as follows.

$$r = \frac{\sigma_n^2}{\sigma_d^2} \tag{2.53}$$

where σ_n^2 is a moving average and σ_d^2 is a measure of variance along the data trend [9]. At steady state, σ_d^2 is an unbiased estimate, assuming both the data and noise are independently distributed. The expressions for these two variances are given below.

$$\sigma_n^2 = \frac{1}{N-1}\sum_{i=1}^{N}(RRMS_i - \overline{RRMS})^2 \tag{2.54}$$

$$\sigma_d^2 = \frac{1}{2(N-1)}\left(\sum_{i=1}^{N}(RRMS_i - RRMS_{i-1})^2\right) \tag{2.55}$$

where $RRMS_i$ is the RRMS of the i^{th} optimization iteration and $\overline{RRMS}$ is the average RRMS over the past N optimization iterations. Note that these variances are calculated at each optimizer iteration.

The calculations associated with Equations (2.54) and (2.55) present a computational burden. Thus, a technique which requires less computational effort was used. This technique uses exponentially-weighted moving averages (first-order filtered values) in place of the variances defined by Equations (2.54) and (2.55). The expressions for these exponentially-weighted moving averages, $\nu_{f_i}^2$ and $\delta_{f_i}^2$, are given below.

$$\nu_{f_i}^2 = \lambda_2\left(RRMS_i - RRMS_{f_{i-1}}\right)^2 + (1-\lambda_2)\nu_{f_{i-1}}^2 \tag{2.56}$$

$$RRMS_{f_i} = \lambda_1 RRMS_i + (1-\lambda_1)RRMS_{f_{i-1}} \tag{2.57}$$

$$\delta_{f_i}^2 = \lambda_3\left(RRMS_i - RRMS_{i-1}\right)^2 + (1-\lambda_3)\delta_{f_{i-1}}^2 \tag{2.58}$$

where λ_1, λ_2, and λ_3 are filter factors and are comparable to the inverse of N. Equations (2.56) and (2.58) replace Equations (2.54) and (2.55), respectively. Additionally, the filtered value, $RRMS_{f_i}$, is used instead of the $\overline{RRMS}$. The equivalent of Equation (2.53) can now be written as the following.

$$r_i = (2 - \lambda_1) \frac{\nu_{f_i}^2}{\delta_{f_i}^2} \tag{2.59}$$

At steady state, the expected value of r is unity, otherwise it is much larger. However, due to the noise presented by the RRMS calculation, it is possible for the optimizer to not be at steady state and yet have an r value near unity. To minimize the probability of accepting this steady state condition when it is not true, Reference [9] recommends using $\lambda_1 = \lambda_2 = \lambda_3 = 0.05$ with a critical r-value of 0.8. Thus, at some optimizer iteration when the r-value is below 0.8, it is assumed that steady state has been reached and thus the minimum has been found.

The entire regression procedure can now be described. After the completion of each optimizer iteration, the RRMS is calculated and used in Equations (2.57) through (2.58). The ratio statistic for that iteration is calculated using Equation (2.59). If this value is less than 0.8, the optimizer has found the best possible E, E_v, and b set and thus stops iterating. Otherwise, the optimizer iterates again and the above procedure repeats until the ratio statistic drops below 0.8.

Regression Analysis Results

Five separate tensile tests were conducted on both FHG and RFG materials. A sample of a typical stress versus time curve for the tensile tests is shown in Fig. 2.8.

There are three distinct regions. During Region 1, there is calibration error in the tensile test machine that occurs for each test. Region 2 is the period from the correction of the calibration error to the rupture of the specimen. Region 3 is the portion of the test after the specimen ruptures. Only the data from Region 2 was

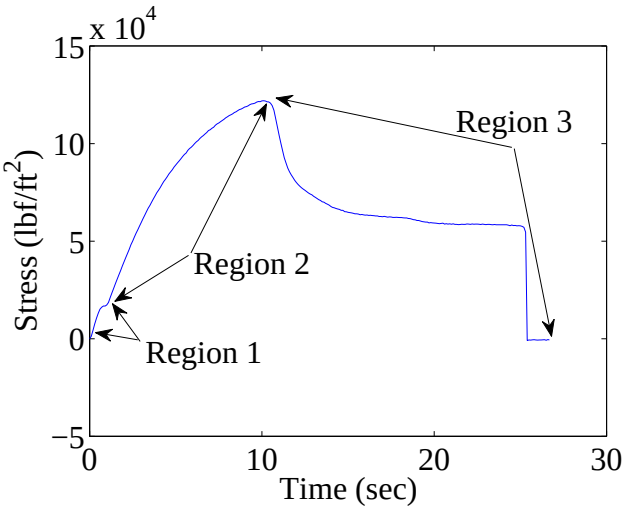

Figure 2.8: Typical stress versus time for material during tensile testing

used in the regression analysis as it is the only reliable data.

In order to be certain that the best set of viscoelastic parameters has indeed been found, the required number of independent random starts of the regression analysis optimizer must be determined. From Reference [9], in order to be c confident that at least one of the best $f \times 100\%$ results have been found, M independent random starts are required. The value of M is determined using Equation (2.60).

$$M = integer\left(\frac{\ln(1-c)}{\ln(1-f)}\right) \tag{2.60}$$

Thus, in order to be 95% confident that at least one of the best 10% results are found, the number of independent random starts of the regression analysis optimizer must be 28.

Therefore, to determine the viscoelastic parameters, the regression analysis was performed 28 times for each of the ten sets of data. The viscoelastic parameter set that corresponded to the best results were chosen to be the "true" E, E_v, and b values. Best was defined as the smallest RMS value.

The data that yielded the best results came from the FHG material. From the regression analysis, the viscoelastic parameters were determined to be: $E = 9.75 \times 10^5$

lbf/ft^2, $E_v = 9.75 \times 10^6$ lbf/ft^2, and $b = 5.01 \times 10^7$ lbf·s/ft^2. Figure 2.9 shows the data and the corresponding best-fit curve for the given viscoelastic parameters. As seen from the plot, the model fits the measured data well and thus the above E, E_v, and b values are sufficient to use in simulations.

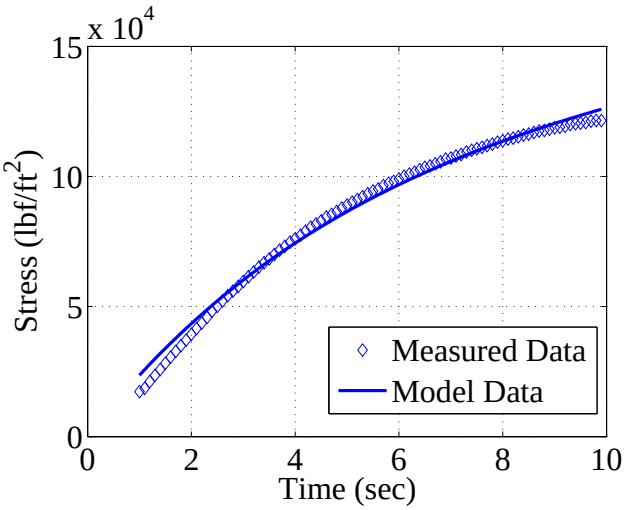

Figure 2.9: Stress versus time for measured data and best-fit model

2.4.2 Friction Torque Evaluation

The friction present in the bearings of rollers has two components: a viscous friction that is proportional to velocity and a constant friction torque. For modeling purposes, it is assumed that the viscous friction is negligible and so the majority of the bearing friction is assumed to be the constant friction torque. In order to determine an accurate value for this term, a test was performed on two typical idle rollers used in CFL. For this test, the roller was hand spun to a speed higher than the desired test speed. A hand held tachometer was used to track the speed of the roller as it slowed due only to friction. Once the speed of the roller reached the desired test speed, a timer was started and the tachometer was removed from the roller. The time for the roller to come to a complete stop was measured for ten trials.

The first test was performed on a 10.5 inch diameter roller, and all ten trials

Trial	Initial Velocity fpm	Stopping Time sec	Friction Torque (ft · lbf)
1	99.9	55.28	0.309
2	100.01	60.57	0.283
3	100.99	58.14	0.297
4	98.78	61.04	0.277
5	100.02	58.05	0.295
6	100.93	60.00	0.288
7	100.73	60.00	0.287
8	100.66	61.07	0.282
9	100.80	55.93	0.309
10	99.81	56.49	0.302

Table 2.1: Test 1 Parameters and Measurements

were performed at a test speed of 100 feet per minute (fpm). The second test was performed on a 9.5 inch diameter roller with six trials performed at a test speed of 100 fpm and four trials at 120 fpm. The results of the tests are presented in Tables 2.1 and 2.2.

To determine the friction torque, the free body diagram of the roller is used. Since there were no other forces besides friction acting on the rollers, the equation of motion for the test rollers is as given in the following.

$$J\dot{\omega(t)} = -\tau_f \tag{2.61}$$

This can be approximated as

$$J\frac{\triangle\omega}{\triangle t} = -\tau_f \tag{2.62}$$

Trial	Initial Velocity fpm	Stopping Time sec	Friction Torque (ft · lbf)
1	99.41	64.83	0.226
2	100.46	60.83	0.244
3	100.17	65.12	0.227
4	99.38	73.36	0.200
5	99.45	71.02	0.207
6	100.98	73.77	0.202
7	120.92	90.80	0.197
8	120.10	85.95	0.206
9	119.93	87.32	0.203
10	120.21	87.84	0.202

Table 2.2: Test 2 Parameters and Measurements

where J is the test roller inertia, $\triangle\omega$ is the change in velocity of the roll in $\triangle t$ stopping time, and τ_f is the friction torque. Using classical methods for determining inertia, the friction torque can be solved for assuming that it is a constant value throughout the duration of each trial. Tables 2.1 and 2.2 show the calculated friction torques for each trial using the aforementioned calculation. The average friction torque values from both tests at each target speed are displayed in Table 2.3. As can be seen from the results, the friction torques for the 9.5 in idler roller are approximately equal even though they were run at different speeds.

Test	Target Velocity (fpm)	Friction Torque (ft · lbf)
1	100	0.293
2	100	0.218
	120	0.202

Table 2.3: Average Friction Torque

2.5 Current Control Strategies

2.5.1 RSLogix5000 Operation

Before the control strategy used in this section of the CFL can be discussed, the exact functionality of the RSLogix ladder logic and its PID controller must be detailed first. Ladder logic is a programming method that uses routines containing a series of rungs that have commands which are executed in order from top to bottom. The entire control strategy of the CFL is composed of multiple tasks consisting of several routines. The tasks involve performing safety checks, computing variables, and several other duties. Only one task can be executed at a time, so each is assigned a different execution period and a priority value from 1 to 15, where 1 is the highest priority and 15 is the lowest. Each task is implemented every period, but it can be interrupted by a higher priority task that happens to occur at the same time. When this happens, the higher priority task executes completely first followed by continuation of the lower priority task from where it was interrupted [5].

On the CFL, there are three tasks that are pertinent to this report: a task that governs the rewind section of the CFL (called the STI task), one that calculates the various reference values for variables of the CFL (called the Line References task), and another that controls the status of certain line components (called the Main task). The Unwind Roll uses an RSLogix PID for tension control which resides in

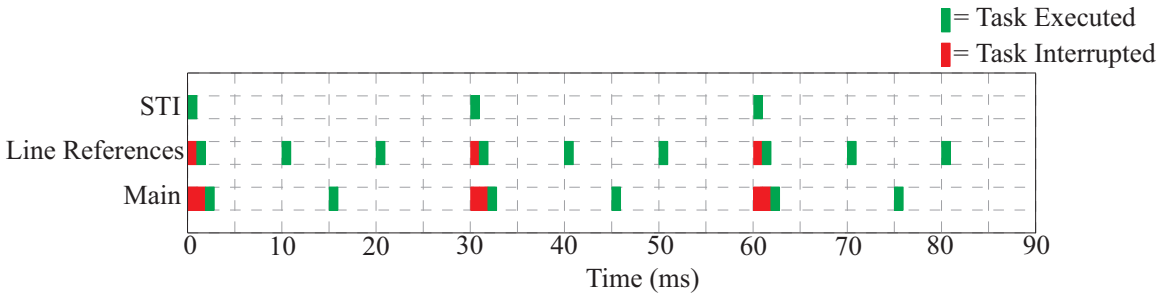

Figure 2.10: Execution times of each task[5]

the Main task whereas the PID that controls tension for both Pull Roll 1 and the Unwind Accumulator (Dancer 1 PID) resides in the Line References task. Table 2.4 lists the priorities and execution periods of each of these tasks.

Table 2.4: Priorities and Periods of RSLogix Tasks

Task	Priority	Period
STI	1	30 ms
Line References	5	10 ms
Main	6	15 ms

Figure 2.10 shows a graphic representation of the times when each of the three aforementioned tasks are implemented. Notice that every 30 ms when each task is scheduled to be performed, the STI task interrupts the other two due to its higher priority. Additionally, the scheduled execution time is constant regardless of any intrusions by a higher priority task.

Figure 2.11 shows the PID procedure used by RSLogix in block diagram form that is utilized for automatic control[6]. Table 2.5 shows the values of the Output Bias percentage, maximum (MAXI) and minimum (MINI) process variable (PV), maximum (MAXS) and minimum (MINS) engineering unit scaling value, and maximum (MAXCV) and minimum (MINCV) control variable (CV) value for the Unwind Roll and Dancer 1 controllers. The process variable is the measured feedback and the

control variable is the value output by the PID that is sent to an actuator[6].

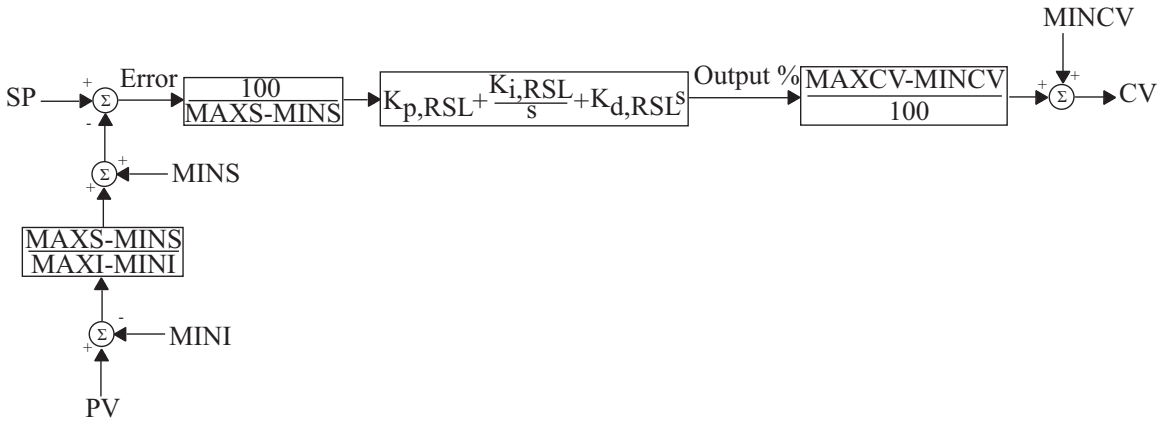

Figure 2.11: Block diagram of RS Logix PID

Table 2.5: Parameter Values Used in RSLogix PIDs

Variable	Unwinder PI	Dancer 1 PID
Bias	0	0
$MAXI$	100	100
$MINI$	0	0
$MAXS$	100	100
$MINS$	0	0
$MAXCV$	100	1.1
$MINCV$	0	0.9

The PID equation first uses the error between the SP and PV to calculate the output. Note that both the error and the output are expressed as percentages of the engineering unit range. The last step performed by the PID function as used in RSLogix is to convert the PID output percentage into the units of the control variable [6].

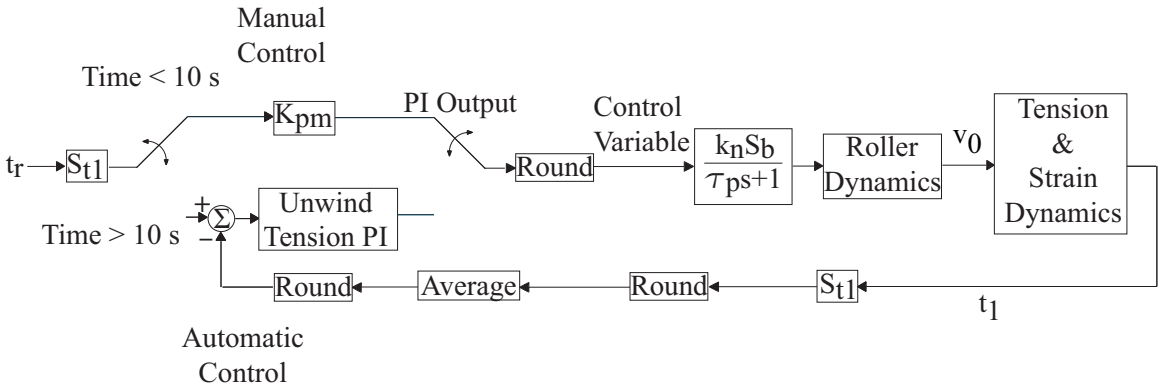

Figure 2.12: Control strategy for Unwind Roll

2.5.2 Unwind Roll Control Strategy

The Unwind Roll torque is controlled by a brake. Therefore, the rotation of the roll is due to the material being pulled by Pull Roll 1. This means that there is no direct velocity control of the Unwind Roll. Thus, there is only tension control via braking for the portion of the web line spanning from the material roll to Pull Roll 1. The tension control strategy presently being employed is shown in Fig. 2.12. This scheme has two parts: manual control and automatic control. The manual control is utilized only for the first 10 seconds after the start up of Pull Roll 1 whereafter the automatic control is employed. When the switch from manual to automatic control occurs, the RSLogix software calculates the accumulated error required to produce the same CV output that is generated by the manual control. This process results in a smooth transition from open loop to closed loop control without causing a sudden increase or decrease in the CV [6].

During manual control, a scale factor, K_{pm} in Fig. 2.12, input by an operator multiplies the tension set point to produce the PI output percentage. For the simulations

conducted in Section 3.2, K_{pm} has a value of 0.6. One reason for implementing the manual control is that it allows RSLogix to acquire 10 tension measurements so that when automatic control is initiated, the tension averaging calculation (to be discussed later) will utilize actual tension measurements as opposed to using the measurements that were recorded before the Unwind Roll was initiated.

For automatic control, web tension measurements taken by a load cell are used as feedback to produce the controller output. The tension measurements are sent to the RSLogix software as integer values where they are sampled once every second and then averaged with the past 9 tension samples. This mean, set as an integer value, is subtracted from the tension set point. This difference is used in the PI equation to produce the PI output percentage that, when rounded to the nearest integer, is the control variable.

During automatic control when the actual tension and the set point are different, the integral term of the PI accumulates this error between the two values. At the instant when the error becomes zero (thus rendering the proportional term of the PI to be zero), the integral part of the PI is able to supply the output required to maintain the desired tension because of the accumulated error. One important fact to note is that the update time for the PI is 0.2 seconds so the PI continues to integrate in between the tension samples. Thus for a large error, the brake would apply an extreme (either high or low depending on the sign of the error) and continuously increasing or decreasing amount of torque to the Unwind Roll until the next sample is measured. The PI equation is displayed in Equation (2.64) below.

The PI output percentage, computed either using the manual or the automatic method, is limited to 1% to 80%. By using Fig. 2.11 with Table 2.5, it may appear that the PI output percentage and control variable have the same numerical value. However, the control variable is set as an integer value and thus is the integer equivalent of the PI output percentage. The control variable corresponds to an out-

put voltage. This voltage is then transformed into pressure via a voltage-to-pressure (E/P) transducer. The pressure is then applied to brake pucks which generate the braking torque on the Unwind Roll. In an effort to increase efficiency, two separate unwind structures, and thus two different brakes (designated Brake 1 and Brake 2), are used so while one is supplying the CFL with material, the other can be reloaded. These brakes are individually configured and thus the configuration of the two brakes can be different (as they most often are) which, as will be seen in Section 3.4, results in dissimilar tension performances and controller outputs for a given PID controller.

The dynamics of the pneumatic device used to supply the pressure for the brakes are assumed to be first order of the following form.

$$\tau_p \dot{p}(t) + p(t) = k_n CV(t) \tag{2.63}$$

where τ_p is the time constant for the pneumatic device, $p(t)$ is the pressure within this device, k_n is the unit conversion constant from units of control variable to psi, and $CV(t)$ is the control variable value sent from the controller. In order to determine τ_p, a simple test was conducted. A step increase was made in the CV and the time required for the pressure in the pneumatic device to reach its steady state value was recorded. From elementary systems analysis, dividing this rise time by four will result in the time constant of the device given an increase in CV. This procedure was repeated for a step decrease in CV. The resulting time constants from these two tests are shown below.

$$\tau_p = \begin{cases} 1.625 & \text{for CV increasing} \\ 0.625 & \text{for CV decreasing} \end{cases}$$

The determination of k_n is discussed later.

Note that there are several scaling factors in Fig. 2.12. The factor of S_{t_1} accounts for the fact that in the RSLogix program, the tension values are represented as percentages of 400 lbf, the maximum tension that can be induced in the web by the brake when a full material roll is attached. This means that the tension PI equation

for the Unwind Roll is given by Equation (2.64).

$$O_{PI,UW} = K_{p,UW}(S_{t_1}(t_r - t_{meas}(t))) + K_{i,UW} \int S_{t_1}(t_r - t_{meas}(t)) \tag{2.64}$$

where $O_{PI,UW}$ is the PI Output, $K_{p,UW}$ is the proportional gain, $K_{i,UW}$ is the integral gain, t_r is the reference tension, and t_{meas} is the tension feedback. Since the CV is just the integer equivalent of the PI output percentage, the transformation from the latter to the former is shown in Fig. 2.12 as a rounding block.

In order to find values for k_n and S_b (the conversion from braking pressure to applied torque), the following information gathered from the control program was used. The PI is calibrated so that 100% of PI output (CV value of MAXCV for the Unwinder from Table 2.5) corresponds to 10 volts and the voltage to pressure transducer (E/P device) is set so that 10 volts corresponds to 46 pounds per square inch (psi) of pressure. Thus $k_n = (46/10) \times (10/MAXCV) = 46/MAXCV$. To determine the amount of braking torque per psi of applied pressure, the following reasoning is used. It is assumed from the RSLogix files that 100% of PI output corresponds to 400 lbf of induced tension. Since the web tension effected by the brake varies with roll radius, it is assumed that this relation was determined using a full material roll. This assumption leads to Equation (2.65) which shows the relation between brake pressure and the corresponding applied torque.

$$S_b = \frac{R_{0i} \times t_{max}}{P_{max}} \tag{2.65}$$

where R_{0i} is the initial material roll radius, t_{max} is 400 lbf, and P_{max} is the applied braking pressure corresponding to 100% of PI output. Although Equation (2.65) was derived presuming a full material roll, it is assumed that S_b is constant throughout the entire unwinding of the roll. In the model verification section (3.2) of Chapter 3, this value is adjusted in order to better match data measured from the CFL.

2.5.3 Pull Roll 1 and Unwind Accumulator Control

Pull Roll 1 uses tension feedback and velocity control. The tension control is used to produce a correction to the velocity reference value. In the CFL, the tension feedback is provided by Dancer 1 which uses the linear transducer mentioned in Section 2.3 to measure the linear displacement of the dancer. This displacement value is then passed to the ladder logics program as a percentage of the maximum transducer stroke where it is compared with the reference dancer position within a PID in the software. The PID equation is given in Equation (2.66).

$$O_{PID,D1}(t) = K_{p,D1}e_x(t) + K_{i,D1}\int e_x(t)dt + K_{d,D1}\frac{de_x(t)}{dt} \tag{2.66}$$

where $O_{PID,D1}$ is the PI Output, $K_{p,D1}$ is the proportional gain, $K_{i,D1}$ is the integral gain, $K_{d,D1}$ is the derivative gain, and $e_x(t) = 100\left(x_{tr} - x_t(t)\right)/x_{tmax}$ is the dancer displacement error as a percentage of the maximum transducer stroke. This output is scaled from 0.9 to 1.1 which will provide $\pm 10\%$ trim to the Pull Roll 1 velocity. This calculation is shown in Equation (2.67) below.

$$d_x(t) = O_{PID,D1}(t)\left(\frac{MAXCV_{D1} - MINCV_{D1}}{100}\right) + MINCV_{D1} \tag{2.67}$$

where $d_x(t)$, referred to as Dancer 1 Trim, is the output of the PID and $MAXCV_{D1}$ and $MINCV_{D1}$ are the values shown in Table 2.5 for the Dancer 1 PID. Dancer 1 Trim is not the velocity correction, but a scaling factor that, when multiplied by the reference line speed (Pull Roll 2 speed reference), gives the corrected speed reference for Pull Roll 1 when the accumulator carriage is stationary. Equation (2.68) shows the values for the Pull Roll 1 reference speed, v_{1r} for the various Unwind Accumulator phases (see discussion below).

$$v_{1r}(t) = \begin{cases} v_{ls}d_x(t) & \text{if carriage is stationary} \\ v_{ls}d_x(t) + 50fpm & \text{if filling} \\ 0 & \text{if emptying} \end{cases} \tag{2.68}$$

where v_{ls} is the line reference speed. The speed reference that is sent to the drive is the ramped equivalent of the value determined from Equation (2.68). This ramped value is calculated at every scan of the "Line References" routine and is shown in Equation (2.69) below.

$$v_{1rr}(t) = \begin{cases} v_{1rr}(t-T) + 0.2 & \text{if } v_{1r}(t) > v_{1rr}(t-T) \\ v_{1rr}(t-T) - 0.2 & \text{if } v_{1r}(t) < v_{1rr}(t-T) \\ 0 & \text{if 0.5s after emptying intiation} \end{cases} \tag{2.69}$$

where $v_{1rr}(t)$ is called the ramped velocity reference and T is the sampling period.

The velocity control for Pull Roll 1 is performed in a PID internal to a Rockwell Powerflex 700 drive attached to the motor which powers Pull Roll 1. This drive bases its PID calculations on motor speed and not web line velocity. Thus $v_{1r}(t)$ needs to be converted to motor speed, which is accomplished using the gear ratio between the drive motor and the attached roller. The drive uses speed feedback from an encoder which is attached to the motor. This value is compared to the speed reference calculated above to produce a speed error which is sent to the PID inside the drive. The PID will then provide the appropriate amount of torque in order to drive Pull Roll 1 at the desired velocity.

The control strategy of the Unwind Accumulator is as follows. When the current roll is near depletion and must be replaced, the accumulator must empty in order to supply the rest of the line with material. To begin this process, an operator presses the Unwinder Stop Push Button when the material roll is empty. In actuality, this button stops Pull Roll 1 (making its speed reference equal to zero) since it directly controls the speed of the material roll. To stop the emptying process, an operator presses the Unwinder Start Push Button (i.e., Pull Roll 1 is started) when a new material roll is ready. At this stage, the accumulator capacity is low and needs to be replenished before the next roll change. In order to begin filling the accumulator, the Unwinder Start Push Button must be pressed first and then the Accumulator

Fill Button must also be pressed. During the filling process, Pull Roll 1 is driven 50 feet per minute (fpm) faster than the line reference speed, but it is still controlled as described above. The accumulator stops filling when it reaches a limit switch located at the top of the accumulator structure.

During the emptying phase and the initial and final portions of the filling procedure, the accumulator uses tension feedback and carriage velocity control. When the carriage is moving, dancer position feedback is used to create a reference speed for the carriage in order to maintain the reference tension. This feedback is provided by Dancer 1. The calculated Dancer 1 Trim from Equation (2.67) is multiplied by the speed reference for Pull Roll 2. This product is then subtracted from the ramped speed reference for Pull Roll 1 for the corresponding accumulator phase. This difference, when divided by the number of accumulator spans, gives the speed reference for the accumulator carriage. The calculation of the reference speed for the carriage, v_{cr}, is shown in Equation (2.70).

$$v_{cr}(t) = \frac{1}{N_{Ac}} \left(v_{1rr}(t) - v_{ls} d_x(t) \right) \tag{2.70}$$

Note that at the initiation of the emptying process, $v_{1r}(t)$ will be set to zero but the ramp defined by Equation (2.69) is allowed to work for another 0.5 seconds. This allows the accumulator carriage to accelerate per Equation (2.70). Afterwards, $v_{1rr}(t)$ is set to zero. As will be seen in Chapter 5, this sudden step in the ramped reference causes a speed mismatch between Pull Roll 1 and the Unwind Accumulator. Once Pull Roll 1 has accelerated to the nominal fill speed, the carriage will have a constant speed reference of $50/N_{Ac}$ since the $v_{ls} d_x(t)$ terms from Equations (2.68) and (2.70) will cancel. Therefore, during this time, the accumulator will be under speed control only.

The velocity control of the accumulator carriage is performed using a Powerflex 700 drive. The drive is attached to a motor which, through a series of gears and turn

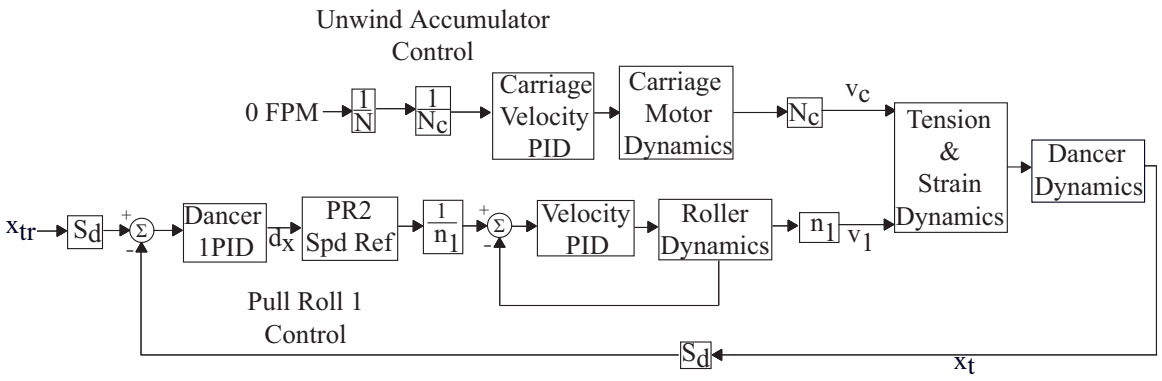

Figure 2.13: Control strategy for Pull Roll 1 and Unwind Accumulator under normal operating conditions

screws, raises and lowers the carriage. The feedback used internally in the drive is the encoder measured motor speed, not the carriage velocity. Thus, the calculated carriage reference speed as given by Equation (2.70) above is converted into motor speed using the gear ratio that determines the amount of linear displacement of the carriage per revolution of the drive motor. The feedback measured from the encoder is subtracted from this reference value. This error is then used in the drive's PID in order to actuate the motor to the speed that will produce the desired carriage velocity. See Figs. 2.13 to 2.15 for the control strategies of Pull Roll 1 and the Unwind Accumulator under normal operating conditions, while emptying, and while filling.

2.5.4 Pull Roll 2 Control

Pull Roll 2 is the Master Speed Roll for the entire CFL and therefore does not use tension feedback to control its motor speed. The only control utilized for Pull Roll 2 is the speed control performed internally in the Powerflex 700 drive. This drive operates exactly like the drive for Pull Roll 1 except the speed reference is not provided by a dancer but is a constant value that is input by an operator. See Fig. 2.16 for the block diagram depicting the control strategy for Pull Roll 2.

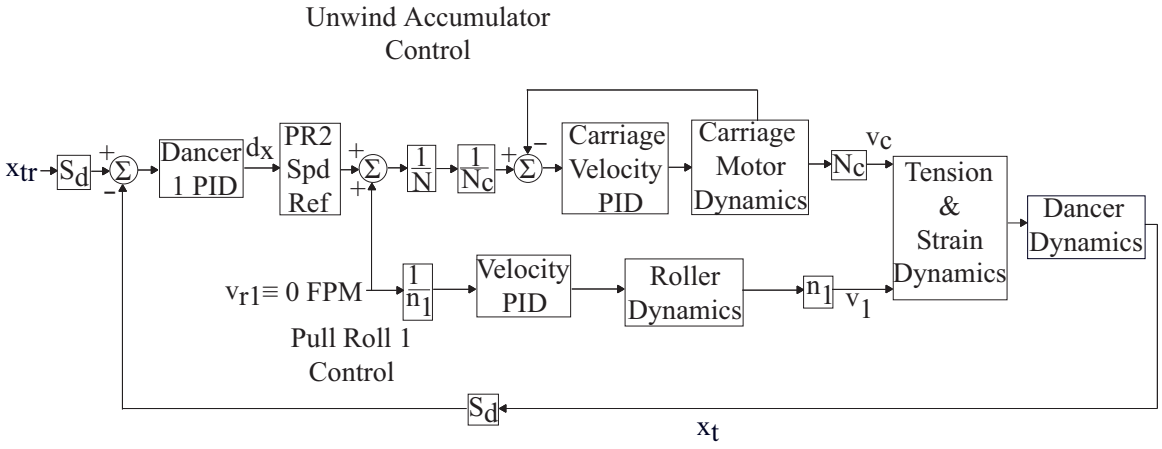

Figure 2.14: Control strategy for Pull Roll 1 and Unwind Accumulator while emptying

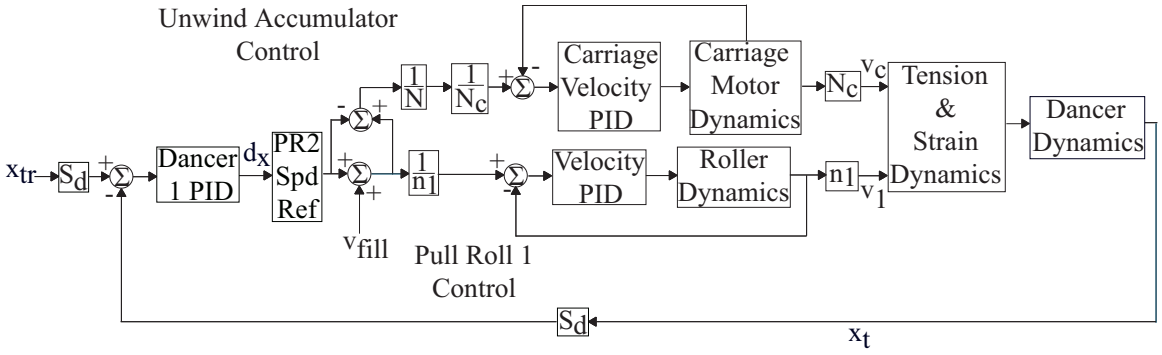

Figure 2.15: Control strategy for Pull Roll 1 and Unwind Accumulator while filling

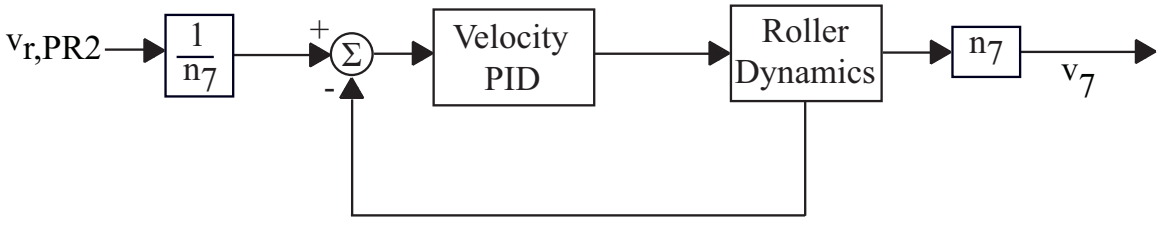

Figure 2.16: Control strategy for Pull Roll 2

2.6 Conclusion

The equations, parameters, and control strategies presented herein will be utilized in the subsequent chapters. The dynamics and control strategies associated with the Unwind Roll are used in Chapters 3 and 4. In Chapter 3, this data will be utilized to develop a simulation model and derive improvements for the current control strategy. In Chapter 4, the linearized dynamics are employed in a technique that compares the stability regions for systems with velocity and torque controlled Unwind Rolls. The control strategies and dynamics corresponding to Pull Roll 1, the Unwind Accumulator, Dancer 1, and Pull Roll 2 are used in Chapter 5 to generate a model simulation which is utilized to analyze and improve upon the current control strategies for Pull Roll 1 and Unwind Accumulator.

CHAPTER 3

Analysis of Unwind Roll Control and Improvements

3.1 Introduction

This chapter discusses the modeling and analysis of the existing control strategy of the Unwind Roll. The analysis will be based on a model simulation using the control strategy described in Subsection 2.5.2. The credibility of the model will be based on comparison of the model output with data measured from the CFL. Based on the deficiencies of the current control strategy, three strategies will be derived with the goal of improving the tension performance. Each of these strategies are simulated and compared with the results obtained using the model of the existing strategy. Experiments are then performed on the CFL to test the effectiveness of these modifications.

In this chapter, Section 3.2 discusses the verification of the system model. The improvements to the existing strategy are presented in Section 3.3, followed by the results of the experimental implementation in Section 3.4. Section 3.5 concludes this chapter with a discussion of the results obtained herein.

3.2 Model Verification

This section discusses the model verification for the system presented in Fig. 2.7. A model simulation is conducted that employs the control strategy for the Unwind Roll as described in Subsection 2.5.2 as well as the mathematical models given by Equations (2.1), (2.7), (2.8), and (2.63), which describe the relevant dynamics. It is

assumed that Pull Roll 1 is running at the reference velocity profile shown in Fig. 3.1. This figure was constructed by assuming that the Pull Roll 1 velocity is the speed reference that would be commanded if Dancer 1 is at its reference position. This simplification allows for the analysis of this section of the CFL. An S-curve instead of step changes in speed was also implemented in order to facilitate realistic speed changes.

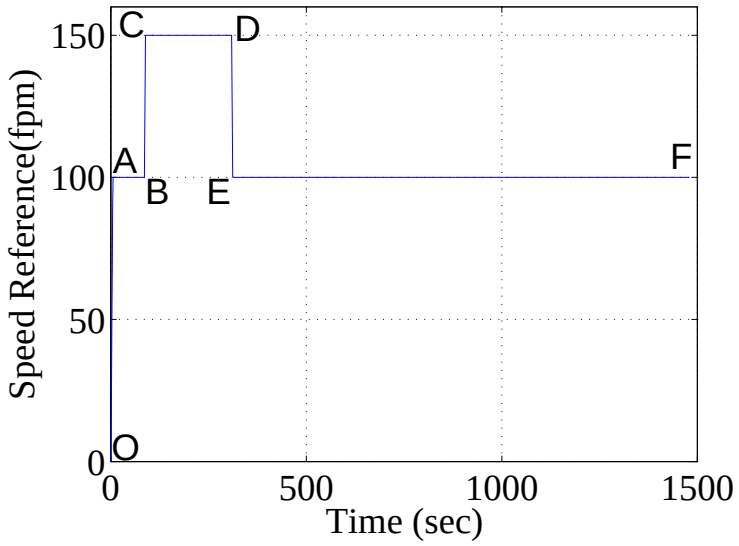

Figure 3.1: Velocity profile of Pull Roll 1

This profile represents a scenario that shows all of the speed changes from the initiation of a new roll to roll depletion. The reference speed has six phases: initial startup to line speed (OA), holding constant at line speed (AB), ramping up to 50 feet per minute (fpm) greater than the line speed (BC), holding constant at 50 fpm plus line speed (CD), decelerating to line speed (DE), and holding constant at line speed until roll depletion (EF). The first two segments are used to advance the web splice that connects the new roll to the previous one through the accumulator. The line speed is maintained in AB in order to keep the accumulator carriage stationary since it will not move when the speed reference for Pull Roll 1 is equal to the line speed. This procedure is used because the web splice may not be able to endure the

increased stresses associated with the web passing through an accumulator when it is filling. Segments BC and CD fill the accumulator. This is possible since the web upstream is moving faster than the web downstream and thus the carriage must rise in order to maintain the web tension and velocity. At D, the accumulator is nearly full and thus Pull Roll 1 and the accumulator carriage must decelerate, a process that happens during DE. Segment EF shows the Pull Roll 1 speed reference when the accumulator carriage is at its maximum height and stationary. Since the carriage is not moving, the speed reference for Pull Roll 1 will be the line speed [2]. The time span during the constant velocity phases were approximated from data collected from the CFL.

3.2.1 Parameter Values and Initial Conditions

Tables 3.1 and 3.2 show the parameter values and the initial conditions that were employed in the simulation. The constant friction torque acting on the Unwind Roll was determined from the friction torque test discussed in Subsection 2.4.2. This is an estimate since the friction test was conducted on idle rollers and a similar test was not performed on the Unwind Rolls. The controller gains currently used on the CFL were selected for $K_{p,unw}$ and $K_{i,unw}$. The web thickness, t_w, and density, ρ_w, were measured from CFL web samples. The length of Span 1, L_1, and the lateral web width, b_w, were obtained from a drawing of the physical line. Since the model shown in Fig. 2.7 ignored the idle rollers in this section of the CFL, the resonant frequencies introduced by these idle rollers are also ignored and an average tension model is used. Thus, L_1 is selected to be the average length of the spans between the first Unwind Roll and Pull Roll 1. The web cross-sectional area, A, was calculated as the product of t_w and b_w. E, E_v, and b are selected to be the values determined in Subsection 2.4.1. The initial Unwind Roll radius value was calculated by the following procedure. The length of material for one roll was determined by integrating the velocity profile

curve. As the volume of the material laying flat is the same as that of the wound material, this length was related to the initial material roll radius. This relationship leads to Equation (3.1), which gives the initial radius of the material roll. The initial tension of 12 lbf was selected because that is the same value as the measured data at the beginning of a new material roll.

$$R_{0i} = \sqrt{\frac{L_w t_w}{\pi} + R_{c0}^2} \tag{3.1}$$

Table 3.1: Parameter Values Used in Simulation

Variable	Value Used in Simulation	Units
$K_{p,unw}$	0.5	None
$K_{i,unw}$	0.005	$\sec^{-1}$
t_w	0.003833	ft
ρ_w	3.182	slug/ft^3
b_w	12.25	ft
A	0.04696	ft^2
E	9.75×10^5	lbf/ft^2
E_v	9.75×10^6	lbf/ft^2
b	5.01×10^7	$\text{lbf} \cdot \text{s/ft}^2$
L_1	4.5	ft
τ_{f0}	0.293	$\text{ft} \cdot \text{lbf}$

3.2.2 Model Simulation Results

The results of the conducted model simulation are shown in Figs. 3.2 through 3.6. Note that three repetitions of the same simulation are shown for clarity when comparing these results with the measured data from the CFL. For simplicity, results of

Table 3.2: Simulation Initial Conditions

Variable	Initial Condition
Unwind Roll Radius, R_0	22 inches
Unwind Roll Velocity, v_0	0 fpm
Span 1 Tension, t_1	12 lbf

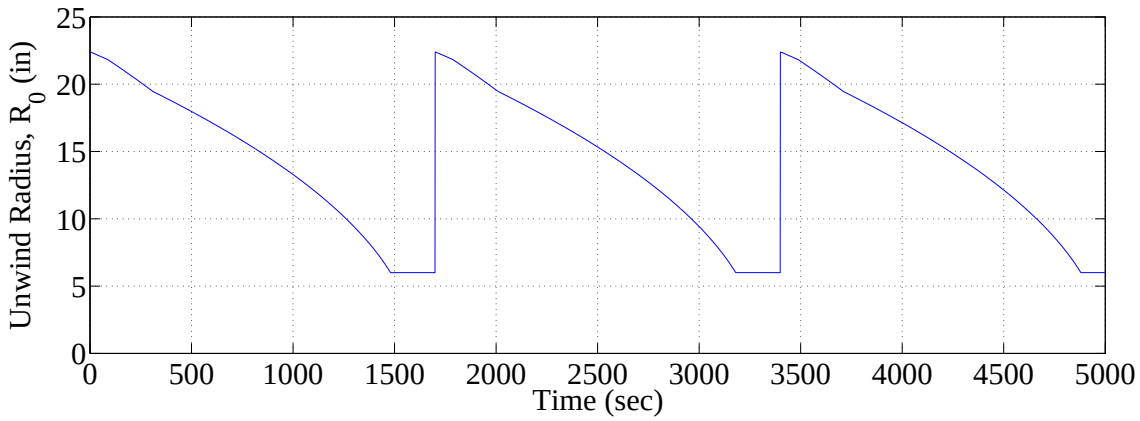

Figure 3.2: Unwind Roll radius (Model Simulation)

the model simulation are referred to as "simulated" data (i.e., the resulting tension data from the model simulation is referred to as the "simulated tension").

Figure 3.2 shows the material roll radius. The radius of the core that the material is wound upon is 6 inches and thus when $R_0(t)$ is equal to this value, the material roll will be completely depleted. The material roll is seen to be completely empty at the end of the simulation, as desired.

Figure 3.3 shows the CV of the Span 1 tension PI controller. As expected, it is constant during the manual control phase. After an initial drop, the CV is seen to oscillate between values of 13 and 15 for approximately the first 300 seconds. Beyond this time, the CV begins to decrease since R_0 is decreasing. A smaller Unwind Roll radius conveys that the material roll has a lower inertia and thus requires less braking torque to slow its rotation. This implies that it becomes easier to produce tension

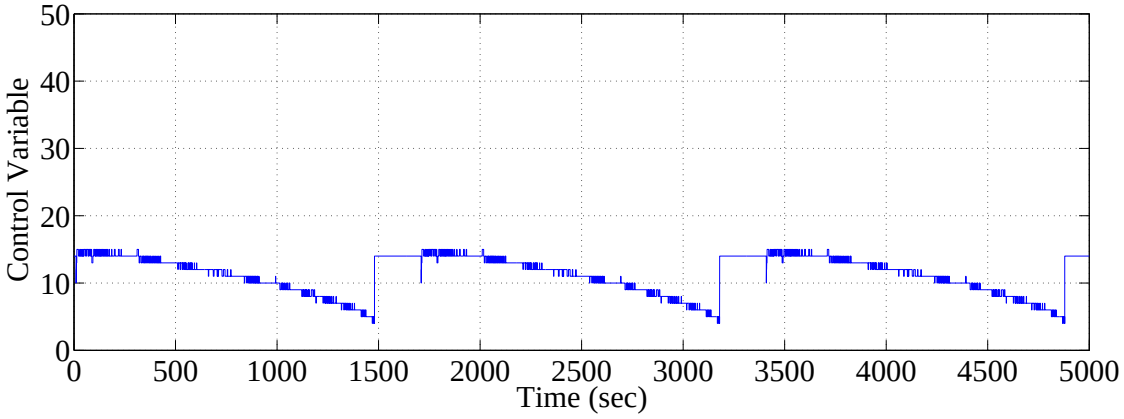

Figure 3.3: Control variable for Span 1 with tension PI (Model Simulation)

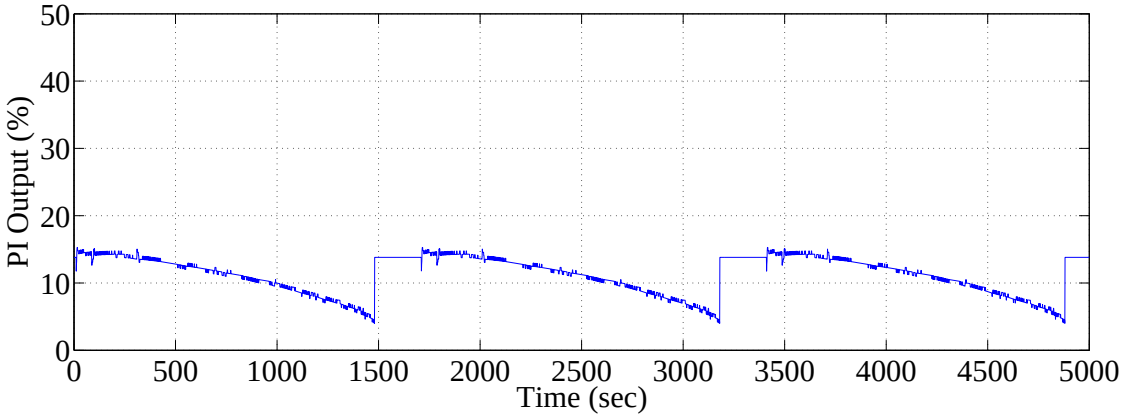

Figure 3.4: PI controller output percentage (Model Simulation)

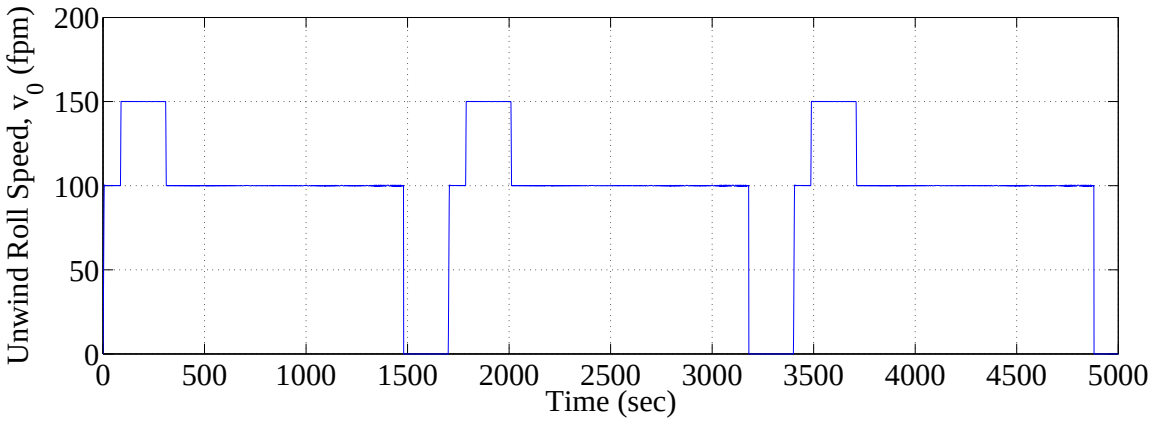

Figure 3.5: Unwind Roll peripheral velocity (Model Simulation)

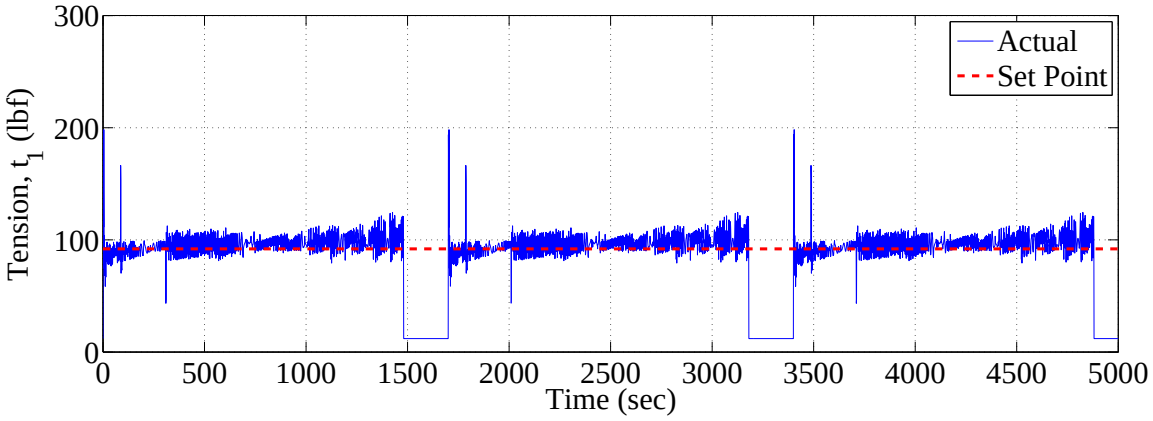

Figure 3.6: Span 1 tension (Model Simulation)

in Span 1 since the change in tension is a function of the upstream and downstream roller velocities. Moreover, braking torque induces tension in Span 1 by Equation (3.2) and hence as the material roll radius wanes, the braking torque required to effect the same amount of tension in Span 1 also reduces.

$$\tau_{braking} = R_0 t_{ind} \tag{3.2}$$

where $\tau_{braking}$ is the applied braking torque and t_{ind} is the corresponding induced tension.

During the simulation, the CV oscillates at times of transition between subsequent values. This occurs since the CV can only take on integer values. In situations where less braking is required, the PI output has to decrease by an entire percentage before a change in the CV will occur. While the PI output is decreasing, the brake is applying approximately the same amount of resistive torque which means the tension will continue to rise. Once the PI Output reaches a value such that the CV changes, the change in braking torque may decrease too much, depending on the Unwind Roll radius. If this situation occurs, the tension will drop below the reference value, causing a rise in the PI output percentage, which, once it becomes large enough, will increase the CV to a value equal to or higher than it was initially. This cycle would repeat until the braking torque corresponding to the lower CV value is sufficient to keep the

tension at the desired value. As the radius decreases, these oscillations will occur more frequently since the drop in braking torque induces more tension as previously discussed. Hence it can be seen that these oscillations are due to the inability of the CV to take on the exact value calculated by the PI equation. The oscillations are also due to the slow reaction of the brake due to the dynamics of the pneumatic device. Once the CV changes, the pressure will also change but at a slower rate. This will cause errors in tension since the brake is not applying the amount of torque that is commanded by the controller. The controller will then alter the CV in order to correct for these tension errors, resulting in more CV oscillations.

Comparing Figs. 3.1 and 3.5 shows that the Unwind Roll velocity generally follows the reference velocity relatively well. However, there are relevant differences during transitions from ramped to constant velocity and during the CV oscillations described above. Since the Unwind Roll rotation comes solely from Pull Roll 1, there is velocity error in the transition from constant velocity to acceleration of Pull Roll 1. At times when Pull Roll 1 decelerates (transitioning from BC to CD and from CD to DE from Fig. 3.1), the large inertia of the Unwind Roll causes it to overshoot the Pull Roll 1 velocity. This occurrence also contributes to the velocity error. Additionally, when the CV oscillates, the applied braking torque also oscillates causing deviations of the Unwind Roll velocity from the reference. As the roll radius decreases, the applied braking torque during the CV oscillations has a greater effect on the Unwind Roll velocity due to the smaller inertia. This causes the velocity oscillation amplitudes to grow as the simulation progresses as witnessed in Fig. 3.7 which shows the Unwind Roll velocity during the EF portion.

The tension in Span 1 is displayed in Fig. 3.6. During the manual control phase, the tension starts at 12 lbf then increases to 193 lbf before returning to approximately 75 lbf. The reason for this trend is that at the initial start up, a large amount of tension is required to accelerate the stationary Unwind Roll. The tension drop after

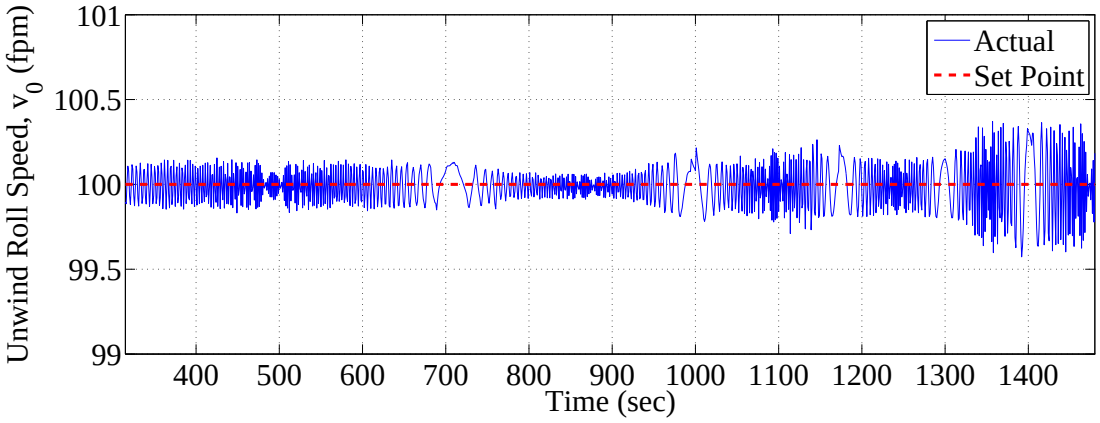

Figure 3.7: Unwind Roll velocity during EF portion of roll (Model Simulation)

the spike is a result of the Unwind Roll overshooting the velocity of Pull Roll 1 as explained above. Since the peripheral speed of the upstream roll is greater than that of the downstream roll, the tension in Span 1 decreases. The velocity error is also significant during the other Pull Roll 1 speed changes and transitions which causes the tension variation to be large during these times, as is seen in Fig. 3.6. The CV oscillations also cause fluctuations in tension. Since the pneumatic device is slow, the braking pressure is not able to match the changes in CV. Meanwhile, this changing pressure is causing the brake to vary the velocity of the Unwind Roll, as discussed above, which induces fluctuations in the tension. As was the trend with the Unwind Roll velocity, the tension oscillations become larger as the material roll radius decreases, a fact that is shown in Equation (3.2). Since changes in the CV correspond to similar changes in braking torque for both a larger roll and smaller roll, the induced tension will increase as the material roll decreases. The final trend seen in the simulated tension is that the tension drifts and does not oscillate about the reference value of 92 lbf but rather 100 lbf.

In summary, the model simulation displayed characteristics expected from the system shown in Fig. 2.7 under the given conditions. To further verify this model, the above results are compared with measured data from the CFL in the subsequent

section.

3.2.3 Measured Data From the CFL

As discussed in Subsection 2.5.2, two separate brakes are alternately used in the control of the Unwind Roll. Thus the measured data analysis is segregated into two sections, each comparing the measured data to the model simulated data. There are three sets of data for each brake. For Brake 1, the first data set was collected on a separate day than the data sets for the latter two sets. For Brake 2, each data set was collected from a different day. Thus the differences in the data for a given brake are attributed to several factors, namely, the Pull Roll 1 velocity profile, the web material, and the particular configuration of the brake.

Brake 1

Figures 3.8 through 3.10 show the measured data for Brake 1. The beginning of each run is the instant that the Pull Roll 1 velocity increases from 0 fpm. Since the Unwind Roll velocity is not measured, Pull Roll 1 velocity is displayed so that the tension and control variable data can be correlated to the action of Pull Roll 1. The first roll operated at the same speeds that the simulations were conducted; however, it does have additional velocity changes during the portion where the Pull Roll 1 velocity is supposed to be near the line speed reference. The latter rolls have a profile shape similar to that of Fig. 3.1, but are ran at slower speeds. Despite these differences between these measured velocities and the velocity profile used in the model simulation, the comparison of the tension and control variable results are still valid.

As expected, the control variable is constant for the first 10 seconds of each roll and then changes based upon the tension. Note that the constant portions at approximately 1500 seconds and 3400 seconds are observed because the controller provides

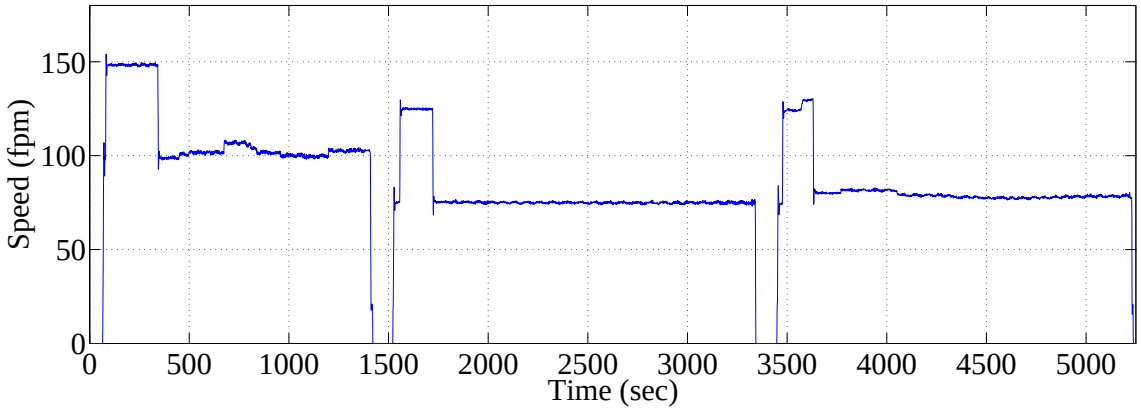

Figure 3.8: Pull Roll 1 velocity using Brake 1 (Measured data)

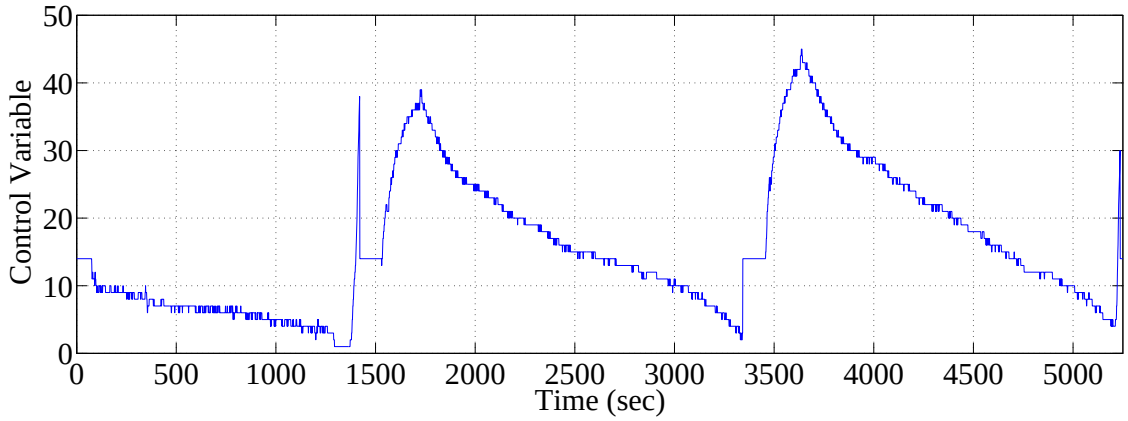

Figure 3.9: Control variable using Brake 1 (Measured data)

a constant braking torque at both the beginning and at the end of material rolls. The large spike seen at the end of the first and third runs is because the brake pressure was very low (in the case of the former, the controller actually saturates), thus causing the tension to drop. However, due to the sampling of tension values and the slow sampling time, the controller cannot immediately react to these changes. Eventually, as the tension drops lower and lower, the current and accumulated errors becomes large, resulting in a drastic increase in the control variable. Except for the first data set, the control variable is seen to gradually rise to its maximum value and then continually and gradually decrease throughout the entire roll. These same trends are observed in

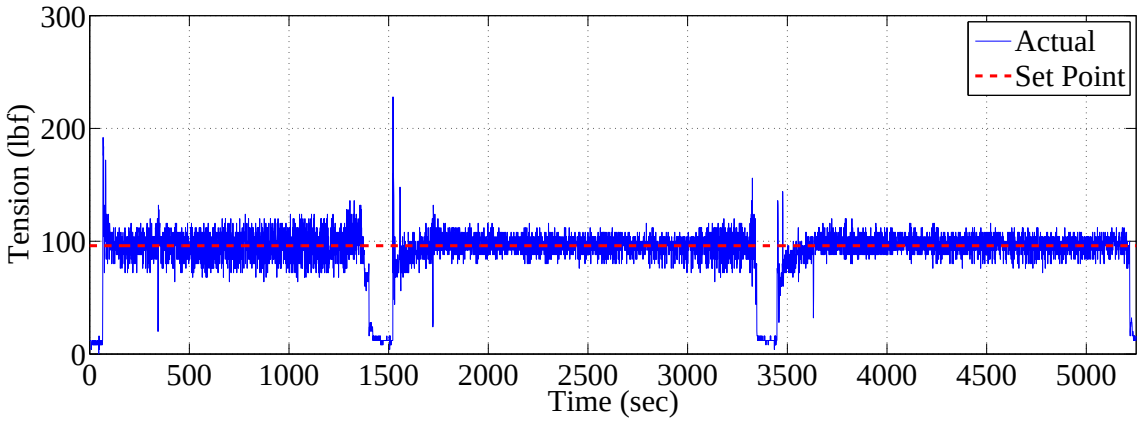

Figure 3.10: Tension in Span 1 using Brake 1 (Measured data)

the first data set, excluding the initial increase in control variable. For the particular system configuration, the initial CV was large enough to quickly increase the tension, eliminating the need to increase the CV once automatic control was initiated.

Comparing Figs. 3.3 with 3.9 shows that the simulated controller follows the same trends as those seen in the first set of measured data; they both use similar magnitudes during the automatic control phase and they both continually decrease throughout the depletion of the Unwind Roll. Additionally, the CV jumps seen in the simulation data are also present in the first set of measured data.

On the other hand, the model simulation did not accurately portray the CV trends seen in the second and third measured data sets. However, the difference is not significant since disparities in magnitude can be seen even between different sets of measured data. Thus for the simulated controller, the assumptions that related the controller output to the applied torque were for only a particular brake configuration.

The measured tension data is shown in Fig. 3.10. Each data set begins with a large tension spike as Pull Roll 1 accelerates from 0 fpm, another spike as Pull Roll 1 accelerates from line speed, and then a drop in tension as Pull Roll 1 decelerates back to line speed after the accumulator has been filled. For the second and third data sets, the tension does not reach the reference value until approximately 130

and 160 seconds after initiation, respectively. The reason is that the slow increase in their respective control variables gradually increases the braking torque, causing the tension to slowly increase. This trend is not seen in the first data set because, as discussed previously, the initial CV was large enough to produce tension values near the set point. Near the depletion of their respective rolls, the first and third data sets are seen to decrease and the second data set begins oscillate with increasing amplitude. The reason for the former trend has been discussed already, however, note that although both control variables spiked at the end of their respective rolls, the tension did not respond. The reason is that the web had already released from the core and thus any changes in the brake would not effect the tension. For the second data set, the cause of the increasing oscillation amplitudes can be attributed to two factors: (1) the gains are not appropriate for the smaller roll size and (2) the CV fluctuations are inducing tension oscillations as discussed in Section 3.2.2.

Comparing Figs. 3.6 and 3.10 illustrates that the simulated tension follows the general trends of the measured tension with a few exceptions. The simulation sufficiently modeled the large spikes during Pull Roll 1 speed transitions, but did not show the tension drop at the end of the roll that was present in the first and third data sets. However, the simulated model did display the increasing oscillation amplitudes seen in the second data set. The simulated data also has similar tension magnitudes seen in the first and second measured data sets.

On the other hand, the measured data sets each oscillated about their corresponding reference values, a trend that the simulation was unable to accurately predict. However, consider Fig. 3.11 which shows the tension in Span 1 using the same model except with the integral gain five times larger. Note that the tension drift has been reduced and the tension oscillates about the set point. This indicates that the model is lacking some unknown scaling or gain that is present within the hardware. Additionally, the model did not accurately predict the oscillation frequency that was seen

in the measure data. One possible reason for this can attributed to the model relating the braking pressure to applied braking torque. The braking pressure inflates the brake pucks which apply a force on the Unwind Roll, causing the frictional torque. These dynamics were modeled using a constant gain, but the actual dynamics are more complicated and may exhibit stick-slip phenomena due to the intermittent force applied by the brake pucks on the brake cylinder. Other possible factors contributing to the difference in oscillation frequency is the span length that was used in the model and that all of the idle rollers were ignored. The various spans between the Unwind Roll and load cell in the actual CFL contribute to the tension dynamics and can therefore influence the tension oscillation frequency observed in the load cell data.

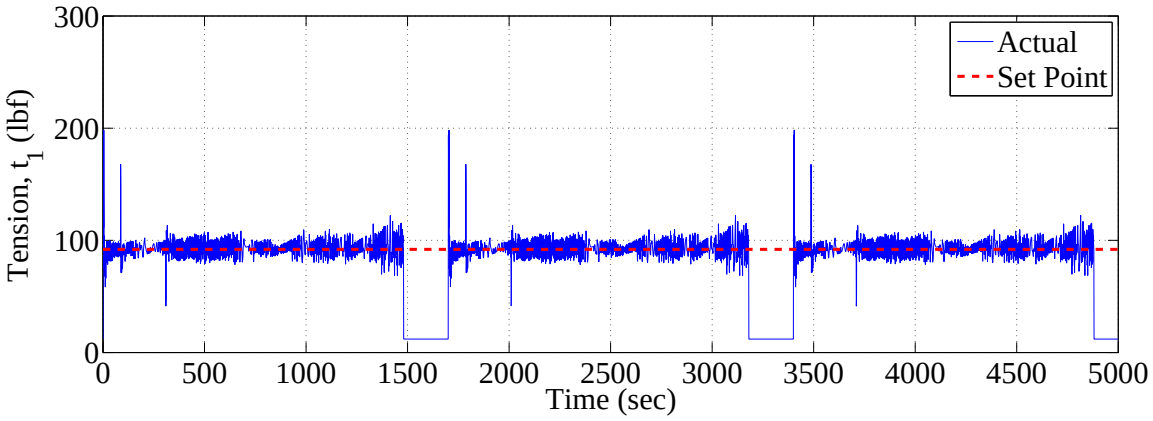

Figure 3.11: Span 1 tension using controller with increased $K_{i,unw}$ (Model Simulation)

Brake 2

Figures 3.12 through 3.14 show the measured data using Brake 2. The first and third data sets are operated at similar speeds that are seen in Fig. 3.1, while the second data set has lower speeds. All of the data sets have speed profiles that are similar to the simulated data. Thus, this data is comparable to the scenario presented in the simulation and can be used for model verification.

The trends seen in the control variable for Brake 2 are very similar to Brake 1

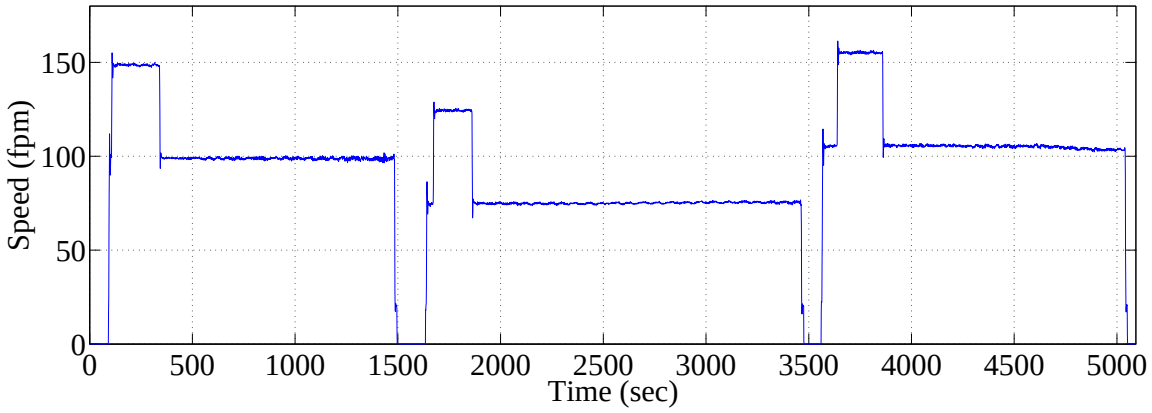

Figure 3.12: Pull Roll 1 velocity using Brake 2 (Measured data)

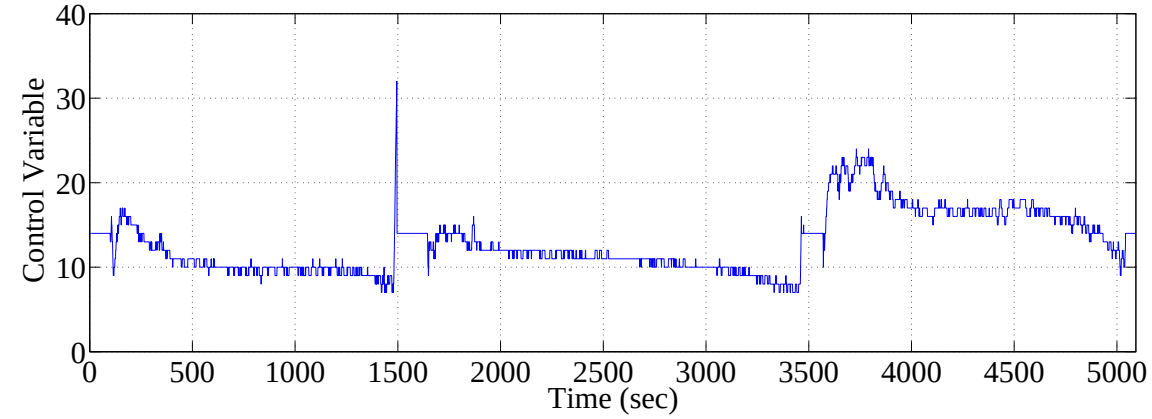

Figure 3.13: Control variable using Brake 2 (Measured data)

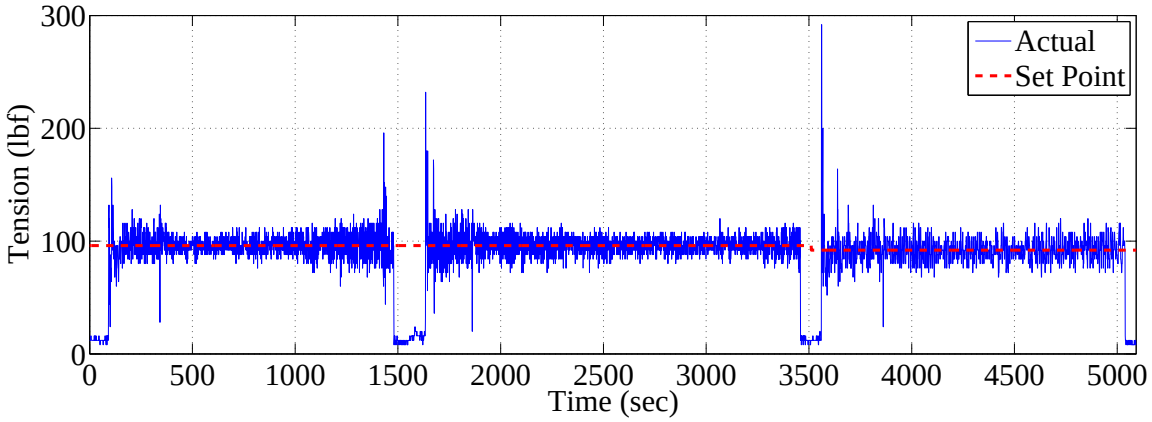

Figure 3.14: Tension in Span 1 using Brake 2 (Measured data)

except for one major aspect. While using Brake 1, the CV slowly increased to a maximum and then gradually decreased throughout the roll. The CV for Brake 2, however, quickly rises to the maximum and does not have a gradual decrease; there are large durations where the control variable is nearly constant. This is explained by the brake being configured such that a small decrease in CV results in a large decrease in braking torque. This causes the CV fluctuations as the controller is attempting to provide the correct amount of torque.

The simulated control variable shown in Fig. 3.3 is comparable to the first two measured data sets in Fig. 3.13. The first similarity is that the magnitudes shown in the simulation are relatively close to those seen in both of the measured data sets. Another trend that illustrates the correspondence is the presence of the CV oscillations.

However, the simulated data gradually decreases throughout the entire roll and does not stay constant for large portions of time, a trend seen in the measured data. Additionally, the model simulation was not able to match the magnitudes observed in the third data set. However, as mentioned above, this is not a significant difference since the CV magnitude is seen to vary between the various measured data sets for the same brake.

The tension data produced using Brake 2 followed similar patterns to those seen with Brake 1. There are large tension spikes during Pull Roll 1 acceleration and a drop in tension whenever Pull Roll 1 decelerates back to line speed after filling the accumulator. However, the tension reached the reference value much faster with Brake 2, and this can be attributed to the faster rise in the CV that was seen in the Brake 2 data. For the first data set, the tension begins to oscillate with increased amplitude as the material roll depletes. This trend is also slightly present in the second and third data sets, but is not as pronounced.

The simulated tension data in Fig. 3.6 displays the general trends found in the

measured data in Fig. 3.14. As was the case with Brake 1, the simulated data matches the tension spikes at the Pull Roll 1 speed changes. Additionally, the oscillations of increasing amplitudes found in the measured tension were also present in the simulation. The time required for the simulated tension to reach the reference value was also similar to that observed in the measured data.

However, as with Brake 1, the measured tension for Brake 2 was also able to oscillate about the reference value, a feat that was not accomplished in the simulated data. Additionally, the oscillation frequency observed in the measured tension was not accurately predicted by the model simulation. The reasons for these differences are the same as those described in the Brake 1 discussion.

3.2.4 Summary

This analysis showed that the dynamic models, though unable to match the measured data perfectly, are able to predict several trends seen in the data collected from the CFL. The simulation was able to mimic the tension effects during the speed changes of Pull Roll 1 for both brakes. The model also produced tension values similar to those seen in the data. Another aspect present in the tension data of both brakes that was captured by the simulation were the oscillations of increasing amplitudes. Additionally, the time required for the simulated tension to rise to the reference value was similar to that observed in the measured data for both brakes. The control variable signal from the model simulations displayed the general attributes that were present in certain data sets of Brakes 1 and 2. The simulated CV showed continual decrease that was observed in each of the three data sets for Brake 1, but was only able to match the magnitudes of the first data set. Conversely, the model was able to match the CV magnitudes of the first two data sets of Brake 2, but did not show the large durations of nearly constant CV present in the Brake 2 data. Control variable fluctuations were also present in both brakes, a trend that was observed in

the simulated CV as well.

However, there were aspects that were not modeled well by the simulation. One such characteristic is the steady state error observed in the tension of the model simulation. The measured tension for both brakes oscillated about the set point value, but the simulated tension did not. As described in the previous discussions, by increasing the integral gain in the model, the steady state error is reduced. This indicates that the model is missing a scaling or a gain factor. The measured tension oscillation frequencies were also not perfectly matched by the model. This can be attributed to three possible causes: the model relating braking pressure to friction torque, the span length used in the model simulation, and the absence of the idle rollers in the model.

Another aspect that was not well predicted by the simulation was that the CV values for the second and third data sets for Brake 1 showed a large initial increase after the switch from manual control. Additionally, the CV magnitudes of these two data sets were not matched by the model simulation. For Brake 2, the measured CV showed large portions that were nearly constant, a trend not observed in the model simulation. The modeled CV also did not match the CV magnitude that was achieved in the third data set for Brake 2.

Despite the shortcomings of the simulation, the major trends of the tension data were adequately predicted. The CV values between the two brakes are different as are the CV values for the three data sets for the same brake. Thus, it would not be possible for the simulation to match the CV trend of each data set for both brakes. However, the simulated CV did have certain attributes from each brake. When it did not accurately predict an aspect of one of the brakes, it matched this same characteristic aptly with the other. Therefore, the developed model sufficiently represents the portion of the CFL shown in Fig. 2.7.

3.3 Strategies For Improvement of the Existing Control Strategy

This section contains a simulation based case study of three suggested improvements to the current control strategy employed to control the Unwind Roll. The first strategy is to decrease the tension measurement sampling time and increase the resolution of certain variables. The second strategy is similar to the first except that the PI gains will vary as a function of the radius. Lastly, the third strategy implements feed-forward control action as well as the improvements employed in the second strategy.

As discussed in Section 2.5, the current control algorithm for the Unwind Roll has the tension feedback and the control variable set as integers. Moreover, due to the scaling within the input modules, the resolution of the tension measurements is 0.25 values per lbf (vpl), where resolution is defined as given below.

$$r = \frac{N_v}{R} \tag{3.3}$$

where r is the resolution and N_v is the number of values that the parameter takes over the range of values R. For example, the tension as measured by the controller takes only one value for tension values that lie in 98 lbf and 102 lbf (98 lbf $\leq t_1(t) <$ 102 lbf), and thus the resolution is $r = 1/(102 - 98) = 0.25$ vpl. These factors dilute the tension data so that the controller is not utilizing accurate data. Since the control variable (CV) is an integer, the controller does not output the required amount with suitable precision, causing large fluctuations in tension. Moreover, the resolution of the CV is one, restricting the number of specific torque values that are able to be applied. The voltage sent from the controller to the brake pressure device is directly related to the CV. Therefore, if the CV can only assume a fixed number of values, the voltage, and hence the pressure, can also only maintain certain values.

Additionally, the sampling period of the tension measurements is one second with the PI controller update time as 0.2 seconds. This means that the controller output is updated every 0.2 seconds but the error only updates every second. Thus, the

controller is just an integrator 0.8 out of every one second rendering the system to be open loop the majority of the time. This results in inaccurate control since the applied torque is not reacting to current errors in tension.

Lastly, the controller used constant PI gains throughout the entire roll. For systems that are time invariant, this would acceptable. However, the inertia of the Unwind Roll changes as the web is continuously released from the roll and the radius decreases. This will cause a set of PI gains to be sufficient near the beginning of the new roll (full roll) while causing the tension performance to be degraded later. There are two solutions to this problem. The first is to define fixed gains such that the system remains stable throughout and allow for decreased performance. The second is to vary the gains as a function of the radius so that the system remains stable and satisfactory performance is achieved for all radii of the material roll.

Each of the simulations conducted in Subsections 3.3.1 through 3.3.3 employed the model shown in Fig. 2.7 and the velocity profile from Fig. 3.1. Unless otherwise specified, the web properties from Table 3.1 and the initial conditions shown in Table 3.2 were utilized as well. As in Subsection 3.2.2, for each simulation, three repetitions of the same data are shown for clarity of comparison.

3.3.1 Strategy 1

As discussed above, the controller output and feedback measurements should be updated as often as is practical and that they be as accurate as possible. Moreover, to avoid the complications of multi-rate control systems, the controller update and measurement rates should be the same. Thus the current control strategy for the Unwind Roll is not ideal since it has different rates for updating the controller and measuring the feedback data in addition to using integer values. Strategy 1 is aimed at rectifying these shortcomings.

The first change is reducing the tension measurement sampling time from one

second to 0.2 seconds. This will allow the controller to react to the most recent data, increasing the relevancy of the control action. Another benefit is that the controller will update at the same rate as the tension measurement, eliminating the need for analysis of the system as a multirate system.

The second improvement seen in Strategy 1 is changing the scaling on the CV and the measured tension as well as setting the average tension as a floating point number. As mentioned above, the current scaling results in a tension resolution of only 0.25 vpl. This causes the feedback to be degraded and decreases the effectiveness of the controller. For Strategy 1, the scaling was changed so that the tension resolution is 1 vpl (i.e., the controller takes on one value for 99 lbf $\leq t_1(t) <$100 lbf). Although not as accurate as a floating point, this is a substantial improvement.

The control variable is the integer equivalent of the PI Output percentage (the percentage of the maximum output the controller is able to provide). Thus, in order to change the controller output, the tension error must become large enough to vary the PI Output by 0.5 so that the CV changes as opposed to the CV adapting more precisely with the tension error. Moreover, slight corrections in the braking torque are not possible since the adjustment of the braking torque is directly related to the alteration of the CV. Using Equation (3.3), the current PI Output to CV resolution is one CV per percent (cvp). Under the new scaling for Strategy 1, the resolution is 10 cvp. Thus, the control variable is able to achieve 10 different values as the PI Output changes by 1%. The CV is now better suited to attain the value specified by the PI equation. This means that the CV jumps seen in Section 2.5 will be decreased, and thus improved tension control performance is expected.

Since the sampling time was changed, the PI gains need to be re-tuned. Using a model simulation with Strategy 1, the PI gains were tuned until the best performance was achieved. This processes resulted in $K_p = 0.01$ and $K_i = 0.15$. The decrease in the proportional gain indicates that the Unwind Roll is sensitive to large changes

in the input and that the most effective method for controlling the tension is to apply a smooth braking torque. Increasing the proportional action will increase the portion of the controller output that is directly related to the tension error. This will cause abrupt changes in the controller output since the tension error is continuously fluctuating. These actions will produce spikes in tension due to the large adjustments in the braking torque.

A simulation was conducted using the above PI gains. The averaging algorithm as described in Section 2.5 was also employed in this simulation in addition to the aforementioned scalings. Additionally, the constant braking torque that was applied during manual control for the first 10 tension samples was utilized. However, since the sampling time was 0.2 seconds, this torque was only implemented for the initial 2 seconds. Figures 3.15 through 3.18 shows the results of the simulation.

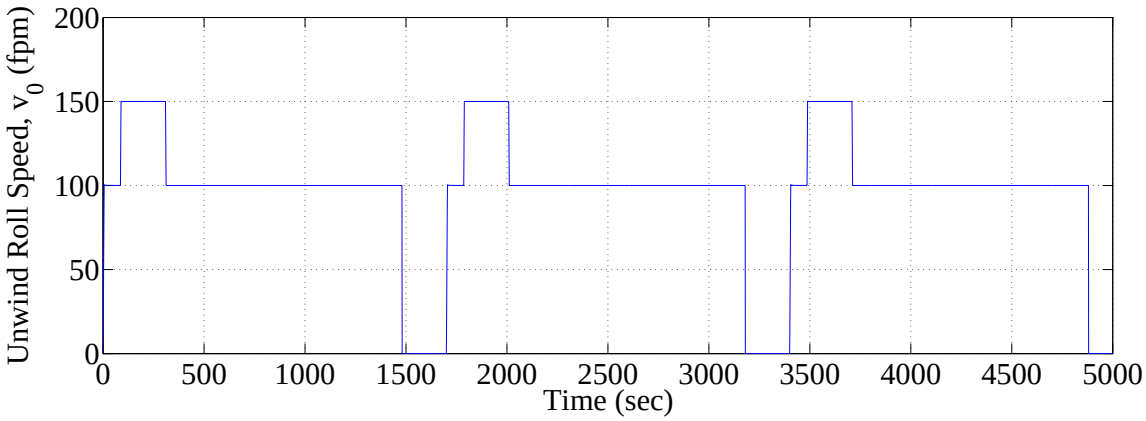

Figure 3.15: Unwind roll velocity using Strategy 1 (Model Simulation)

A comparison of Fig. 3.1 and Fig. 3.15 shows that the velocity followed the reference very well. Moreover, it outperformed the Unwind Roll velocity using the existing strategy as observed by comparing Figs. 3.19 and 3.7. The velocity oscillations near the end of the roll that were present with the current control strategy are reduced with Strategy 1.

As expected, the control variable from Fig. 3.16 has decreased the jumps seen

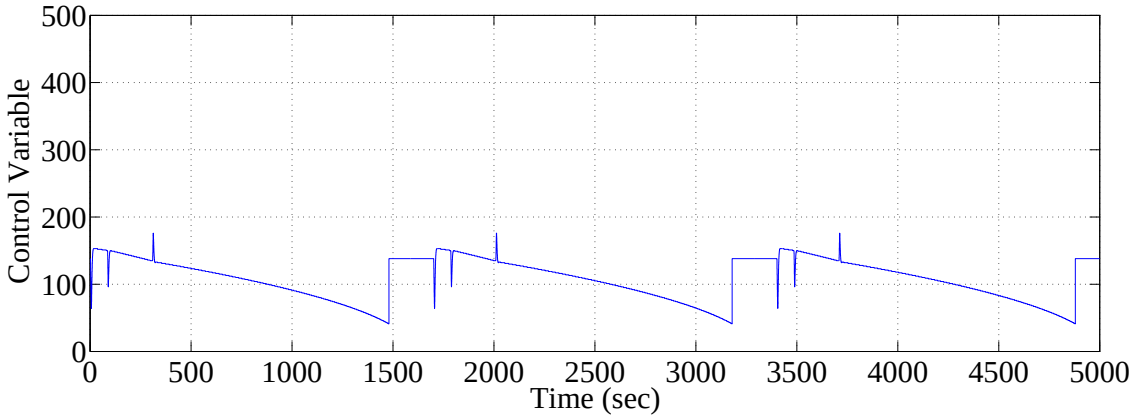

Figure 3.16: Control variable using Strategy 1 (Model Simulation)

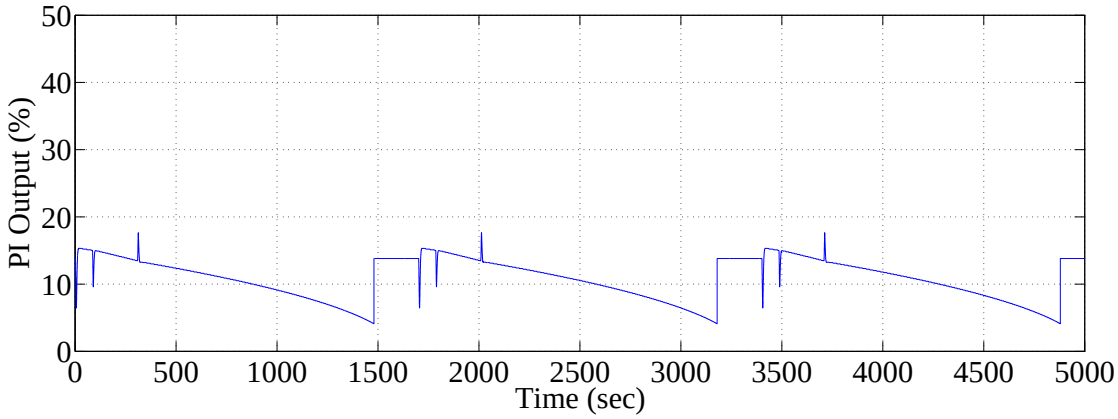

Figure 3.17: PI Output percentage using Strategy 1 (Model Simulation)

with the current control strategy. Additionally, the values are much larger due to the new scaling. Note that this does not change the magnitude of the volts output by the controller; the new scaling allows the CV to assume more values because of its larger range. To further reinforce this statement, note that the PI Output percentage shown in Fig. 3.17 has similar magnitudes as those seen in Fig. 3.4. The value of the PI Output percentage represents the percentage of the maximum braking torque that is applied. Since similar amounts of torque are needed to control the Unwind Roll, it is expected that these values are similar for the current strategy and Strategy 1 even though their respective CV values are different.

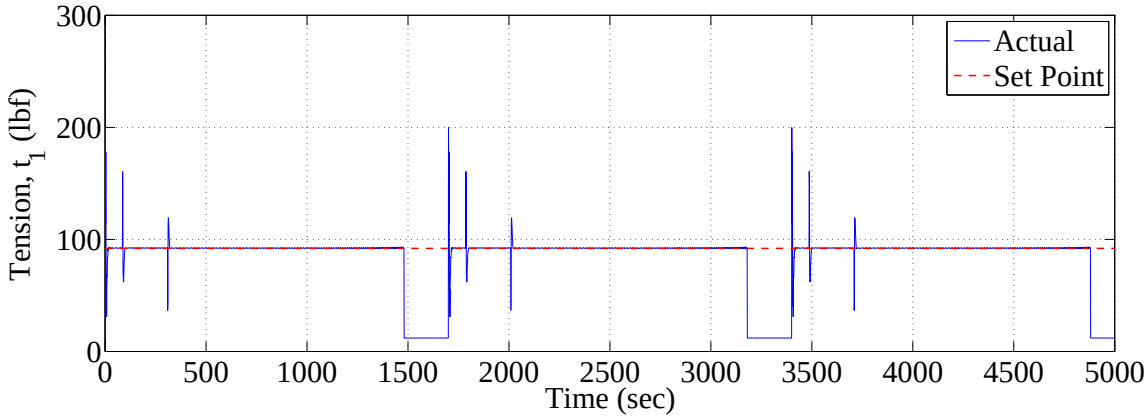

Figure 3.18: Tension using Strategy 1 (Model Simulation)

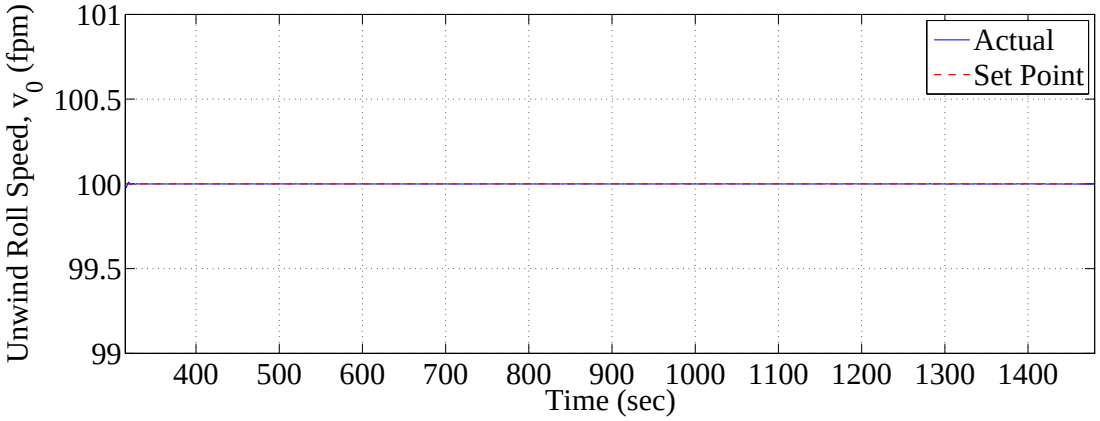

Figure 3.19: Unwind Roll velocity during EF portion of roll using Strategy 1 (Model Simulation)

Comparing the simulated tension using the current control strategy shown in Fig. 3.6 with Fig. 3.18 shows that the tension performance is much improved with Strategy 1. The tension reaches the reference value faster due to the shorter duration of the manual control phase and increase in the integral action. Greater braking torque is applied sooner since the manual control phase is shorter and automatic control can increase the braking torque faster due to the larger integral term, thus increasing the tension quickly to the reference. The increase in steady state tension error seen near the end of the simulation with the current control strategy has also been reduced

with Strategy 1. This is due to the increased integral gain, the faster sampling time, and the higher CV resolution. Near the end of the roll, the control input is more sensitive to the integral portion due to its larger gain which allows the controller to better correct the tension error. Additionally, the brake is using more recent and precise measurements due to the faster sampling time and higher CV resolution which provide more accurate control. These improvements allow the controller to smoothly reduce the braking and thus reduce the tension drift.

Even though the CV jumps have been reduced and the corresponding oscillations in tension have also abated, they are still present near the end of the simulation as seen in Fig. 3.20 which shows a re-scaled tension plot using Strategy 1. Although slight, the increase in oscillation amplitude is due to two factors: (1) the control variable resolution is still not large enough and (2) the PI gains are not appropriate for the smaller roll. Near the end of the roll, the integer changes in the CV, albeit less in magnitude than with the current control strategy, are still significant enough that the corresponding changes in braking torque cause fluctuations in the Unwind Roll velocity, resulting the progressively increasing tension oscillation amplitudes as discussed in Subsection 3.2.2. The control variable is not able to be a floating point value, and thus the controller will not be able to produce the exact output required. Hence, this phenomena will always be present to a certain extent unless floating point values are used. By request of the CFL operators, the CV scaling cannot be increased in order to maintain the simplicity of the interpretation of this variable. A solution that helps reduce the oscillations is to reduce the integral and proportional gains. The effects of this are discussed in Section 3.3.2 when varying PI gains are considered.

One aspect that was not substantially improved with Strategy 1 was the magnitude of the tension spikes that occurred during the speed transitions of the reference velocity profile corresponding to the accumulator filling. The first reason is that the controller with Strategy 1 is still too slow, even though the tension sampling time was

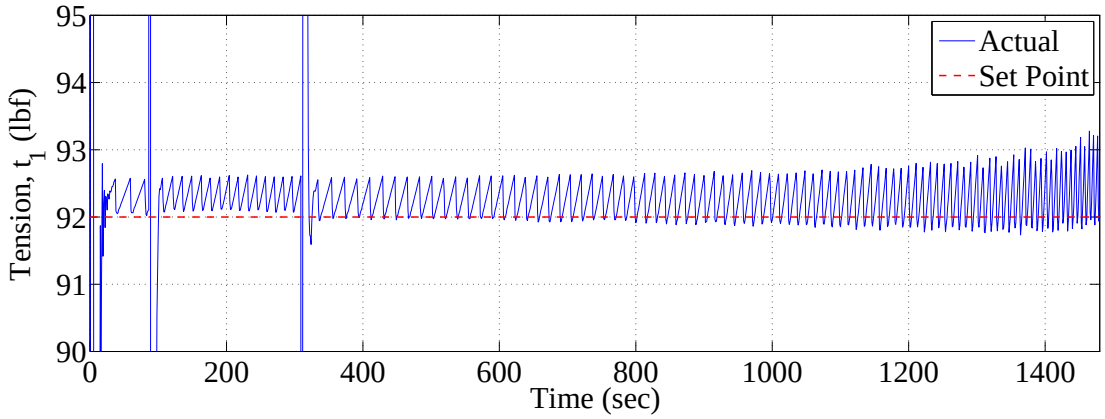

Figure 3.20: Tension oscillation amplitudes still increase as the material roll depletes using Strategy 1 (Model Simulation)

decreased. However, the pneumatic device restricts the efficacy of further decreasing the controller update time; the device dynamics limit its reactivity to the changes dictated by the faster controller. When Pull Roll 1 velocity increases (as in segments OA and BC from Fig. 3.1), the tension in Span 1 also increases and thus the brake torque decreases. However, the brake torque does not decrease fast enough, causing the large spike. Shortly thereafter, the velocity of Pull Roll 1 becomes constant. With the reduced braking torque, the inertia of the Unwind Roll causes it to overshoot the speed of Pull Roll 1, creating a large dip in tension. A couple possibilities for solving this problem exist. If the controller and actuator were fast enough, they would be able to quickly compensate for these actions, resulting in increased performance. Another option would be to change the PI gains. However, the solutions for the large spike and the dip counteract one another; while increased gains would allow the brake to decrease faster, this would result in a larger dip. The converse trends are true when Pull Roll 1 decreases back to line speed in segment DE from Fig. 3.1.

3.3.2 Strategy 2

As discussed above, there are two concerns in the tension regulation for this scenario: (1) tension spikes during speed transitions and (2) oscillations with increasing amplitude that are shown in Fig. 3.20. The spikes are so large because the controller is unable to either increase or decrease the brake pressure fast enough. To alleviate this problem, K_p and K_i should be increased. As soon as the tension is too large or small, the increased gains will change the CV by a greater amount, causing the brake to react quicker. The spike in tension at approximately 310 seconds when Pull Roll 1 decreases from filling speed back to line speed is actually lower with smaller gains. At the initial deceleration, the tension drops, resulting in an increase in controller output. The larger gains will output a greater amount of torque than the smaller gains. When Pull Roll 1 stops decelerating and operates at a constant value, the greater braking torque will produce a larger tension spike whereas the smaller gains will have a smaller increase in torque, resulting in a decreased tension spike magnitude. However, the smaller gains result in a lower initial tension drop as they are slower to respond to the decrease in tension.

As mentioned previously, the tension is very sensitive to large changes in the braking torque. This phenomena is amplified when the radius of the Unwind Roll is smaller since the brake has more affect on its velocity. To smoothen the control near the end of the roll and reduce the oscillations, the PI gains should both be decreased. The decrease in gains will reduce the fluctuations in braking torque which will smooth the control action, resulting in improved tension performance.

These results indicate that the PI gains should decrease over time. Initially, larger gains are desirable to reduce the spikes in tension during reference velocity changes. However, smaller gains are required as the roll depletes to keep the system stable and reduce the large oscillations. Thus, for Strategy 2 the PI gains are chosen to be functions of the Unwind Roll radius given in Equations (3.4a) and (3.4b) below.

This idea of varying the gains was borrowed from Reference [1] which used gains in an Linear Quadratic (LQ) optimal velocity controller that were functions of the inertia and radius of the Unwind Roll. As the roll depleted, the gains also decreased. Although this is a torque controlled Unwind Roll, a similar philosophy is used.

$$K_p(t) = m_p R_0(t) + b_p \tag{3.4a}$$

$$K_i(t) = m_i R_0(t) + b_i \tag{3.4b}$$

where m_p (m_i) and b_p (b_i) are the slope and intercept for proportional (integral) gain. The slopes are defined in the following.

$$m_p = \frac{K_{p,\max} - K_{p,\min}}{R_{0,\max} - R_{0,\min}} \tag{3.5a}$$

$$m_i = \frac{K_{i,\max} - K_{i,\min}}{R_{0,\max} - R_{0,\min}} \tag{3.5b}$$

where the "max" and "min" correspond to the maximum and minimum values for the respective variable. The intercepts are defined in Equations (3.6a) and (3.6b).

$$b_p = K_p^\star - m_p R_0^\star \tag{3.6a}$$

$$b_i = K_i^\star - m_i R_0^\star \tag{3.6b}$$

where $K_p^\star$ and $K_i^\star$ are the constant PI gains that allow Strategy 1 to adequately control the system (i.e., $K_p^\star = 0.01$ and $K_i^\star = 0.15$) and $R_0^\star$ is the value of the Unwind Roll radius where $K_p^\star$ and $K_i^\star$ produce the best tension performance. This is assumed to occur when the roll is half full, so $R_0^\star$ is selected to be half way between $R_{0,\max}$ and $R_{0,\min}$. The maximum and minimum gains are chosen to be a certain percentage above and below, respectively, the corresponding starred value as indicated in Equations

(3.7a) through (3.7d).

$$K_{p,\max} = (1 + K_{p0})\, K_p^\star \tag{3.7a}$$

$$K_{p,\min} = (1 - K_{p0})\, K_p^\star \tag{3.7b}$$

$$K_{i,\max} = (1 + K_{i0})\, K_i^\star \tag{3.7c}$$

$$K_{i,\min} = (1 - K_{i0})\, K_i^\star \tag{3.7d}$$

Figure 3.21 displays a graphical representation of the proportional gain using the

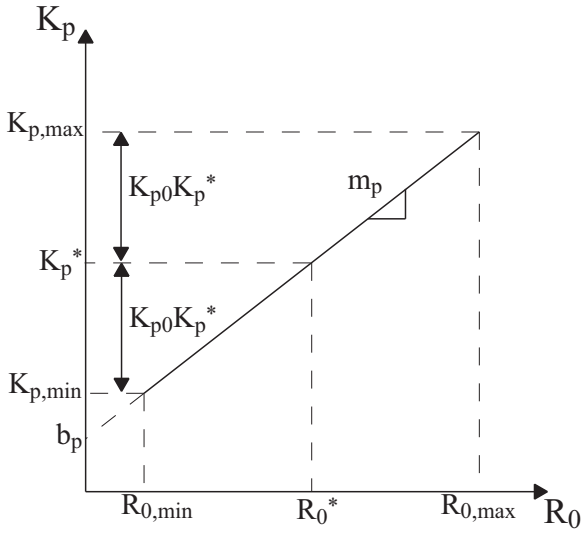

Figure 3.21: Proportional gain as a function of Unwind Roll radius

above method. Calculating the gains in this fashion ensures that they cannot greatly deviate from values which have been shown to provide adequate control. This provides an element of safety while also allowing the gains to change. Note that the stability of the closed loop system was not shown using varying gains; however, the Unwind Roll radius is slowly changing so the system with the varying gains is assumed to be stable. The model simulation that follows and the experimental results that are discussed later both show the system remaining stable while using this gain calculation algorithm, so long as the gains are properly tuned.

Tuning resulted in $K_p^\star = 0.01$ and $K_i^\star = 0.15$ with $K_{p0} = K_{i0} = 0.45$. A model

simulation was conducted using Strategy 2 with the time-varying gains as well as the scalings discussed in Section 3.3.1. The results are given in Figs. 3.22 through 3.27.

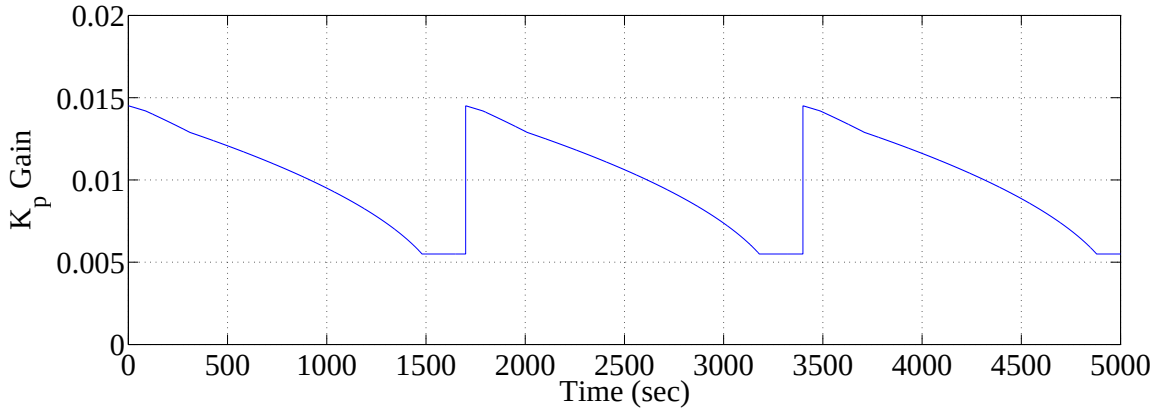

Figure 3.22: Proportional gain using Strategy 2 (Model Simulation)

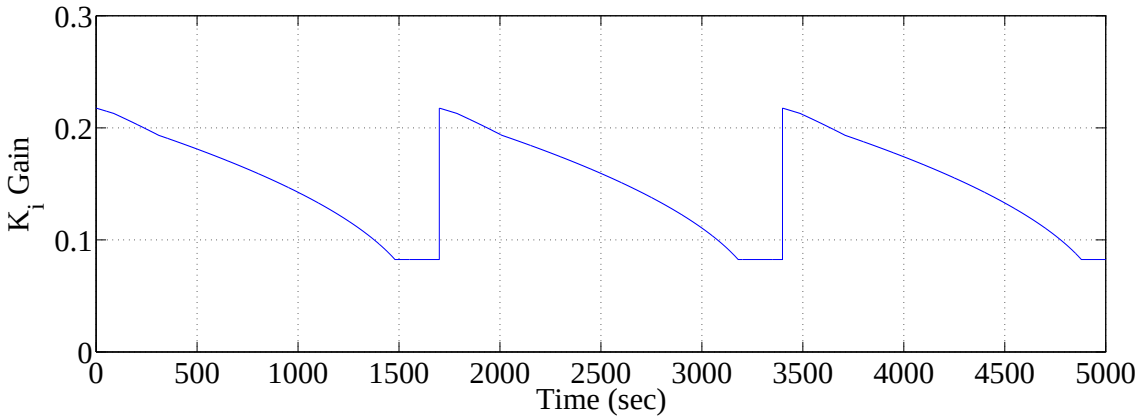

Figure 3.23: Integral gain using Strategy 2 (Model Simulation)

Figures 3.22 and 3.23 show the proportional and integral gains, respectively. Note that K_p starts at 0.0145 and decreases to 0.0055 at the roll depletion. Likewise, K_i has values of 0.2175 and 0.0825 at the system initiation and roll depletion, respectively. These results indicate that the gain calculation functioned as desired.

A comparison of Figs. 3.4 and 3.26 shows that Strategy 2 uses similar PI Output magnitudes as those used in the current strategy. Strategy 2 initially increases the output earlier than the current strategy due to the increased integral gain and the

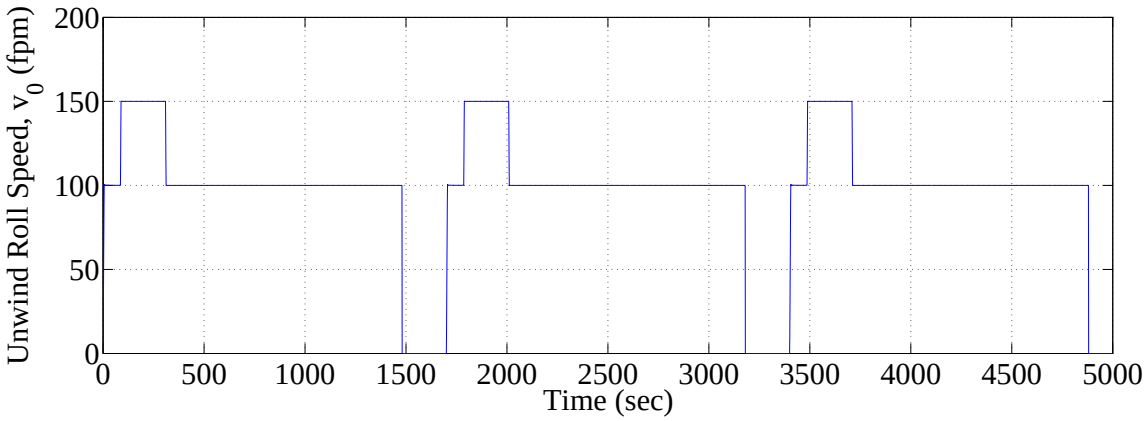

Figure 3.24: Unwind roll velocity using Strategy 2 (Model Simulation)

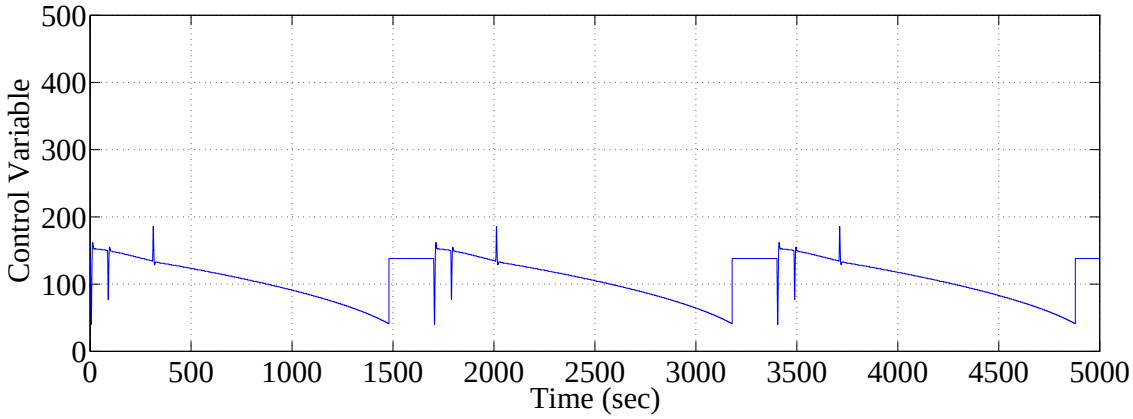

Figure 3.25: Control variable using Strategy 2 (Model Simulation)

shorter duration of the manual control. This allows the tension using Strategy 2 to reach the reference value before that achieved using the current control strategy. Moreover, Strategy 2 provides a much smoother CV profile without the large jumps between integer values. As will be seen later, this will result in improved tension results since the brake is able to apply a more precise amount of torque as determined by the PI controller. Note that the CV values of Strategy 2 are similar to those of Strategy 1 since they use the same scaling.

A comparison of Figs. 3.6 and 3.27 illustrates that the tension performance is much improved using Strategy 2. The general trends discussed in the previous section,

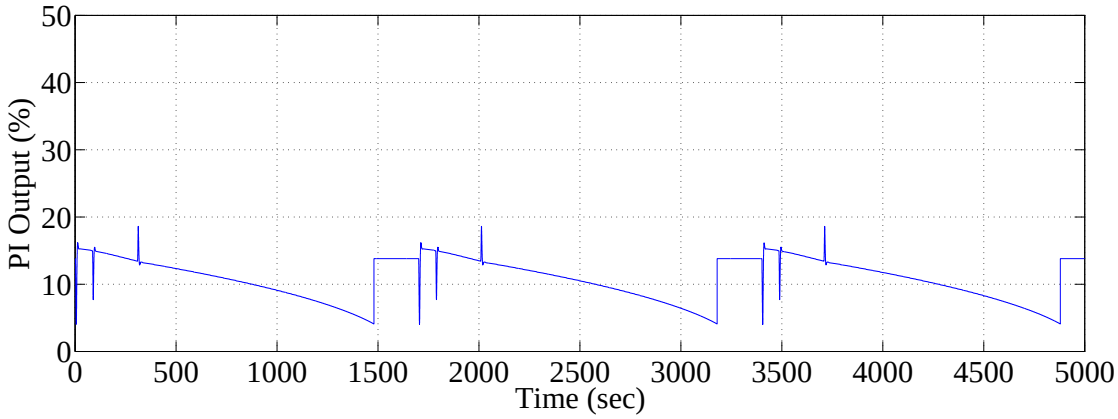

Figure 3.26: PI Output percentage using Strategy 2 (Model Simulation)

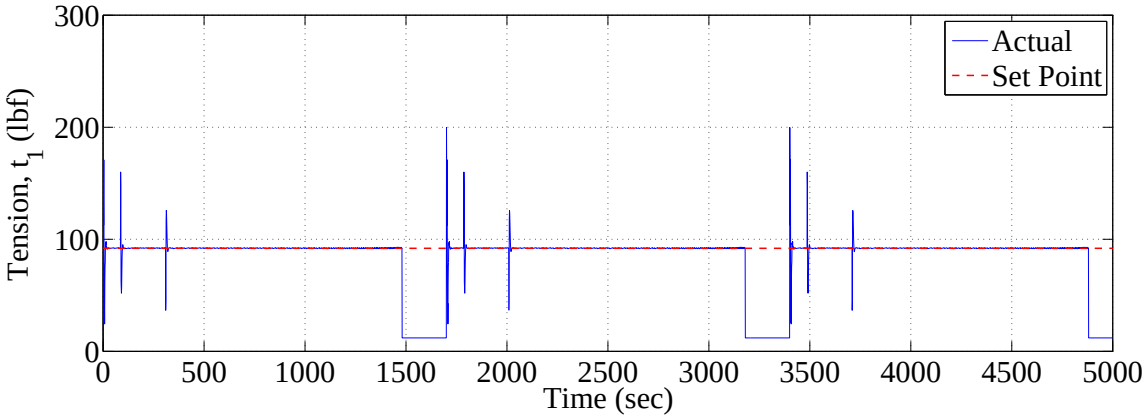

Figure 3.27: Tension using Strategy 2 (Model Simulation)

including the faster rise of the tension to the reference value, the tension spikes during Pull Roll 1 speed changes and the oscillations near roll depletion (see Fig. 3.28), are also present with Strategy 2. However, the new strategy was able to rise to the reference tension value faster. Additionally, near the roll depletion, both the amplitudes of the oscillations as well as the amount of steady state error were reduced. Therefore, Strategy 2 is an improvement over the existing strategy.

In order for Strategy 2 to function, the Unwind Roll radius must be measured. Currently on the CFL, the Unwind Roll radius is not measured. However, the total length of web in each roll is measured as well as the length of material removed from

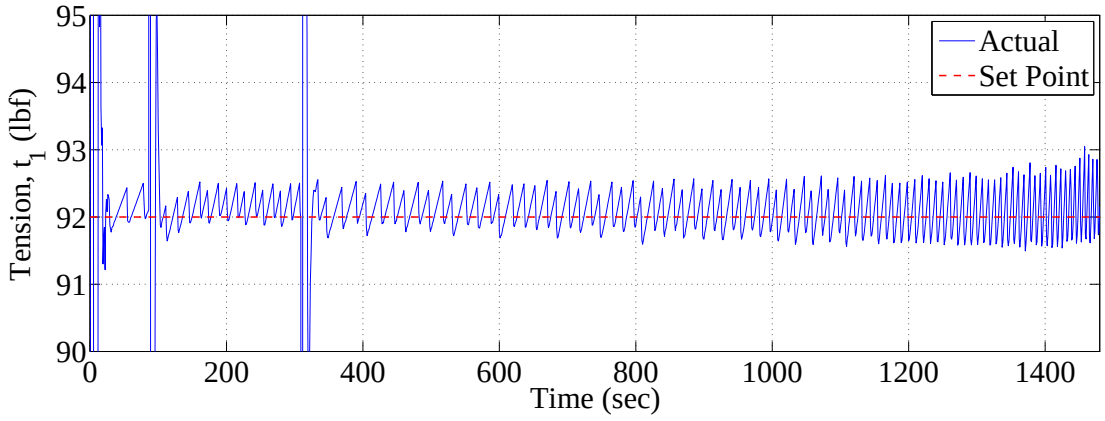

Figure 3.28: Re-scaled Span 1 tension using Strategy 2 (Model Simulation)

the Unwind Roll. Thus the radius can be calculated from the following algorithm. The same concept that was utilized when deriving Equation (3.1) can be used here except now the web length is time varying. $L_w(t)$ represents the length of material on the Unwind Roll and is the difference between the initial length of the web in a roll, $L_{w,i}$, and the amount removed from the roll, $\Delta L_w(t)$. Therefore, Equation (3.1) can be rewritten as the following.

$$R_0(t) = \sqrt{\frac{(L_{w,i} - \Delta L_w(t))t_w}{\pi} + R_{c0}^2} \tag{3.8}$$

3.3.3 Strategy 3

In Strategies 1 and 2, the integrator carried much of the "controller load" as it provided the equilibrium torque and also provided correction. The aim of Strategy 3 is to use feed-forward action to eliminate this load on the integrator and allow the integrator to be solely used to make corrections.

The control input is thus broken into two portions as given in Equation (3.9) below.

$$u_0(t) = u_{0f}(t) + u_{0c}(t) \tag{3.9}$$

where $u_{0f}(t)$ and $u_{0c}(t)$ are, respectively, the feed-forward and correction portions of

$u_0(t)$. The objective for $u_{0f}(t)$ is to apply the equilibrium torque and allow corrections to be made by $u_{0c}(t)$. Assuming the last three terms in Equation (2.1) are small, the equilibrium torque is $t_r R_0(t)$. Thus, accounting for the conversion from controller output to torque input, $u_{0f}(t)$ is given in Equation (3.10).

$$u_{0f}(t) = \frac{t_r R_0(t)}{n_0} \tag{3.10}$$

As previously discussed, sudden changes in the control torque can cause large variations in tension. This is especially prevalent during the initialization of a new Unwind Roll since the Unwind Roll must be moved from rest and Pull Roll 1 is accelerating. The tension spike caused by any sudden braking torque applied to the Unwind Roll will be magnified since the velocity of the downstream roller is increasing. Thus, using the feed-forward control from the initialization of the Unwind Roll would cause large tension fluctuations. To avoid this, the feed-forward control will be ramped according to the following.

$$u_{0f}(t) = \begin{cases} (0.1 + 0.09t)\,\dfrac{t_r R_0(t)}{n0} & \text{if } t \leq 10 \text{ sec} \\ \frac{t_r R_0(t)}{n0} & \text{else} \end{cases} \tag{3.11}$$

where n_0 accounts for the unit conversion from the PI Output to applied torque. In this way, the initial feed-forward torque applied to the Unwind Roll will be $0.1 t_r R_0(0)$ and then after 10 seconds, $t_r R_0(t)$. This gradual increase will steadily increase the tension. Note that after two seconds, the PI control will also help regulate the tension.

The correction portion of $u_0(t)$ will be provided by a PI controller using tension feedback. Using the same reasoning discussed in Section 3.3.2, the PI gains will be functions of the radius and also defined as in Equations (3.4a) and (3.4b). Additionally, the tension averaging algorithm will be employed and therefore the implementation of PI control will be delayed for 2 seconds in order to acquire the initial 10 tension measurements to use in feedback. The scalings used in Strategy 1 are also

utilized. Thus the correction portion of the control is defined as shown below.

$$u_{0c}(t) = K_p(t)e_t(t) + K_i(t)\int_0^t e_t(\tau)d\tau \tag{3.12}$$

where $e_t(t)$ is the scaled tension error. The control torque $u_0(t)$ can now be defined as in Equation (3.13).

$$u_0(t) = \begin{cases} \dfrac{(0.1+0.09t)\,t_r R_0(t)}{n_0} & \text{if } t < 2 \text{ sec} \\ \dfrac{(0.1+0.09t)\,t_r R_0(t)}{n_0} + K_p(t)e_t(t) + K_i(t)\int_0^t e_t(\tau)d\tau & \text{if } 2 \le t < 10 \text{ sec} \\ \dfrac{t_r R_0(t)}{n_0} + K_p(t)e_t(t) + K_i(t)\int_0^t e_t(\tau)d\tau & \text{if } t \ge 10 \text{ sec} \end{cases} \tag{3.13}$$

Tuning resulted in $K_p^\star = 0.01$ and $K_i^\star = 0.15$ with $K_{p0} = K_{i0} = 0.5$.

A model simulation was conducted using the above gains with Equation (3.13) as the control input and the scalings discussed in Section 3.3.1. The controller output was limited similarly to the current control strategy as discussed in Section 2.5. It was reasoned that the $u_0(t)$ produced by Equation (3.13) should result in magnitudes comparable to the CV of Strategies 1 and 2. Thus, so long as the equivalent PI Output is maintained at values between 1% and 80%, the actuator would not saturate. This assures that Strategy 3 can be integrated to the current system without the need for additional hardware. The results of the simulation are shown in Figs. 3.29 through 3.32.

Figures 3.29 and 3.30 show the equivalent PI Output percentage and the controller output for the feed-forward and correction portions, as well as the total controller output. Since the PI Output percentage achieves magnitudes similar to the current control strategy and did not exceed any of its limits, this strategy is physically realizable. Additionally, the total controller output was comparable to the values seen with Strategies 1 and 2. As desired, the feed-forward is seen to constitute the majority of the total controller output with the correction portion making slight adjustments. The feed-forward increases for the initial ten seconds whereafter it continually de-

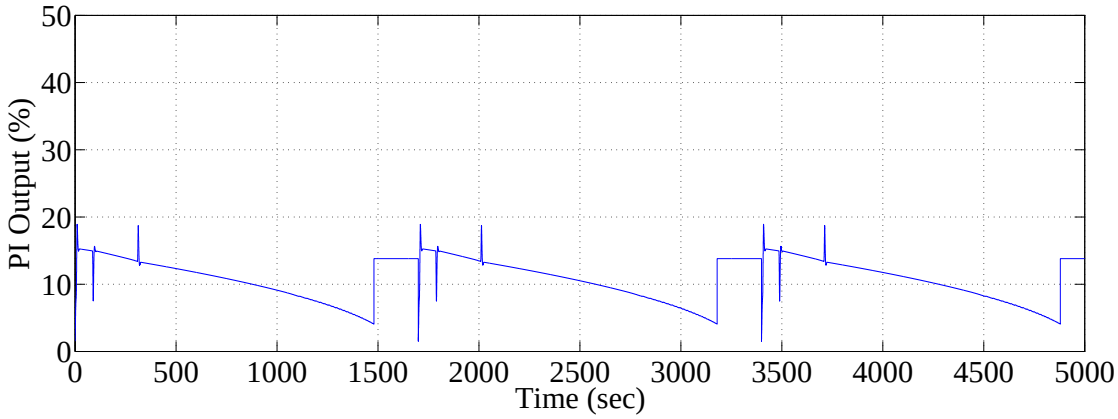

Figure 3.29: PI Output percentage using Strategy 3 (Model Simulation)

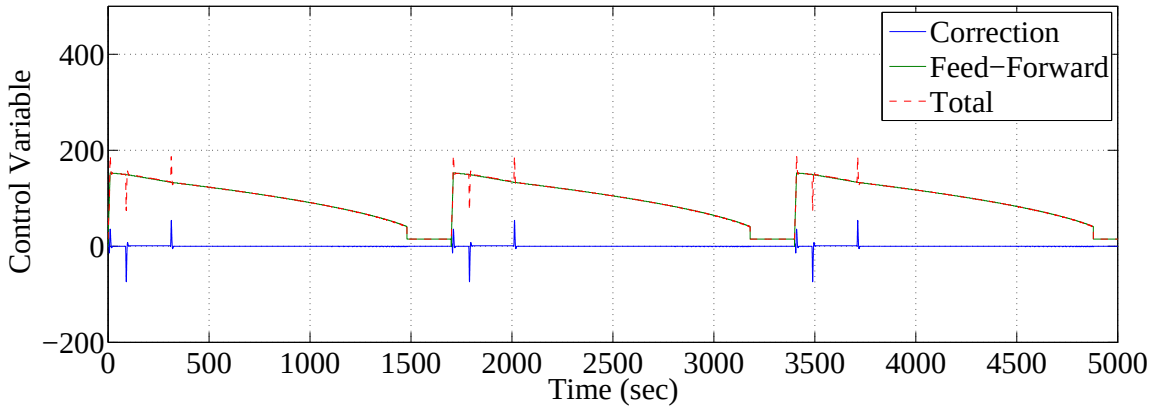

Figure 3.30: Controller output using Strategy 3 (Model Simulation)

creases due to the decrease in radius.

Figure 3.31 shows the tension results for Strategy 3. The performance is similar to Strategies 1 and 2; the tension regulation is sufficient when the Unwind Roll velocity is constant. However, except for the initial acceleration, there are large tension fluctuations during speed changes. Additionally, Strategy 3 was unable to completely eliminate the oscillations near the depletion of the Unwind Roll (see Fig. 3.33). In fact, these oscillations are larger than those produced using Strategies 1 and 2. The ramping of the feed-forward torque performed as desired and allowed for a relatively smooth increase in tension from the initial value of 12 lbf, with only a 20

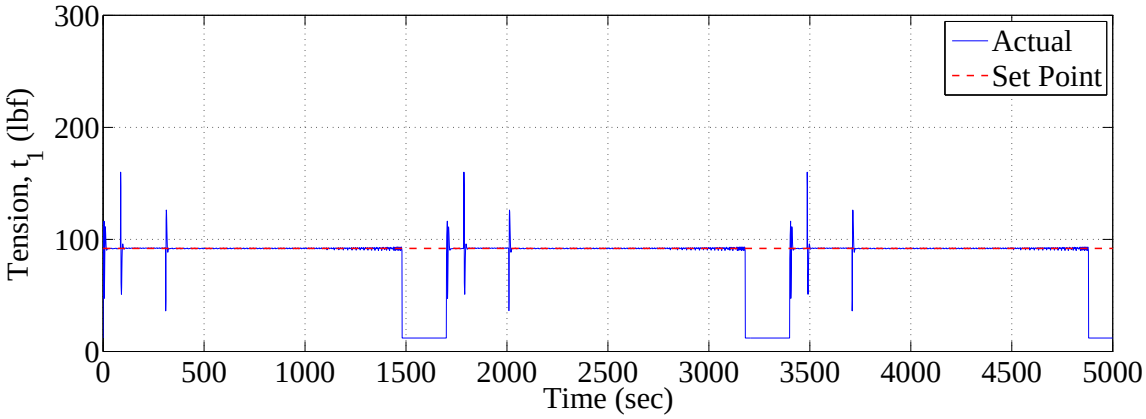

Figure 3.31: Tension using Strategy 3 (Model Simulation)

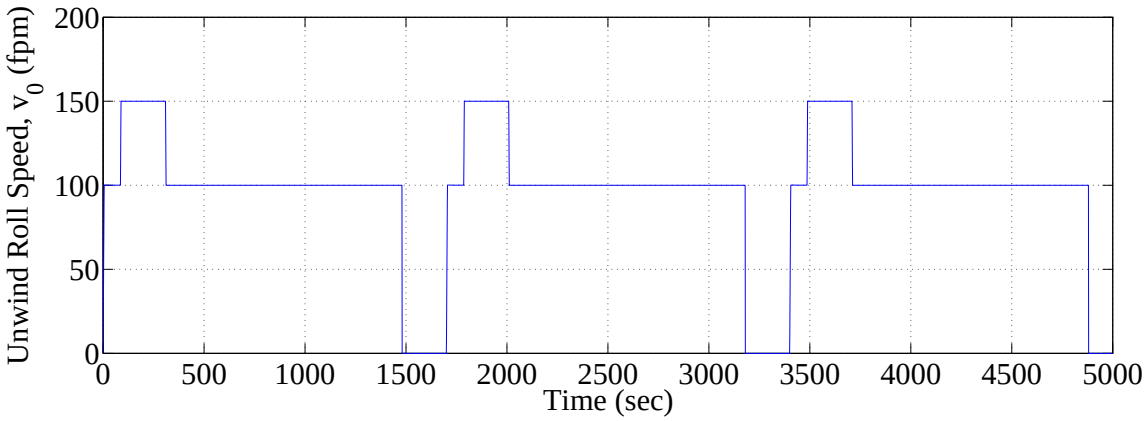

Figure 3.32: Unwind roll velocity using Strategy 3 (Model Simulation)

lbf overshoot (as compared to 110 lbf for the other strategies).

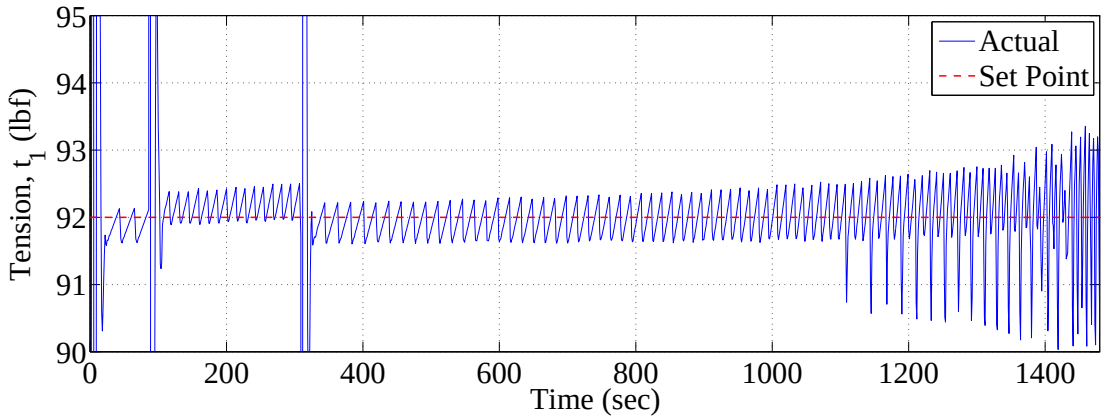

Figure 3.33: Re-scaled Span 1 tension using Strategy 3 (Model Simulation)

3.3.4 Summary

Comparing the results of Strategies 1 through 3 to those of Section 3.2.2 illustrates that the proposed strategies each improve tension regulation performance over the current strategy. Even though each of the new strategies had a larger spike during the Pull Roll 1 velocity reference Phase DE from Fig. 3.1, all other aspects were greatly improved. More specifically, Strategy 3 reduced the large tension spike present at the beginning of the simulation in Strategies 1 and 2. With each of the new strategies, the tension was able to reach the reference value during the constant velocity phases, which was not attained in the current control strategy. Moreover, near the end of the simulation, the oscillations were reduced as was the steady state tension error. For these reasons, Strategies 1 through 3 are superior to the current control strategy.

The simulations in Subsections 3.3.1 through 3.3.3 showed very similar tension results. Each attained large tension values at every speed change of Pull Roll 1 (except for the initial spike with Strategy 3 which was significantly lower than the other two strategies), remained near the reference value during constant reference velocity phases, and had oscillations near the end of the roll. The performance of Strategies 1 and 2 were nearly identical although Strategy 2 did reduce the amount of steady state error. Strategy 3 was not able to reduce the tension oscillation amplitudes to the values achieved using Strategies 1 and 2 but it did reduce the large initial tension spike using the gradual increase in feed-forward control.

Employment of these three strategies on the CFL is the subsequent task in the testing/development of these strategies. Successful implementation will further support the effectiveness of the proposed improvements. This topic is discussed in the subsequent section.

3.4 Experimental Data Analysis

This section describes the implementation of the three previously outlined strategies onto the CFL. Each section begins with several runs of data from the current strategy before the employment of the new strategy. For clarity, only a representative sample of results will be presented. Each experiment was conducted with the same web material on the CFL during production. It is noted that these experiments were not conducted for the specific purpose of obtaining data for this thesis; the experiments were conducted on the CFL during the manufacture of actual product. Therefore, extreme caution was required in the development and implementation of the RSLogix code so that the web was not ruptured and the machinery was not damaged.

There are two separate brakes (labeled "Brake 1" and "Brake 2") that are controlled by the PID. These brakes are pneumatically operated and can have different configurations (as they most often are) resulting in dissimilar tension performances and dissimilar controller outputs for a given PID controller. Therefore, each of the the following analyses are divided into two portions where the strategy under consideration is compared with the current strategy using Brake 1 and then using Brake 2.

3.4.1 Strategy 1 Experimental Results

The first experiment was conducted on the CFL using Strategy 1. On-site tuning suggested that the appropriate PI gains were 0.01 and 0.05 for K_p and K_i, respectively. The values suggested by the simulations discussed in Section 3.3.1 were initially selected but were later changed as they resulted in rapid changes in the control variable which was unacceptable since a conservative approach was taken in implementing these experiments as they were conducted during the production of actual material. The proportional and integral gains of 0.01 and 0.05, respectively, were chosen since they provided a similar rate of change in the control variable that was observed us-

ing the existing strategy. The integral gain is different from the value selected for the model in Section 3.3.1 because the model was not an exact representation of the physical system. The model assumed the dynamics relating the braking pressure to the applied braking torque was a constant gain. As mentioned in Section 3.2.2, the actual dynamics may involve a stick-slip relationship that relates the force applied to the Unwind Roll by the braking pressure to the corresponding friction torque. Additionally, the model assumed an average tension model. Therefore, it did not account for the dynamics introduced by the idle rollers present in the actual CFL and it also did not include the tension propagation effects from the other sections of the CFL.

Strategy 1 was allowed to control the Unwind Roll for approximately 6 hours whereafter the gains were tuned in an attempt to increase performance. However, insufficient data was collected during this tuning process. Thus, the following analysis is based on the results of only those gains that are specified initially.

It is noted that, approximately three hours into the experiment, the initial roll radius was decreased from 16 inches to 14 inches. In order to keep the comparisons as similar as possible, only the data corresponding to 16 inch initial roll radius will be considered. Additionally, the line reference speed during the data collection for the current control strategy was 10 fpm slower than that for Strategy 1. However, the shape of the velocity profiles for Pull Roll 1 were nearly identical for both strategies.

Analysis Using Brake 1

Figures 3.34 through 3.39 show the experimental data for both the current control strategy and Strategy 1 using Brake 1. The three main changes that are observed in the experimental data that made Strategy 1 distinct from the current control strategy were:

1. Automatic control was activated in 2 seconds (as opposed to 10)

2. The PID gains were increased due to the change in sampling time

3. The controller output resolution was increased, making the brake more sensitive to changes in tension.

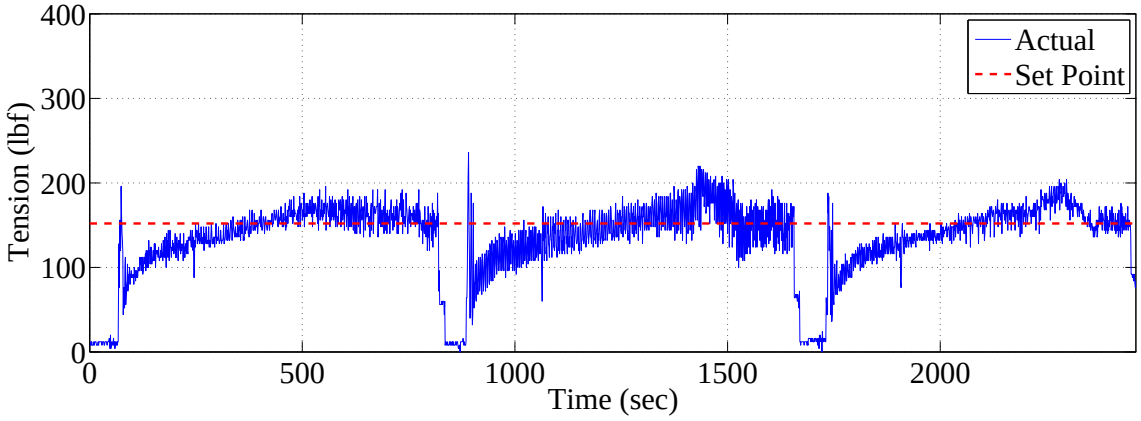

Figure 3.34: Tension using the current control strategy with Brake 1 prior to implementation of Strategy 1

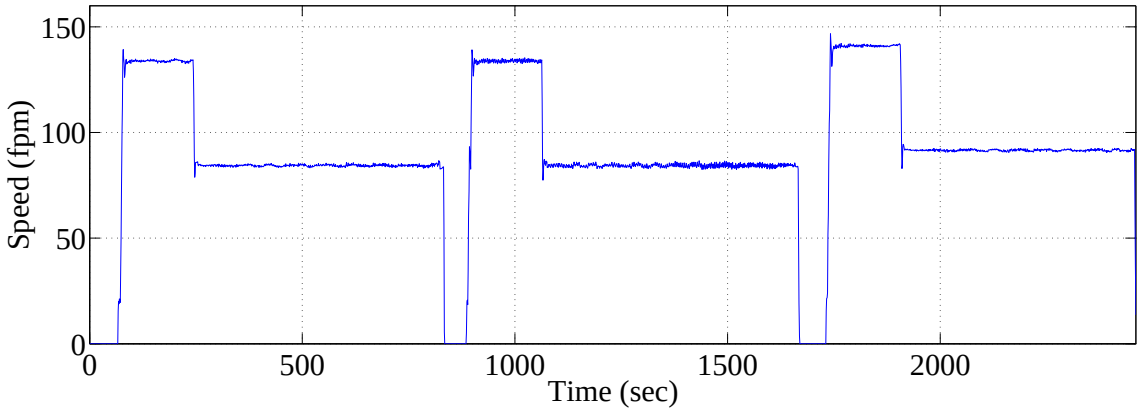

Figure 3.35: Pull Roll 1 velocity using the current control strategy with Brake 1 prior to implementation of Strategy 1

The effects of (1) and (2) can be seen in Fig. 3.40. Prior to automatic control, the two controllers will output identical, constant values. However, due to (1), Strategy 1 begins to increase the output before the current strategy to bring the tension to the reference value. Additionally, this rise is very fast relative to the current control

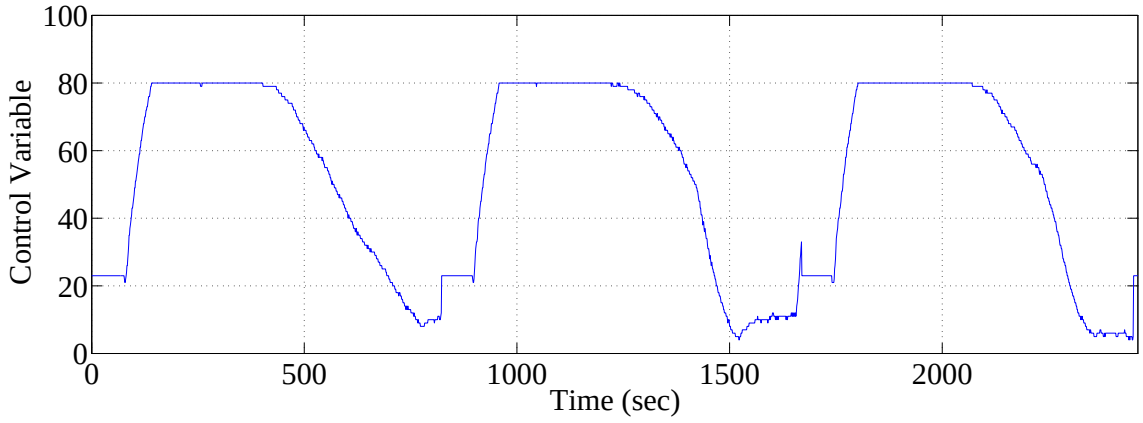

Figure 3.36: Control variable using the current control strategy with Brake 1 prior to implementation of Strategy 1

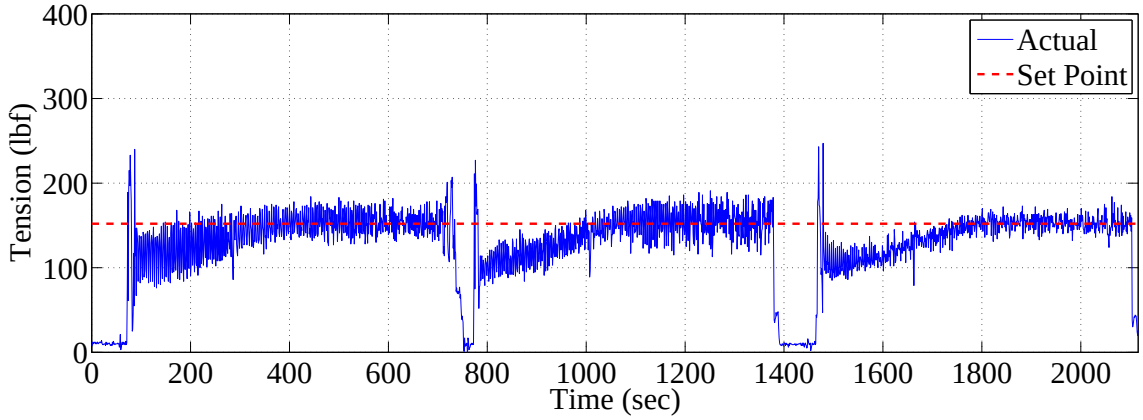

Figure 3.37: Tension using Strategy 1 with Brake 1

strategy due to the larger gains used in Strategy 1. These two trends in Strategy 1 cause the tension to reach the reference value faster than the current control strategy.

Another trend seen in the data is that once the tension for Strategy 1 reached the reference value, it oscillated about this value. However, the current strategy typically overshot the reference value. Overshoot in this section refers to the general trend of the tension over a substantial portion of time increasing over the reference value, not the oscillation of the data over a short period. This trend is due to (2) and (3). Since the tension sampling time was decreased for Strategy 1, the tension signal can

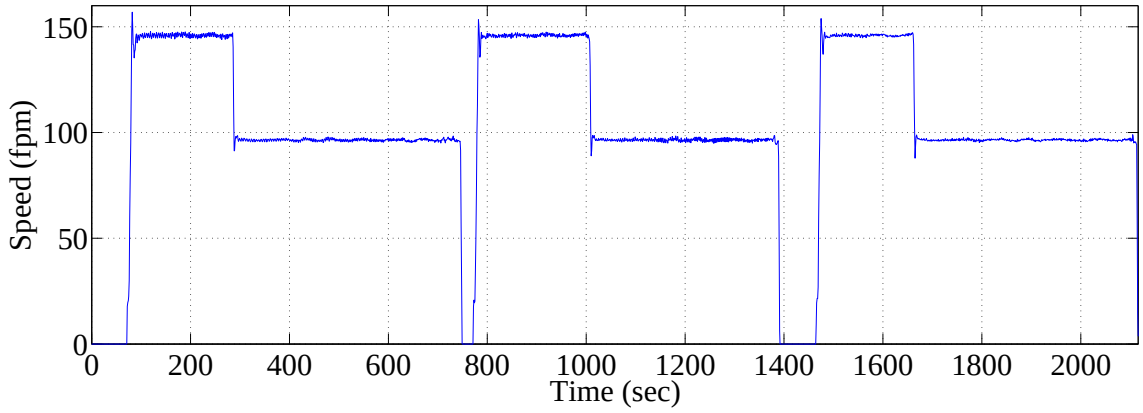

Figure 3.38: Pull Roll 1 velocity using Strategy 1 with Brake 1

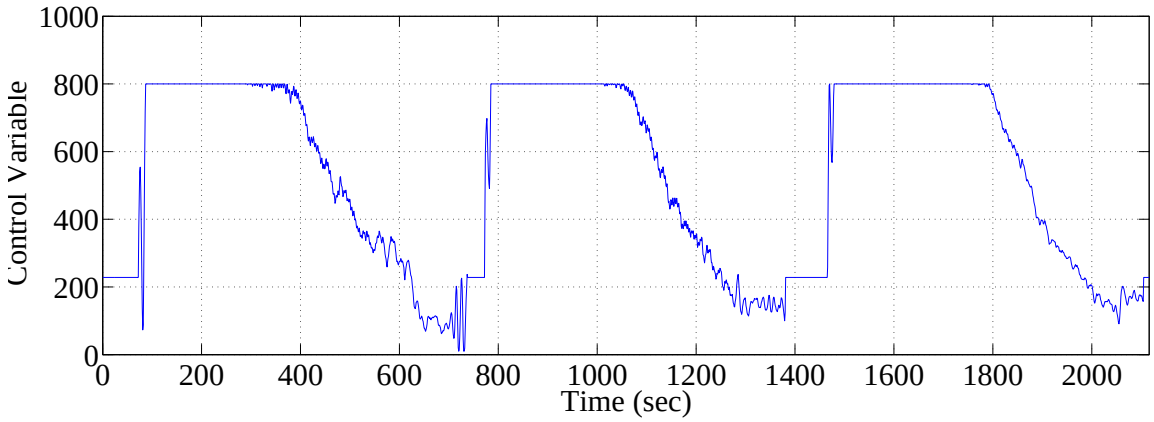

Figure 3.39: Control variable using Strategy 1 with Brake 1

be more accurately recreated, thus allowing the controller to react properly to the actual tension. Additionally, the increased PID gains allow the controller to correct for smaller tension errors. These corrections are more precise to the value created by the PID since the control variable has more resolution. This is shown in Fig. 3.40 as the control variable for Strategy 1 makes more corrections as the roll progresses whereas the current strategy is relatively stagnant. Thus, as the tension deviated from the reference value, Strategy 1 made the proper corrections to keep the tension near the reference value.

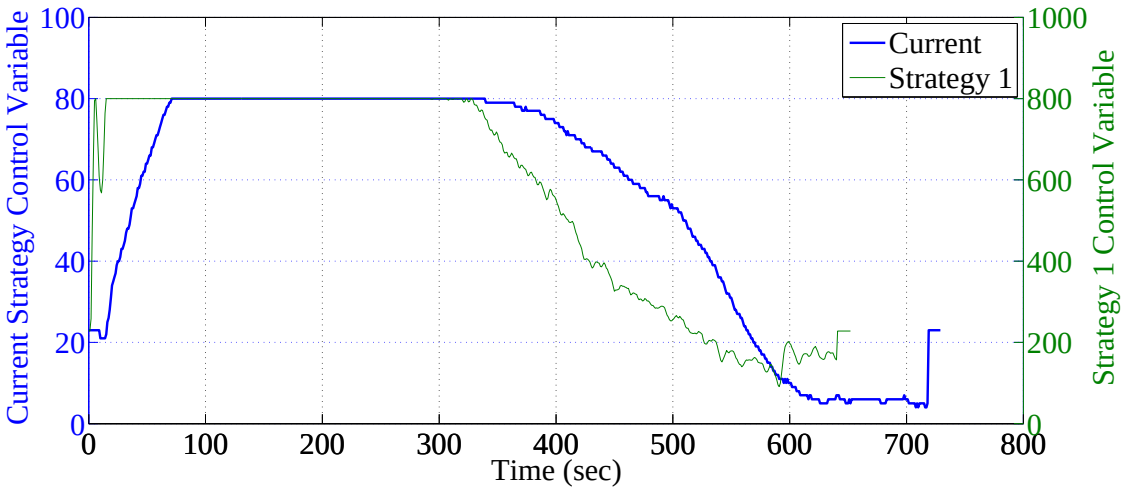

Figure 3.40: Control variable for a typical roll using Strategy 1 and the current control strategy with Brake 1

However, Strategy 1 was unable to appreciably reduce the size of oscillations. In fact, near the end of several rolls, the oscillations began to increase. This could be attributed to the PID gains which, while appropriate for larger rolls, were too large for the smaller Unwind Roll radii. Additionally, the response time of the brake could be negatively affecting the performance of the controller. Strategy 1 occasionally changed the controller output relatively quickly. If the brake is unable to properly react to these changes, the higher precision of Strategy 1 will have limited utility.

Analysis Using Brake 2

Figures 3.41 through 3.46 show the experimental data for both the current control strategy and Strategy 1 using Brake 2. Although not as prevalent as the tension data for Brake 1, the current strategy did produce some overshoot via Brake 2. Moreover, using Brake 2, the current strategy maintained the tension near the reference value better than was possible with Brake 1. The tension oscillation amplitudes using Brake 2 also increased near the end of the roll whereas for Brake 1, no such increase occurred. These results clearly illustrate that, as mentioned earlier, the two brakes

produce different results even while being controlled by the same control algorithm.

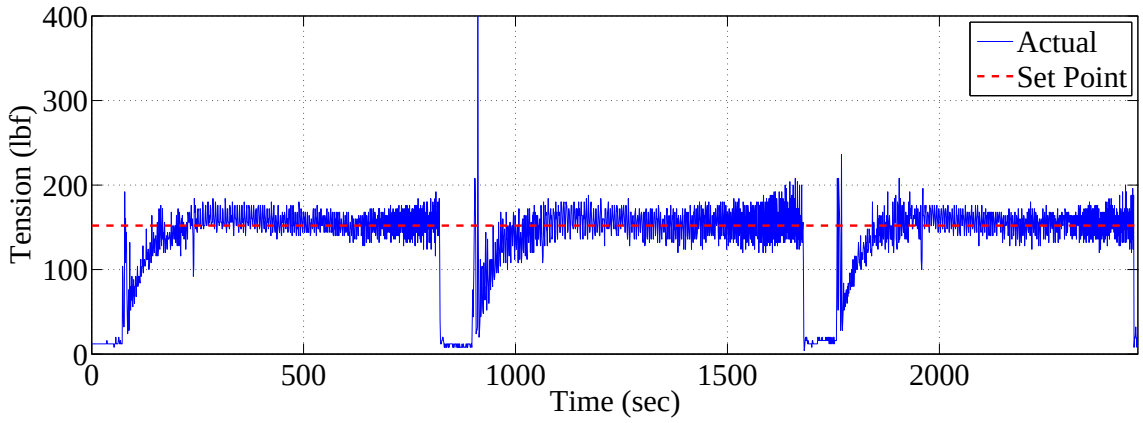

Figure 3.41: Tension using the current control strategy with Brake 2 prior to implementation of Strategy 1

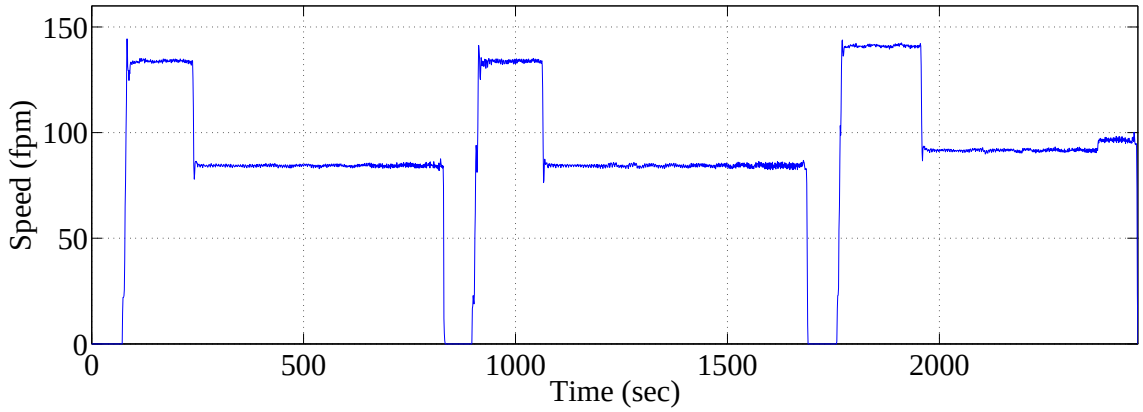

Figure 3.42: Pull Roll 1 velocity using the current control strategy with Brake 2 prior to implementation of Strategy 1

Unlike the results obtained using Brake 1, the current strategy was actually slightly faster than Strategy 1 at driving the tension to the reference value. However, during this time, Strategy 1 maintained the tension closer to the reference value. This means that during the initial tension increase Strategy 1 produced tension values that, while not at the reference value, were closer to the reference value than the current strategy.

Similar to the results obtained using Brake 1, Strategy 1 reduced the overshoot

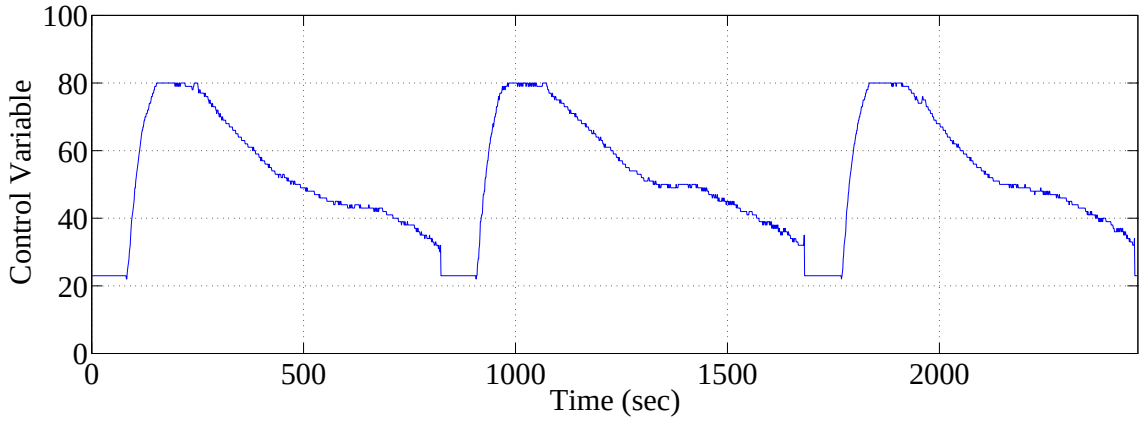

Figure 3.43: Control variable using the current control strategy with Brake 2 prior to implementation of Strategy 1

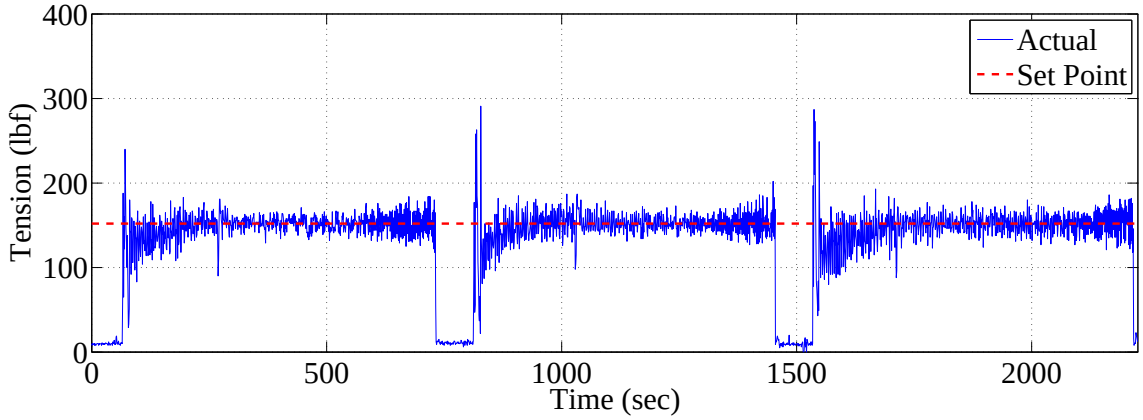

Figure 3.44: Tension using Strategy 1 with Brake 2

trend seen in the current strategy. As mentioned previously, this is due to Strategy 1 being able to adapt the output with greater precision than the current strategy because of the larger gains and increased CV resolution used by Strategy 1. Strategy 1 was also able to sufficiently decrease the amplitude of the tension oscillations although the oscillations near the end of the roll were not eliminated. This is in contrast to the results obtained using Brake 1 where Strategy 1 actually produced slightly larger oscillations, especially near the end of the rolls.

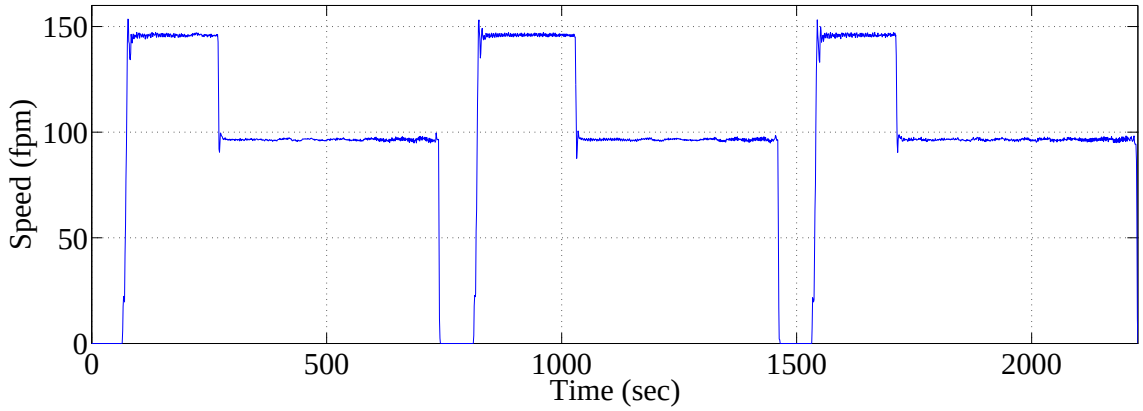

Figure 3.45: Pull Roll 1 velocity using Strategy 1 with Brake 2

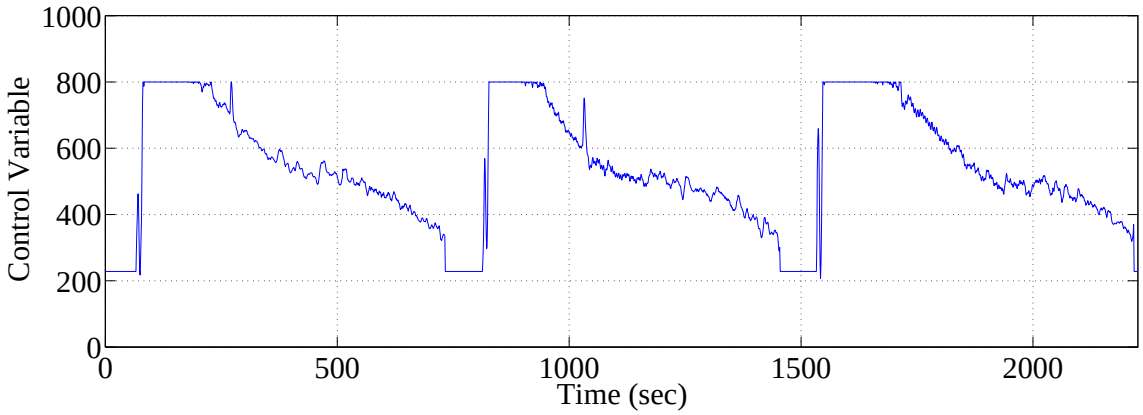

Figure 3.46: Control variable using Strategy 1 with Brake 2

Summary

This experiment illustrated that Strategy 1 was successful in improving the tension performance. For both brakes, Strategy 1 reduced the overshoot and successfully maintained the tension near the reference value, except near the end of the rolls. In fact, in the case of Brake 2, the tension oscillation amplitudes decreased. The rise time was also reduced for Brake 1 using Strategy 1 while for Brake 2, there was not a significant change in this value. The only shortcoming of Strategy 1 is the increase in oscillation amplitudes present near the end of rolls. These could be reduced by decreasing the PID gains; however, since the gains are fixed, this would reduce the

performance for other portions of the roll. This indicates a need to have the larger PI gains initially and then decrease them as the roll depletes. The subsequent topic is to implement Strategy 2.

3.4.2 Strategy 2 Experimental Results

This subsection discusses the results of implementing Strategy 2 onto the CFL. As described in Subsection 3.3, sudden changes in braking torque induce large tension oscillations when the material roll is nearly depleted. Thus, it is desirable to have a smooth control signal during this phase. In order to achieve this, the PI gains should be decreased at the end of the roll. This is the rationale for Strategy 2, which uses the faster sampling time and higher resolutions employed in Strategy 1 along with gains that vary according to Equations (3.4a) and (3.4b). For the experiments conducted for Strategy 2, $K_p^\star = 0.01$, $K_i^\star = 0.05$, and $K_{p0} = K_{i0} = 0.3$ which indicates that both gains will initially be 30% larger than the gains specified in Strategy 1 and then decrease to values that are 30% lower. As was the case with Brake 1, these gains were selected conservatively in that they were not allowed to vary by 45% as was suggested by the model using Strategy 2. The radius calculation from Equation (3.8) was also created in the CFL RSLogix routine in order to calculate the controller gains. It is noted that through the process of experimentation discussed in Subsection 3.4.1, the tension resolution on the CFL was permanently changed to one vpl from the previous value of 0.25 vpl. Similar to Subsection 3.4.1, this analysis is divided into two portions with one for each brake.

Analysis for Brake 1

Figures 3.47 through 3.49 show the data collected using the current control strategy with Brake 1 prior to the experiment and Figs. 3.50 through 3.52 display the data while Strategy 2 was used for control. Note that only one set of data is displayed

for Strategy 2 because using this strategy with Brake 2 resulted in poor performance due to a change in its brake configuration. Comparing Figs. 3.38, 3.48, and 3.51 shows that the Pull Roll 1 speed profiles for these data sets are similar, although the speeds do not match. However, the differences are small, so this data is suitable for comparison.

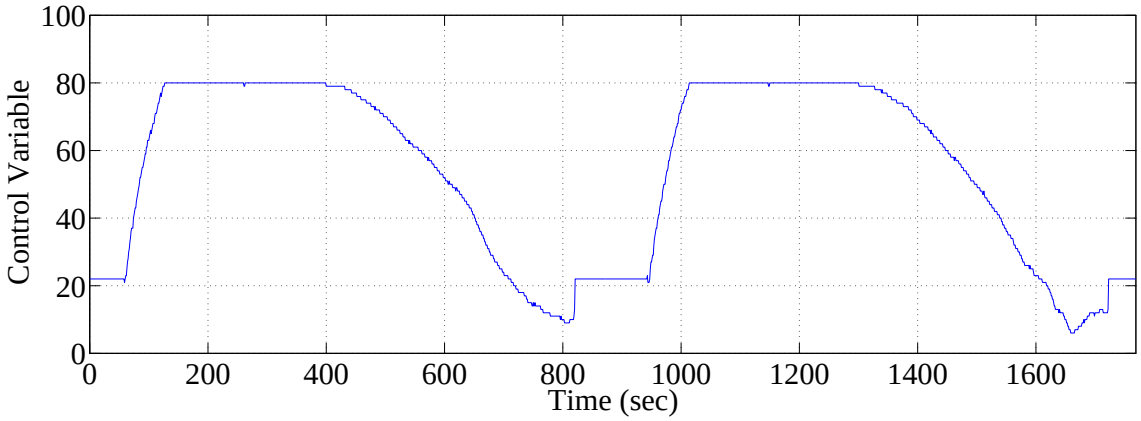

Figure 3.47: Control variable for the current control strategy using Brake 1 prior to implementation of Strategy 2

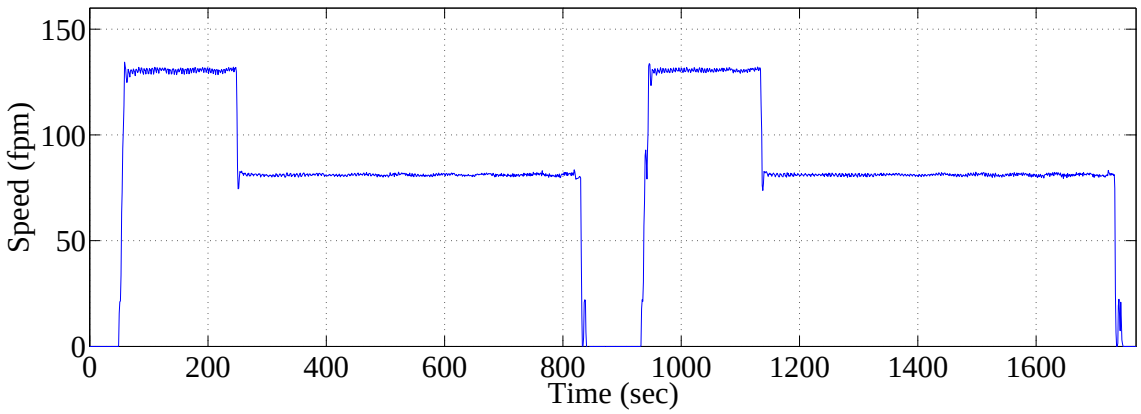

Figure 3.48: Pull Roll 1 speed for the current control strategy using Brake 1 prior to implementation of Strategy 2

Similar to the results obtained using Strategy 1, the control variable for Strategy 2 provided corrections that were more precise to the tension error than those seen

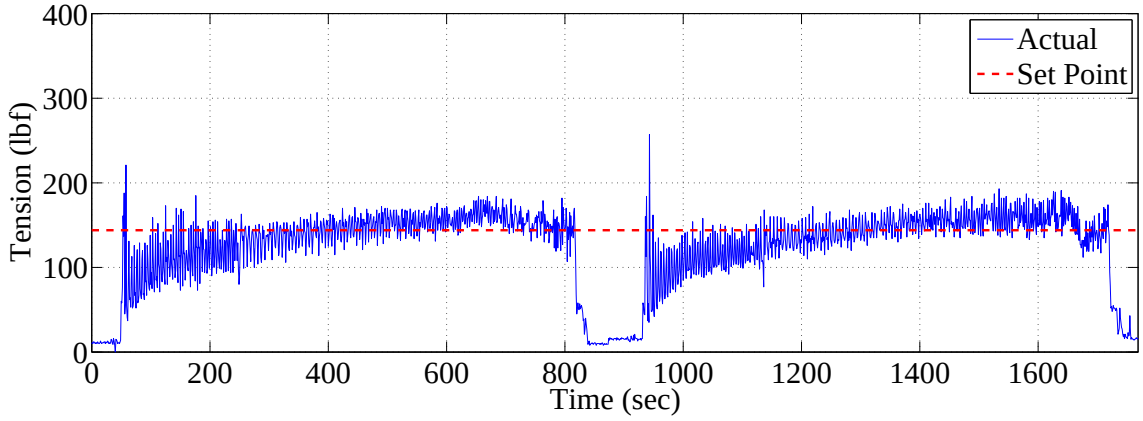

Figure 3.49: Tension for current control strategy using Brake 1 prior to implementation of Strategy 2

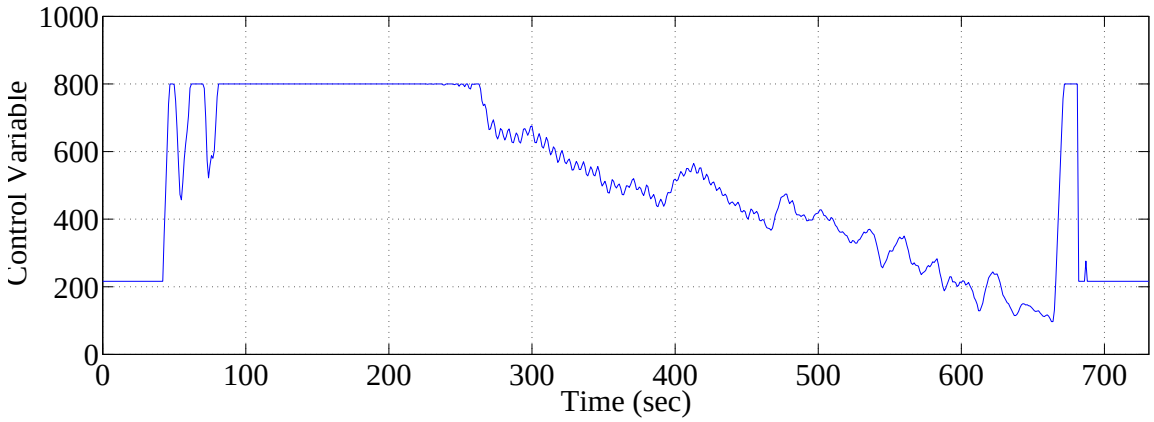

Figure 3.50: Control variable for Strategy 2 using Brake 1

with the current control strategy. This trend is due to the decreased sampling time utilized in Strategy 2. Near the end of the roll, the control variable for Strategy 2 does not fluctuate less rapidly than Strategy 1. As the discussion in Section 3.3 explains, this will result in approximately the same amplitudes of tension oscillation that were present near the roll depletion for Strategy 1. However, a comparison of Figs. 3.47 and 3.50 reveals that the current control strategy provides a smoother control variable profile than Strategy 2. Thus, despite having decreased gains, the tension oscillations at the end of the roll for Strategy 2 will still be greater than those

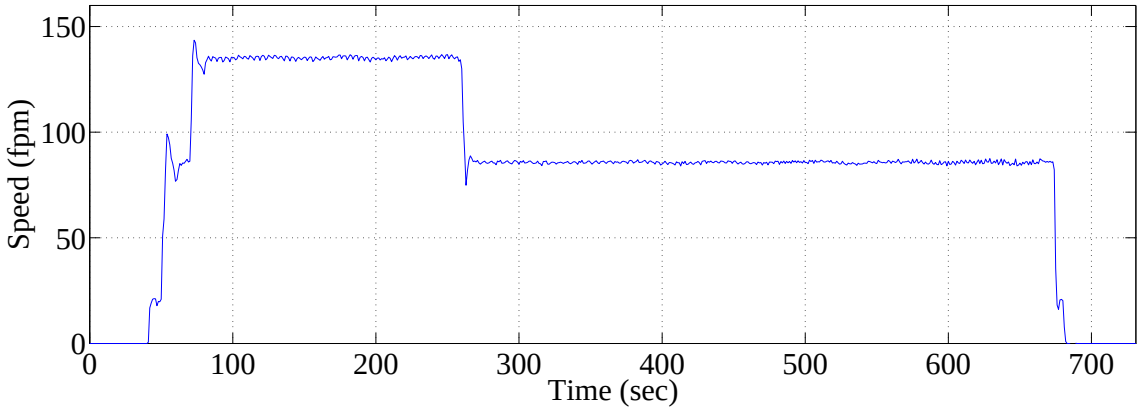

Figure 3.51: Pull Roll 1 Speed for Strategy 2 using Brake 1

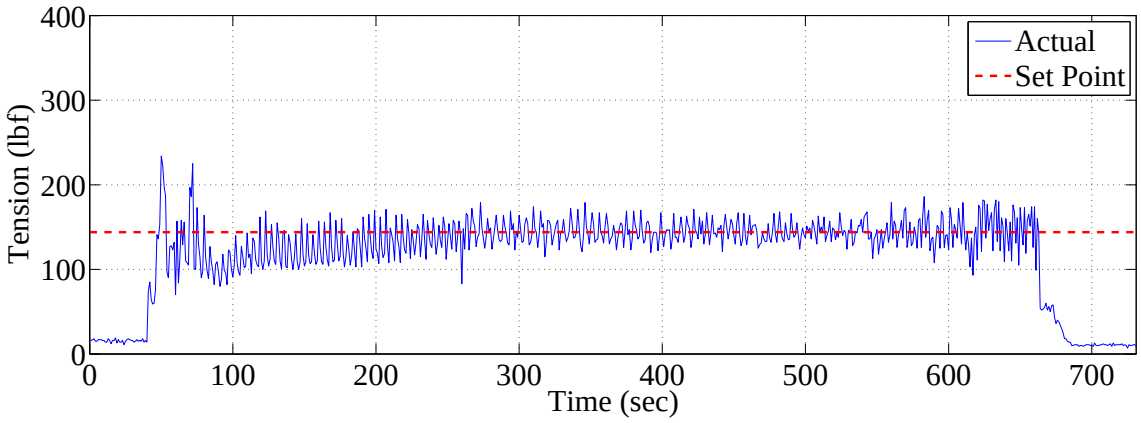

Figure 3.52: Tension for Strategy 2 using Brake 1

in the current control strategy.

A comparison of Fig. 3.37 and Fig. 3.52 confirms the results mentioned above, in that the tension oscillations that were present near the end of the roll for Strategy 1 have not been appreciably changed using Strategy 2. This is explained by the control variable which is still changing too rapidly and inducing tension oscillations as discussed in Section 3.3. The gains could be decreased further by increasing K_{p0} and K_{i0}; however, as will be seen later, this is not a practical option due to the variability in the brake configurations. Fig. 3.49 verifies that the current control strategy has the smallest tension oscillation amplitudes just prior to roll depletion,

although Strategies 1 and 2 provide improved control for the beginning and middle portions of the material roll.

Analysis for Brake 2

Figures 3.53 through 3.55 show the data collected while using the current control strategy with Brake 2. Comparing Figs. 3.43 and 3.53 and considering the fact that the only difference in these two control strategies is the tension feedback resolution, illustrates the variability in the brakes used in the unwind section of the CFL. From Subsection 2.5.2, it is known that the physical configuration of the brakes can be altered and this effectively changes the gains. This is demonstrated by the equivalent tension performances that result when the same control strategy is used to produce two different control variables. The new brake configuration during the Strategy 2 experiment effectively increased the gains from the Strategy 1 experiment since, for the former case, a smaller control variable resulted in the same amount of braking torque that was produced with the previous brake configuration which utilized larger control variable values. The PID gains used in the current strategy are low enough that this reconfiguration does not detrimentally alter the performance of the brake. On the other hand, this also suggests that it will be difficult to provide improvements that will be universally effective for both brakes and for any brake configuration. This problem is discussed further in Subsection 3.4.5.

Figures 3.56 through 3.58, which show the data collected using Strategy 2 with Brake 2, shows that this reconfiguration altered the performance of the controller. The gain changing-like affect of adjusting the brake configuration is illustrated in these results because the gains used for Strategy 2 differed from those used in Strategy 1 by no more than 30%. Yet the system became unstable at the end of the roll using Strategy 2 since the new configuration has essentially increased the gains so that they are no longer appropriate. The K_p and K_i values would cause the control

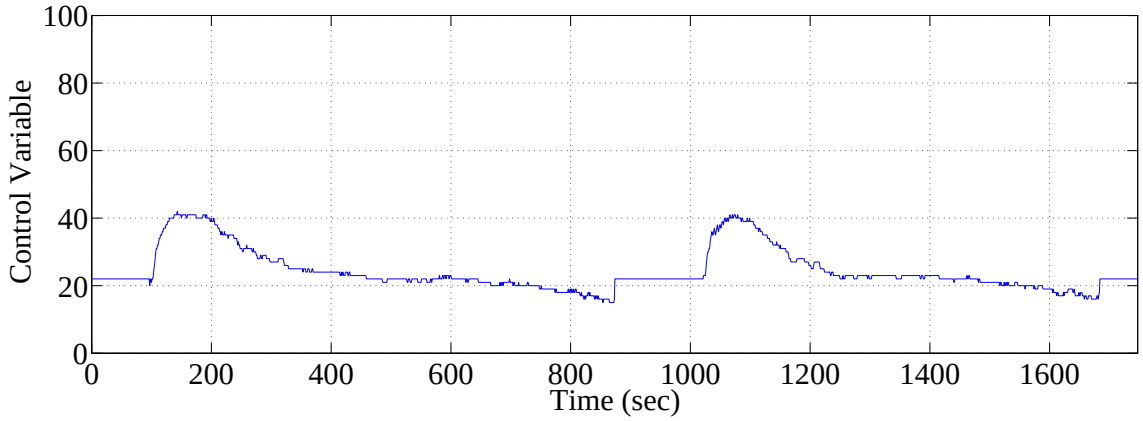

Figure 3.53: Control variable for current control strategy using Brake 2 prior to implementation of Strategy 2

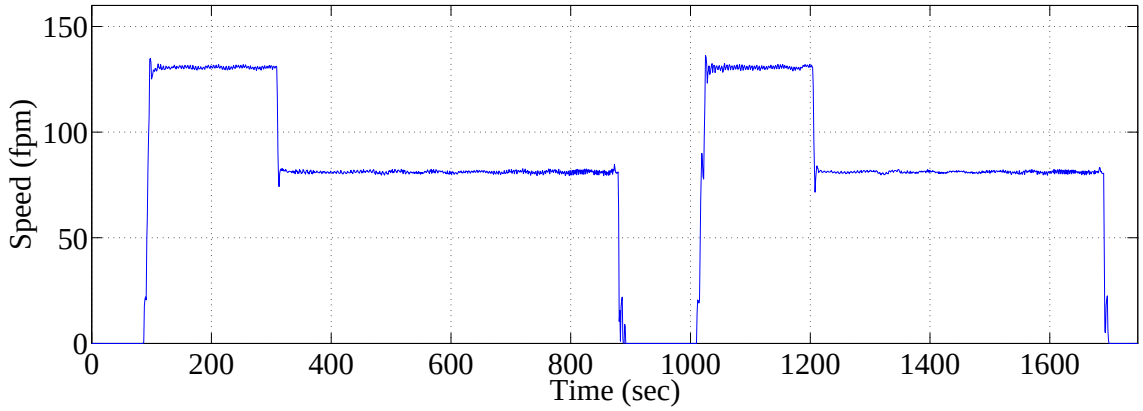

Figure 3.54: Pull Roll 1 Speed for current control strategy using Brake 2 prior to implementation of Strategy 2

variable to change by a certain amount based on the tension error. Under the new configuration for Brake 2, this alteration in the control variable results in a larger change in braking torque than the corresponding change for Brake 1. Near the end of the roll, when changes in the control variable have a much greater affect on the tension, these fluctuations in the braking torque caused the system to become unstable.

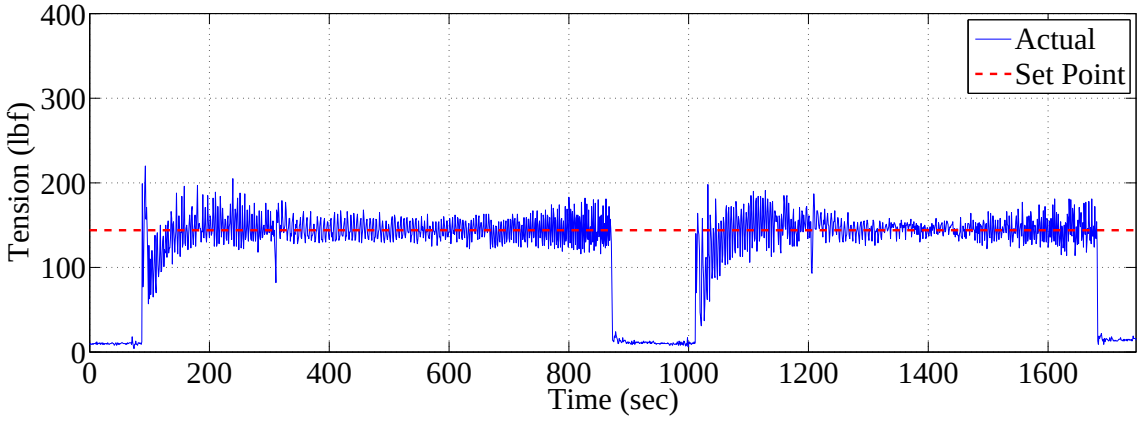

Figure 3.55: Tension for current control strategy using Brake 2 prior to implementation of Strategy 2

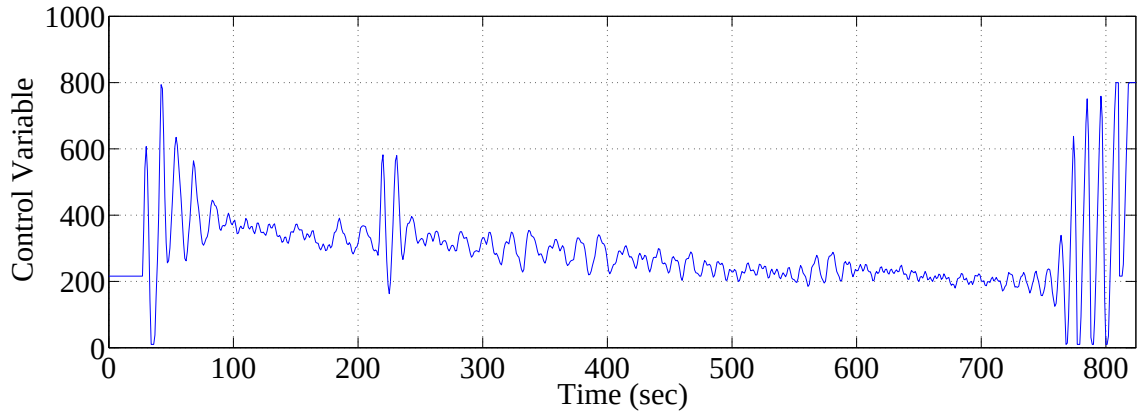

Figure 3.56: Control variable for Strategy 2 using Brake 2

Summary

Strategy 2 was unable to substantially alter the oscillations present at the end of the material roll. For Brake 1, the tension regulation at the beginning and middle of the roll was sufficient. However, due to the alteration of the Brake 2 configuration, Strategy 2 had degraded results, especially at the end of the roll where the system became unstable. This illustrates that adjusting the brakes effectively changes the controller gains.

As seen from the data presented in this subsection, the configuration of the brake

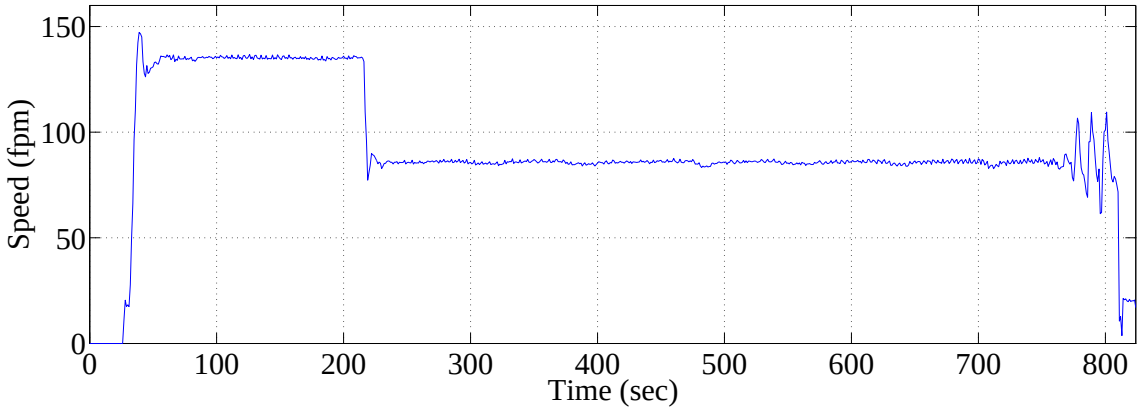

Figure 3.57: Pull Roll 1 speed for Strategy 2 using Brake 2

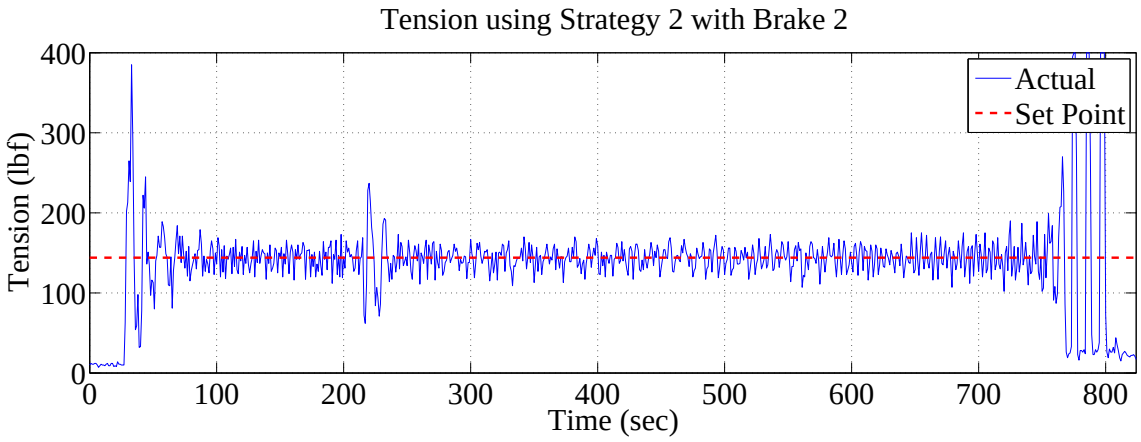

Figure 3.58: Tension for Strategy 2 using Brake 2

can alter the performance of a controller. Since the brake configuration cannot be known beforehand, Strategy 2, with the gains mentioned herein, should not be used to conduct the experiments that will determine if time-varying PID gains can improve the tension performance throughout the entire roll and reduce the tension oscillations with increasing amplitudes seen just prior to the roll depletion. Thus, Strategy 2 will be transformed to exactly match the current control strategy with one difference: the PID gains will vary as in Equations (3.4a) through (3.7d) to attempt to reduce the oscillations seen at the roll depletion. This topic is discussed further in the following subsection.

3.4.3 Current Control Strategy Using Varying PID Gains

This subsection discusses the experimental results of implementing the varying PID gains discussed in Subsection 3.4.2 using the current control strategy employed in the CFL. This strategy will be referred to as Strategy 2a. Note that the only alteration from the current control strategy is that the PID gains will decrease according to Equations (3.4a) and (3.4b) with $K_{p0} = K_{i0} = 0.1$; Strategy 2a does not alter the tension sampling time nor the controller resolution. As discussed previously, the variability between the two brakes decreases the feasibility of permanently replacing the current control strategy with either Strategy 1 or Strategy 2. Thus, the motivation for this experiment is to illustrate the effect of varying the PID gains with time on the tension performance. Similar to the previous experimental discussions, this subsection is divided into two portions, one for each brake. Additionally, note that the sets of data presented herein were selected to provide similar Pull Roll 1 speed profiles for the two control strategies.

Analysis of Brake 1

Figures 3.59 through 3.61 show the measured data corresponding to the current control strategy prior to the experiment and Figs. 3.62 through 3.64 show data collected from the CFL during the implementation of Strategy 2a. Note that the first data set for the current control strategy was collected at a speed 10 fpm slower than the rest of the data. However, the disparity is not great and the profile is similar; thus, this data set is acceptable as a basis for comparison.

The control variables for the two strategies are similar. This is to be expected since the only differences are the gain values. Both control variables initially rise until the upper limit of 80, after which the controller remains saturated for large portions of the roll. Subsequently, the control variables gradually reduce in value until the end of the roll nears where a slight increase is seen. Note that near the roll depletion,

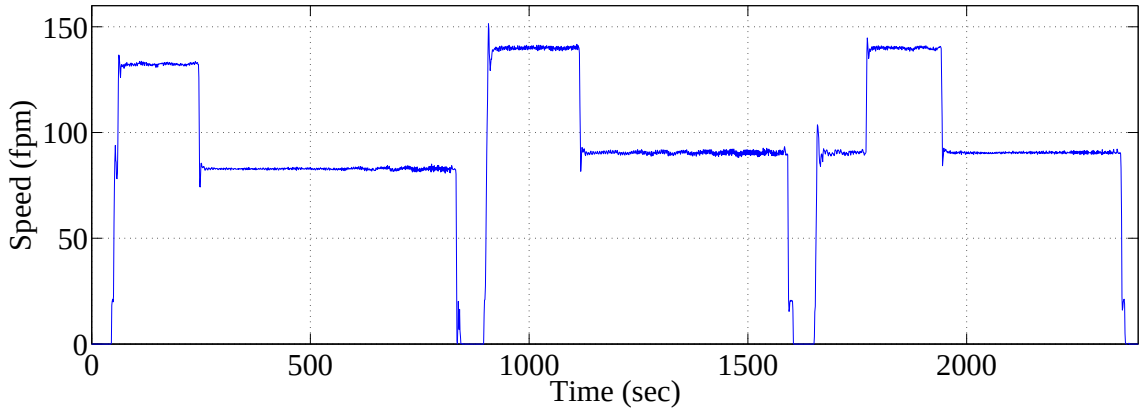

Figure 3.59: Pull Roll 1 speed for the current control strategy using Brake 1 prior to implementation of Strategy 2a

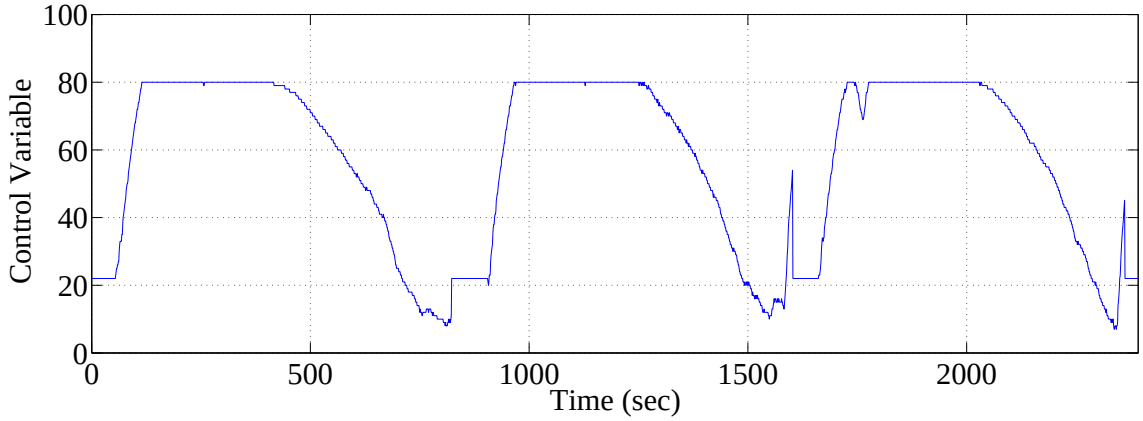

Figure 3.60: Control variable for the current control strategy using Brake 1 prior to implementation of Strategy 2a

the fluctuations in the control variable for Strategy 2a are less in both quantity and rapidity. This is because the gains for Strategy 2a are nearly 10% lower and thus the controller is slower. However, this trend is advantageous during this portion of the roll since variations in the control variable produce changes in the braking torque. These changes in the braking torque have increasing effect on the speed of the Unwind Roll, and thus the tension, as the roll nears depletion. Therefore, variations in the control variable result in the large tension oscillations present just before the material roll is

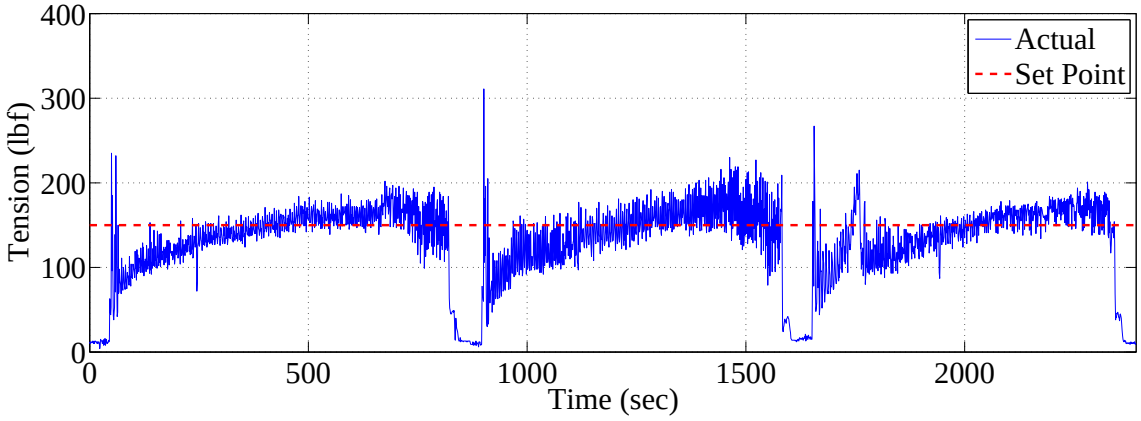

Figure 3.61: Tension for current control strategy using Brake 1 prior to implementation of Strategy 2a

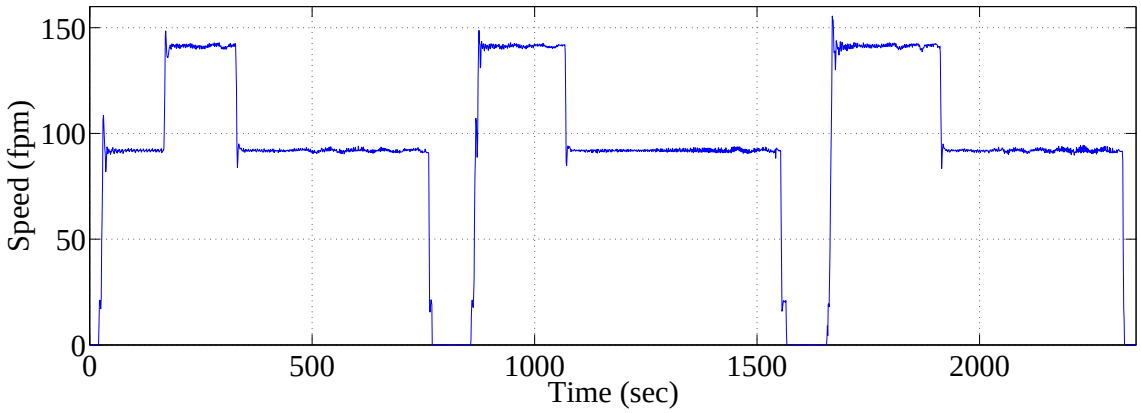

Figure 3.62: Pull Roll 1 Speed for Strategy 2a using Brake 1

empty. The trend seen with Strategy 2a is beneficial as it will reduce the fluctuation of the control variable which will result in decreased tension oscillation amplitudes. Note that the large spike witnessed just prior to the splicing process is due to the depleted material roll which causes a drop in the load cell feedback, resulting in a large controller output.

The tension performance for both strategies are similar for the data sets corresponding to comparable Pull Roll 1 speed profiles. They both exhibit the slow rise time and large overshoot described in Subsection 3.4.1 although Strategy 2a did de-

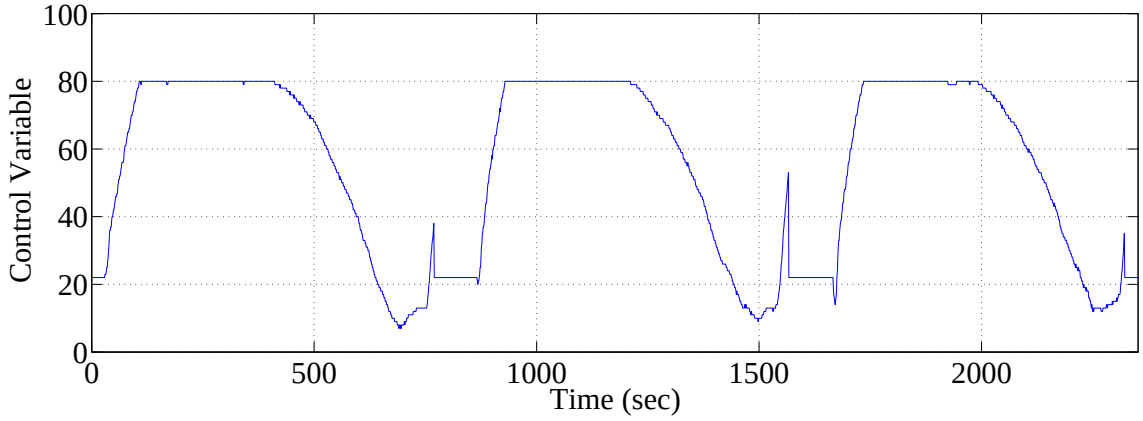

Figure 3.63: Control variable for Strategy 2a using Brake 1

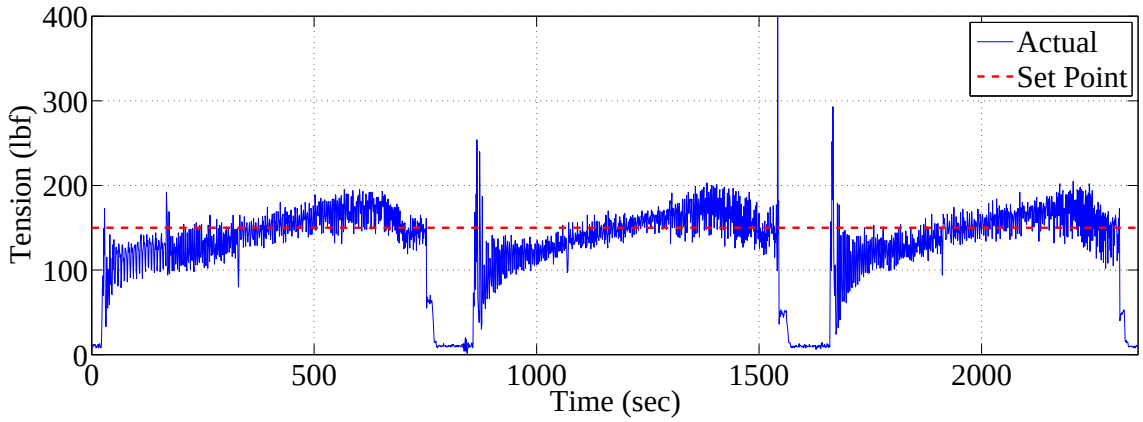

Figure 3.64: Tension for Strategy 2a using Brake 1

crease the amplitude of the oscillations during the beginning and middle portions of the roll. However, due to the decreased gains near the end of the roll, Strategy 2a actually has slightly larger overshoot than the current strategy because the smaller gains make the controller less responsive to tension errors. By comparing the size of the oscillations just before the material roll is depleted, it is seen that, although the improvement is slight, Strategy 2a was successful in reducing the amplitude of the tension oscillations. During this time, the control variable changes at a slower rate, providing smoother alterations in the braking torque. As previously discussed in Section 3.3, this will result in reduced tension oscillation amplitudes. However, it

is noted that the amplitudes were not greatly reduced because the control variable still fluctuates, resulting in braking torque changes that induce tension oscillations.

Analysis of Brake 2

The data collected from the CFL using Brake 2 prior to experimentation is shown in Figs. 3.65 through 3.67, and Figs. 3.68 through 3.70 show the data after implementing Strategy 2a. In the first set of data for the current control strategy, Pull Roll 1 speeds are 10 fpm slower than the rest of the data. However, as was argued in the analysis of Brake 1, the profile matches those used in the other data sets and the speed does not differ substantially. Therefore, this data is suitable for comparison.

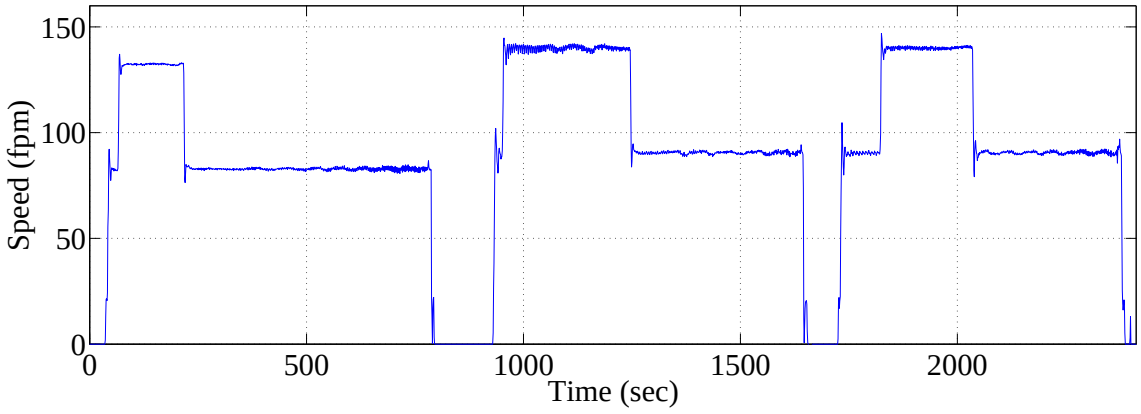

Figure 3.65: Pull Roll 1 speed for the current control strategy using Brake 2 prior to implementation of Strategy 2a

A comparison of Figs. 3.66 and 3.69 shows that the control variables for the two strategies are similar. Note that since the speeds for the first data set of the current control strategy were lower than the others, the control variable for this set did not reach as high of a value. Unlike the results with Brake 1 that had the control variable for Strategy 2a noticeably smoother near the end of the roll, the two strategies for Brake 2 do not have such a distinguishing difference. This is due in part to the fact that the controller resolution is smaller for Brake 2; relative to Brake 1, a single

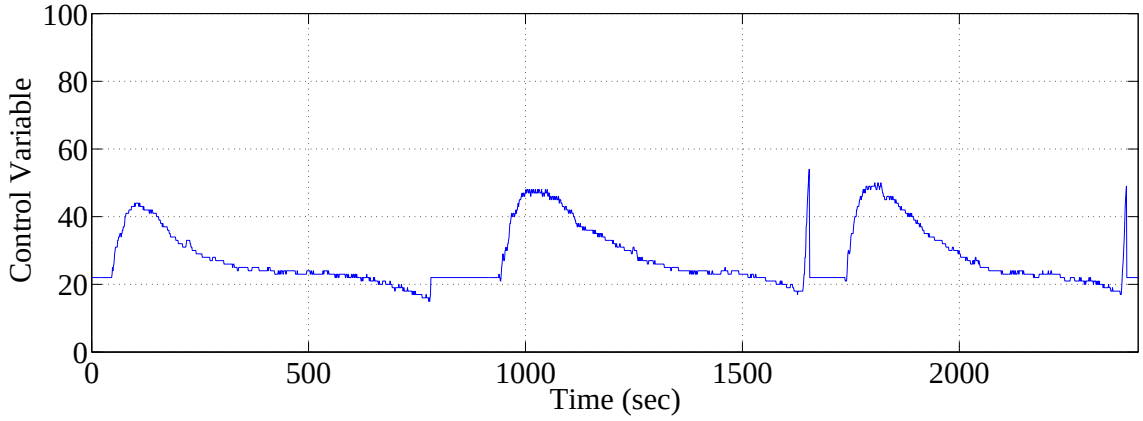

Figure 3.66: Control variable for the current control strategy using Brake 2 prior to implementation of Strategy 2a

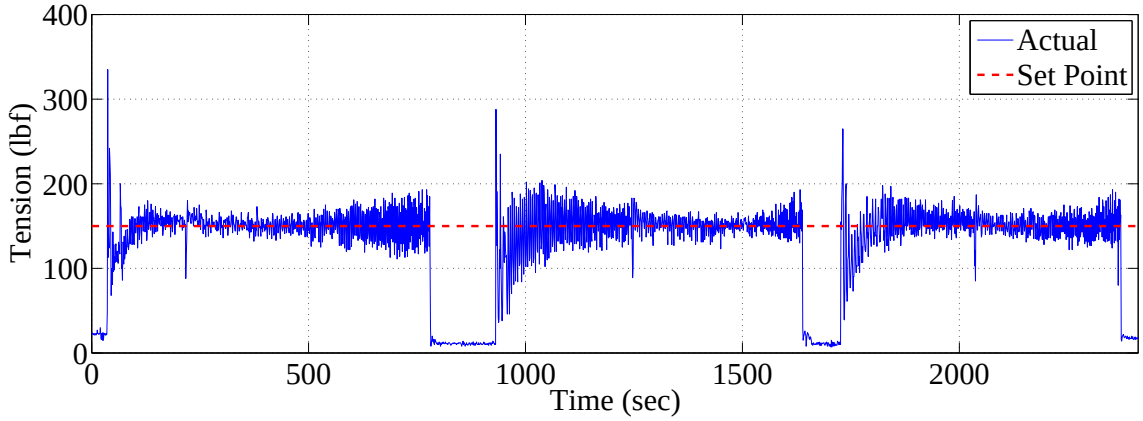

Figure 3.67: Tension for current control strategy using Brake 2 prior to implementation of Strategy 2a

control variable value for Brake 2 corresponds to a larger range of braking torques. This is seen by comparing the control variables for Brakes 1 and 2. For the same size of roll and the same material, Brake 1 saturates whereas Brake 2 only reaches a value of 50. This indicates that, although Brake 1 is not able to apply as large of braking torque, it is able to provide a higher resolution for smaller braking torque values since an incremental change in the control variable results in a smaller change in breaking torque. Thus, even with the smaller gains at the end of the roll, the

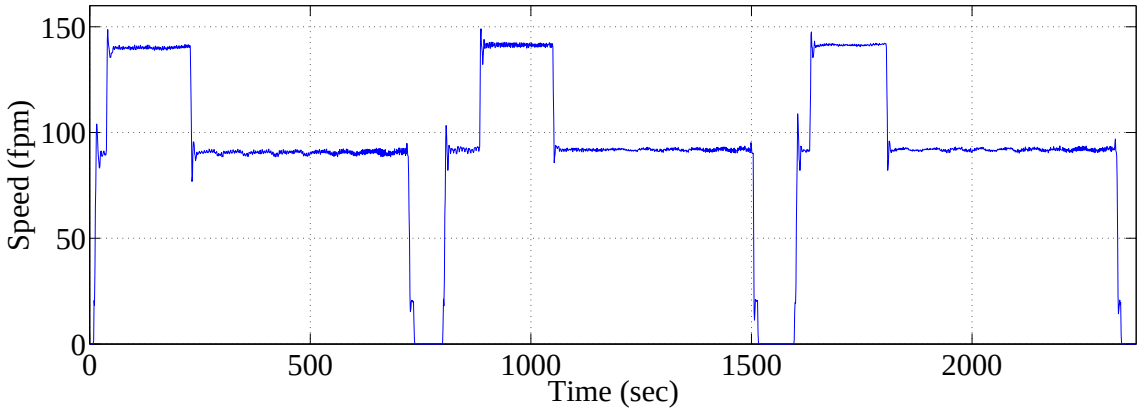

Figure 3.68: Pull Roll 1 Speed for Strategy 2a using Brake 2

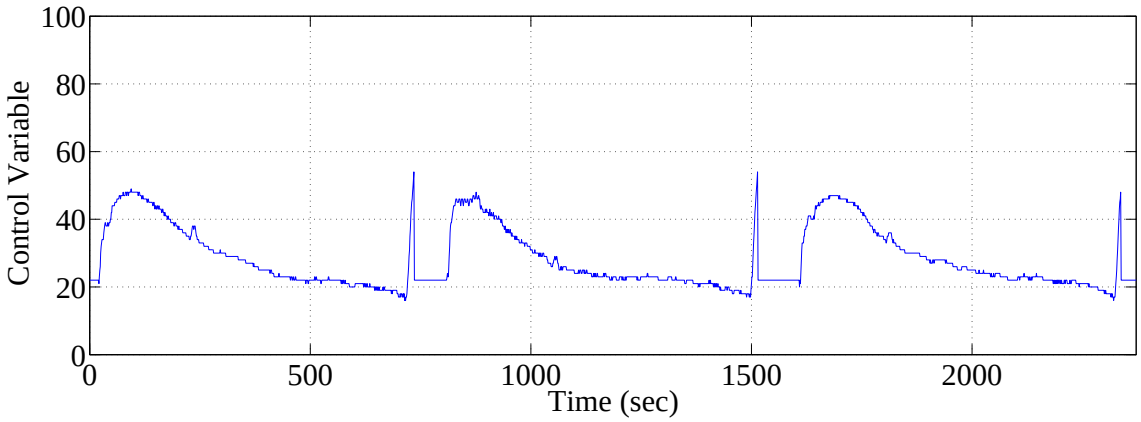

Figure 3.69: Control variable for Strategy 2a using Brake 2

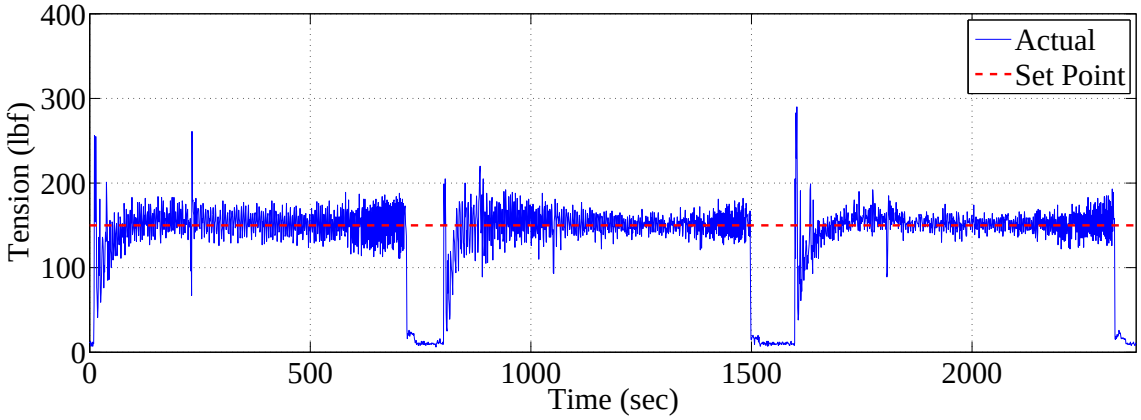

Figure 3.70: Tension for Strategy 2a using Brake 2

tension oscillations created by an incremental change in the braking torque using Brake 2 can cause the control variable to oscillate between values as it attempts to correct this error. Therefore, the smooth transition of the control variable seen with Brake 1 is not present with Brake 2.

A comparison of Fig. 3.67 with Fig. 3.70 shows that the tension performance near the beginning and middle of the roll is improved. The larger gains allowed the controller to be more sensitive to the tension error and thus increase the performance. Near the end of the roll, the tension oscillations are present for both strategies, although Strategy 2a shows a slight improvement. The difference between these two strategies is not more significant because the control variable for Strategy 2a still fluctuated near the depletion of the material roll, thus producing tension oscillations as mentioned in the previous discussion.

Summary

This experiment showed that by decreasing the PI gains as the roll depletes, the tension performance can be improved even while using two differently configured brakes. Strategy 2a was able to improve the tension performance at the beginning and middle portions of the roll using Brake 2. Near the depletion of the material roll, the tension data for both Brakes 1 and 2 showed reduced oscillation amplitudes; however, the improvement for the latter case was slight. It is noted that, although the tension values using Strategy 2a with Brake 1 were above the set point value near the end of each roll, the deviations from the average value had greater reduction than the corresponding tension results using Brake 2. This trend occurred because the control variable for Brake 1 had very few fluctuations during this final portion of the roll whereas the low control variable-to-braking torque resolution prevented Brake 2 from exhibiting this trend. As discussed above, these trends caused Brake 2 to induce larger oscillations in tension near the roll depletion than those induced by Brake 1.

A comparison of Figs. 3.63 and 3.69 illustrates that Brake 1 and Brake 2 were configured differently (i.e., the control variable for the former saturated for each roll whereas the control variable with the latter did not exceed 50). Unlike the experiment discussed in Subsection 3.4.2, Strategy 2a used gains low enough for the given sampling time and controller resolution, so the system remained stable and slightly improved the tension performance.

3.4.4 Strategy 3 Experiment Discussion

Strategy 3 requires the same control variable values to be used for both brakes since the feed-forward portion is independently calculated from the correction portion that utilizes the feedback. As discussed previously in this report, the two brakes are configured independently and are most often configured differently. This results in Brakes 1 and 2 utilizing different control variable ranges in order to regulate the tension. Therefore, the experimental implementation of Strategy 3 on the CFL is impractical since it would not produce control variable values that are satisfactory for both brakes.

3.4.5 Summary of All Experiments

Experiments were conducted on the CFL using Strategies 1 and 2 in order to verify the simulation results given in Section 3.3 and determine which would perform the best in a practical application. Strategy 1 decreased the sampling time and increased the resolution for the tension measurements and controller output. In fact, because of this experiment, the tension measurement resolution on the CFL was permanently altered to the value employed by Strategy 1. It improved the overall tension regulation but was unable to eliminate the tension oscillations present near the roll depletion. Strategy 2 was designed to rectify this problem by decreasing the PI gains as the material roll depleted. However, the brake configuration had been altered in some

fashion and thus the gains that were appropriate for Strategy 1 could no longer be used as they caused unstable results. These results illustrated that alterations that increased the performance with one brake under a certain configuration may degrade the performance for the other brake or even degrade the performance of the same brake with a different configuration. Therefore, in an effort to provide a universally useful improvement over the current control strategy, Strategy 2a, which utilized the same sampling time and controller output resolution as the current control strategy except with PI gains that decreased over the course of the roll, was employed. This provided increased performance during the beginning and middle portions of the material roll while only slightly reducing the tension oscillations present near the roll depletion.

The limitations of the brakes inhibits the effectiveness of the controller and thus the tension performance. Altering the brake configuration essentially changes the PI gains and, as seen from the difference in the control variables from Section 3.4.3, this can have a large impact on the controller output. The gains utilized in Strategy 1 improved the tension performance; however, under a different brake configuration, these gains may not be appropriate. Alterations to the brake configuration for the current control strategy do not cause significant problems since the PI gains are sufficiently small. However, this limits the effectiveness of the controller as is seen in the data for the current control strategy that was collected prior to the experimental implementation of Strategies 2 and 2a. The control variable-to-braking torque resolution is high enough for Brake 1 that, although not able to apply as great of torques as Brake 2, an incremental change in the control variable produces a small enough adjustment in the braking torque that the tension oscillations with increasing amplitude that are seen near the end of the roll when using Brake 2 were not generated. However, the consequences of this configuration is that, in the middle of the roll where the tension exceeds the set point value, the control variable cannot decrease fast enough to reduce

the braking torque and thus the tension. Conversely, the current control strategy using the configuration for Brake 2 is able to supply large braking torques for lesser values of control variable. This results in sufficient tension regulation for the middle portions of the roll since incremental changes in the control variable result in larger alterations of the braking torque which quickly corrects the tension. However, near the end of the roll, these large changes in braking torque produce tension oscillations as discussed previously. From this discussion, it is clear that the uncertainty in the brake configuration prohibits the use of a universal controller that provides improved tension regulation for all portions of a roll.

Therefore, if the brakes remain as they are with nonuniform and inconsistent performances, it is recommended to select a controller that provides sufficient results for both brakes under different configurations while simultaneously improving the tension performance over the current control strategy. Strategy 2a fulfills both of these criteria for the current set of brakes and is thus the suggested controller that will provide the best tension regulation for all portions of the roll. However, if the brakes can be modified such that their performances are uniform and consistent, then Strategy 2 is the recommended controller. The reason for this is that Strategy 1 showed that increasing the tension measurement and control variable resolutions and decreasing the sampling time improves the tension performance over that of the existing strategy. Strategy 2a showed the effectiveness of reducing the gains as the roll depletes. Therefore, since Strategy 2 is a combination of Strategies 1 and 2a, a properly tuned Strategy 2 with brakes that have uniform and consistent performances should result in a controller that provides improved tension regulation performance over that of the existing strategy.

3.5 Conclusion

This chapter discussed the analysis and improvement of the tension control for the section of the CFL from the Unwind Roll to Pull Roll 1. First a model simulation was created from the existing control strategy and the web dynamics, both of which were derived in Chapter 2. This model was then verified by comparing the simulation results to data collected from the CFL. It was shown that the model sufficiently represented the physical system.

Following the model verification, three improvements to the current control strategy, named Strategies 1, 2, and 3, were proposed. Strategy 1 used a faster sampling time and increased the resolution of the tension feedback and controller output. Strategy 2 employed these same improvements but used PI gains that decrease with the Unwind Roll radius. Strategy 3 utilized feed-forward control with a PI to provide corrections. These three improvements were compared to each other and the current control strategy via simulation.

Subsequently, Strategies 1 and 2 were implemented onto the CFL to test their effectiveness in controlling the actual process line. Strategy 1 provided improved performance whereas Strategy 2 produced adverse results. This occurred because the configuration of the brakes had been altered, and the gains that were effective with Strategy 1 became inappropriate. Subsequently Strategy 2 was altered to Strategy 2a which used the current control strategy with the alteration of varying gains. Strategy 2a showed improvement over the current control strategy and was selected as the recommended controller, if the brakes remain as they are where their configurations are inconsistent and nonuniform, as it proved effective even in the presence of differing brake configurations. If the brakes can be modified to have consistent and uniform performances, then Strategy 2 is the recommended controller. Strategy 3 was not implemented due to practical constraints; it requires that both brakes produce the same torque for a given control variable and the brakes are most often configured

differently. Additionally, any alterations to the brake configurations would prove detrimental to the Strategy 3 performance.

It is noted that the results of the experimental implementation of Strategy 1 and Strategy 2 did not match the model simulation results. Additionally, the experimental implementation of Strategy 2a illustrated the efficacy of varying the PI gains better than that shown by the model simulation of Strategy 2. The reason for these trends is that the model lacked some of the characteristics of the actual system. First, the model simulation showed Pull Roll 1 operating at an ideal profile. However, this is not the case in reality since the speed of Pull Roll 1 is being varied by its outer tension loop. Second, the model ignored the idle rollers and the influence they have on the tension dynamics. Additionally, the tension propagation effects from the Unwind Accumulator were also ignored. The dynamics relating the braking pressure to the applied braking torque was assumed to be a constant gain, but in actuality the dynamics are more complicated. They may include a stick-slip friction dynamic that relates the force applied by the brake pressure device to the corresponding friction torque applied to the Unwind Roll. Each of the disturbances and dynamics mentioned above will influence the actual system but not the model since the model does not account for them, resulting in the discrepancies between the measured and simulated data.

Through the implementation of multiple strategies, it was shown that the configurations of the two brakes can differ significantly and this alters the performance of the controller. The different configurations essentially change the PI gains which causes the degradation in the performance of Strategy 2. Analysis of data collected using the current control strategy illustrated that certain aspects of two particular configurations for Brakes 1 and 2 provide sufficient control for different portions of the material roll. Thus it was concluded that, given the obscurity in the brake configuration, no controller is able to greatly improve the tension regulation for all portions

of the roll and for all brake configurations.

CHAPTER 4

Comparison of Torque and Velocity Control

4.1 Introduction

This chapter compares two control strategies of an unwind roll as configured in Fig. 2.7: (1) inner velocity control with an outer tension loop (Fig. 4.1) and (2) torque control that utilizes tension feedback (Fig. 4.2). The former method utilizes a motor whose velocity reference is corrected by the tension loop whereas the latter method employs a brake which applies a torque to the unwind roll based on the tension error. This comparison is useful because it will provide a basis for determining the distinguishing attributes between these two strategies with regard to stability. In the comparison of the control strategies, the PI controller space will be divided into regions where every point in each region corresponds to K_p, K_i pairs that result in a fixed number of unstable closed loop poles [11]. These regions are constructed by mapping the stability boundary in the root space ($j\omega$ axis) to the PI controller parameter space [11].

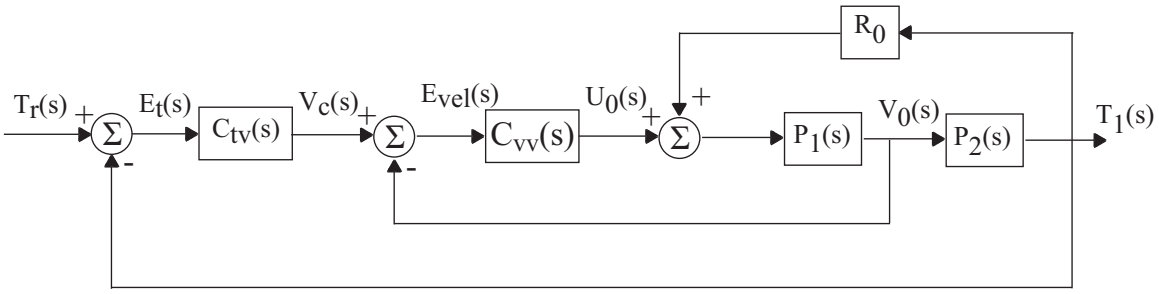

Figure 4.1: Block diagram of velocity controlled unwind roll with outer tension loop

Section 4.2 discusses the stability region mapping procedure for a general system.

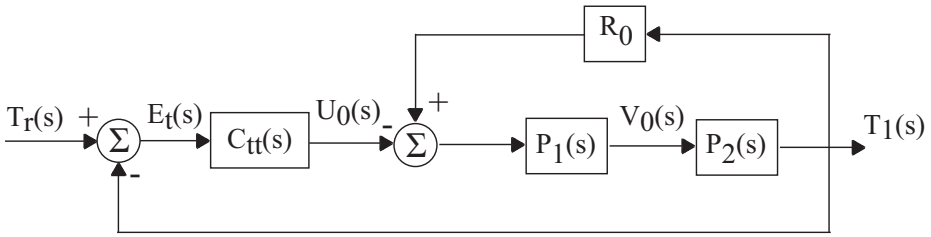

Figure 4.2: Block diagram of torque controlled unwind roll

Section 4.3 derives the stability regions for the velocity controlled unwind roll and Section 4.4 describes this process for the torque unwind roll. This chapter concludes with a comparison of the stability regions for these two control strategies in Section 4.5.

4.2 Stability Boundary Mapping

The following procedure for mapping the stability boundary in the root space to the PI controller space was taken from Reference [11]. Each of the aforementioned strategies can be transformed into Fig. 4.3 where $C(s)$ is the PI controller and $P(s)$ is the plant.

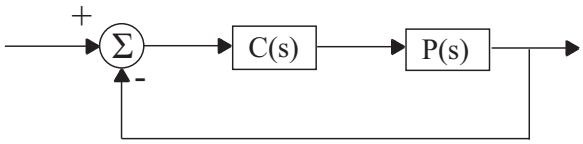

Figure 4.3: General block diagram of plant with controller

This system has a closed loop characteristic equation as shown in Equation (4.1).

$$\delta(s) = (s^2 D_o(s^2) + K_i N_e(s^2) + K_p s^2 N_o(s^2)) + s(D_e(s^2) + K_i N_o(s^2) + K_p N_e(s^2)) \quad (4.1)$$

where $N_e(s^2)$ and $N_o(s^2)$ are the even and odd parts, respectively, of the numerator of $P(s)$ and likewise for the denominator, $D(s)$. Note that $N(s) = N_e(s^2) + sN_o(s^2)$ and $D(s) = D_e(s^2) + sD_o(s^2)$.

Equation (4.1) is evaluated at $s = j\omega$, the stability boundary in the root space, in order to construct the boundary in the controller parameter space. Thus, Equation (4.1) becomes Equation (4.2)

$$\delta(j\omega) = \delta_r(j\omega) + j\omega\delta_i(j\omega) \tag{4.2}$$

where

$$\delta_r(j\omega) = -\omega^2 D_o(-\omega^2) + K_i N_e(-\omega^2) - K_p\omega^2 N_o(-\omega^2) \tag{4.3}$$

$$\delta_i(j\omega) = D_e(-\omega^2) + K_i N_o(-\omega^2) + K_p N_e(-\omega^2). \tag{4.4}$$

4.2.1 Stable to Unstable Transition

A root or pair of roots can pass from the stable region of the root space to unstable (or vice versa) in three ways:

1. A real root can pass through the origin
2. A pair of complex roots can traverse the imaginary axis at $\omega \in (0, \infty)$
3. A real root can pass through infinity

Stability Boundary at the Root Space Origin

The stability boundary at the origin of the root space is the set of all K_p, K_i pairs such that

$$\delta(j\omega)|_{\omega=0} = 0. \tag{4.5}$$

From Equations (4.2), the corresponding stability boundary in the parameter space is given by

$$K_i = 0. \tag{4.6}$$

Complex Axis Stability Boundary

The stability boundary in the controller parameter space corresponding to the complex axis in the root space is composed of all K_p, K_i pairs such that, for all $\omega \in (0, +\infty)$,

$$\delta(j\omega) = 0. \tag{4.7}$$

From Equations (4.2) through (4.4), the above condition corresponds to

$$\mathbf{F}(\omega)\mathbf{K} = \mathbf{B} \tag{4.8}$$

where

$$\mathbf{F}(\omega) = \begin{bmatrix} -\omega^2 N_o(-\omega^2) & N_e(-\omega^2) \\ N_e(-\omega^2) & N_o(-\omega^2) \end{bmatrix}$$

$$\mathbf{K} = \begin{bmatrix} K_p \\ K_i \end{bmatrix}$$

$$\mathbf{B} = \begin{bmatrix} \omega^2 D_o(-\omega^2) \\ -D_e(-\omega^2) \end{bmatrix}.$$

Solving Equation (4.8) for K_p and K_i yields

$$K_p(\omega) = \frac{-\omega^2 N_o(-\omega^2) D_o(-\omega^2) - N_e(-\omega^2) D_e(-\omega^2)}{|\mathbf{F}(\omega)|} \tag{4.9}$$

$$K_i(\omega) = \frac{\omega^2 N_e(-\omega^2) D_o(-\omega^2) - \omega^2 N_o(-\omega^2) D_e(-\omega^2)}{|\mathbf{F}(\omega)|}. \tag{4.10}$$

Evaluating Equations (4.9) and (4.10) for ω from 0 to $+\infty$ results in the stability boundary in the parameter space corresponding to the $j\omega$ axis in the root space. It is noted that solutions to Equation (4.8) only exist for $|\mathbf{F}(\omega)| \neq 0$ for $\omega > 0$. The conditions for which $|\mathbf{F}(\omega)| = 0$ when $\omega > 0$ for each system under consideration will be shown later.

Stability Boundary at Infinity

A real root passes from stable to unstable (or vice versa) through infinity only when the degree of $\delta(s)$ decreases. It will be seen later that, since the plants in both systems under consideration are strictly proper, the leading coefficient of $\delta(s)$ is a fixed constant that is not a function of K_p nor K_i. Thus, this condition does not apply.

Therefore, the only conditions that need to be considered are the boundaries corresponding to a real root passing through the origin of the root space (Equation (4.6)) and a complex pair crossing the $j\omega$ axis (Equations (4.9) and (4.10)). Equations (4.6), (4.9) and (4.10) delineate curves in the controller parameter space that divide the space into several regions. Each of these regions contain K_p, K_i pairs that correspond to controllers that produce a fixed number of unstable closed loop poles. Thus if any region produces zero unstable closed loop poles, then for any K_p, K_i pair within that region, there exists a PI controller that is able to stabilize the plant. However, if such a region does not exist, then a PI controller is unable to stabilize the plant.

Note that in order to be confident that all regions have been found, Equations (4.9) and (4.10) must be evaluated over $\omega \in [0, +\infty)$. The initial location of the boundary is known at $\omega = 0$; however, the final behavior of the boundary is not known since this would require an infinite number of evaluations of Equations (4.9) and (4.10). In the proceeding analysis, ω is evaluated over a large enough range so that the major regions are found.

4.3 Controller Parameter Stability Regions for Velocity Control

The block diagram for a velocity controlled unwind roll with outer tension control is shown in Fig. 4.1. $P_1(s)$ and $P_2(s)$ are the transfer functions relating the applied torques of the unwind roll to $V_0(s)$ and $V_0(s)$ to $T_1(s)$, respectively, and were derived

from Equations (2.47) through (2.49) assuming $n_0 = 1$. $C_{tv}(s)$ and $C_{vv}(s)$ are the PI controllers for tension and velocity, respectively. $P_1(s)$, $P_2(s)$, $C_{tv}(s)$, and $C_{vv}(s)$ are given below.

$$P_1(s) = \frac{R_0}{J_0 s} \tag{4.11}$$

$$P_2(s) = \frac{\mu_1 EA(\tau_2 s + 1)}{(\tau_3 s + 1)(\tau_1 s + 1)} \tag{4.12}$$

$$C_{tv}(s) = \frac{K_{ptv} s + K_{itv}}{s} \tag{4.13}$$

$$C_{vv}(s) = \frac{K_{pvv} s + K_{ivv}}{s} \tag{4.14}$$

where

$$\mu_1 = \frac{\varepsilon_r - 1}{v_r}$$

$$\tau_1 = \frac{b}{E_v}$$

$$\tau_2 = \frac{b(E_v + E)}{E_v E}$$

$$\tau_3 = \frac{L_1}{v_r}$$

The stability boundary calculation is split into two steps. First, the boundary for the inner velocity loop is calculated to determine a K_{pvv}, K_{ivv} pair that stabilizes the inner velocity loop. Then, using these gains, the stability boundary for the outer tension loop is determined.

4.3.1 Inner Velocity Loop Stability Boundary

The inner velocity loop is shown in Fig. 4.4.

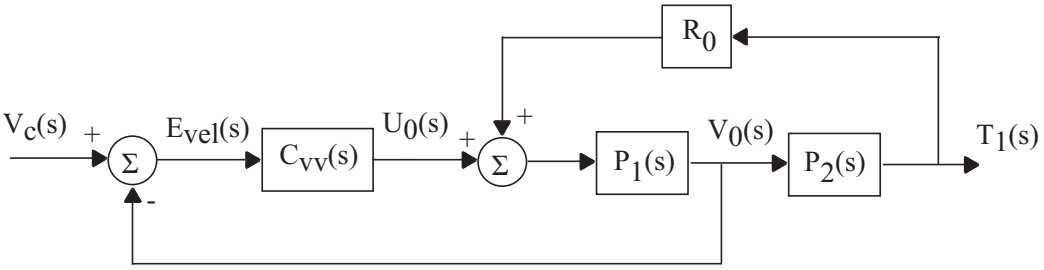

Figure 4.4: Block diagram of inner velocity loop

The closed loop transfer function, T_1/V_c, is determined to be

$$\frac{T_1(s)}{V_c(s)} = \frac{(K_{pvv}\, s + K_{ivv})\,(\tau_2\, s + 1)\, AE\mu_1\, R_0}{\delta_{vv}(s)} = P_3(s) \tag{4.15}$$

where

$$\begin{aligned}\delta_{vv}(s) =& J_0\, \tau_3\, \tau_1 s^4 + (J_0\, \tau_3 + J_0\, \tau_1 + R_0\, K_{pvv}\, \tau_3\, \tau_1)\, s^3 \\ &+ \left(R_0\, K_{ivv}\, \tau_3\, \tau_1 + R_0\, K_{pvv}\, \tau_3 + R_0\, K_{pvv}\, \tau_1 - {R_0}^2 \mu_1\, EA\tau_2 + J_0\right) s^2 \\ &+ \left(-{R_0}^2 \mu_1\, EA + R_0\, K_{ivv}\, \tau_3 + R_0\, K_{ivv}\, \tau_1 + R_0\, K_{pvv}\right) s + R_0\, K_{ivv}\end{aligned} \tag{4.16}$$

is the characteristic equation for the velocity loop. Setting $s = j\omega$ gives

$$\delta_{vv}(j\omega) = \delta_{rvv}(\omega) + j\omega\delta_{ivv}(\omega) \tag{4.17}$$

where

$$\begin{aligned}\delta_{rvv}(\omega) =& \left(-\omega^2 R_0\, \tau_3\, \tau_1 + R_0\right) K_{ivv} + \left(-\omega^2 R_0\, \tau_1 - \omega^2 R_0\, \tau_3\right) K_{pvv} \\ &+ J_0\, \omega^4 \tau_3\, \tau_1 + \omega^2 {R_0}^2 \mu_1\, EA\tau_2 - \omega^2 J_0\end{aligned} \tag{4.18}$$

$$\delta_{ivv}(\omega) = (R_0\,\tau_3 + R_0\,\tau_1)\,K_{ivv} + \left(-\omega^2 R_0\,\tau_3\,\tau_1 + R_0\right)K_{pvv} \\ -\,\omega^2 J_0\,\tau_3 - \omega^2 J_0\,\tau_1 - {R_0}^2\mu_1\,EA. \tag{4.19}$$

As mentioned in Section 4.2, the real root boundary at the origin is

$$K_{ivv} = 0. \tag{4.20}$$

To calculate the stability boundary corresponding to the imaginary axis, Equation (4.8) is used with

$$\mathbf{F}(\omega) = \mathbf{F_{vv}}(\omega) = \begin{bmatrix} -\omega^2 R_0\tau_1 - \omega^2 R_0\tau_3 & -\omega^2 R_0\tau_3\tau_1 + R_0 \\ -\omega^2 R_0\tau_3\tau_1 + R_0 & R_0\tau_3 + R_0\tau_1 \end{bmatrix} \tag{4.21}$$

$$\mathbf{K} = \mathbf{K_{vv}} = \begin{bmatrix} K_{pvv} \\ K_{ivv} \end{bmatrix} \tag{4.22}$$

$$\mathbf{B}(\omega) = \mathbf{B_{vv}}(\omega) = \begin{bmatrix} -J_0\omega^4\tau_3\tau_1 - \omega^2 {R_0}^2\mu_1 EA\tau_2 + \omega^2 J_0 \\ \omega^2 J_0\tau_3 + \omega^2 J_0\tau_1 + {R_0}^2\mu_1 EA \end{bmatrix}. \tag{4.23}$$

$\mathbf{K_{vv}}$ has a unique solution if $|\mathbf{F_{vv}}(\omega)| \neq 0$ for $\omega > 0$. $|\mathbf{F_{vv}}(\omega)|$ for the inner velocity loop is given below.

$$|\mathbf{F_{vv}}(\omega)| = -{R_0}^2\left(\omega^2{\tau_1}^2 + 1\right)\left(\omega^2{\tau_3}^2 + 1\right) \tag{4.24}$$

The only condition under which $|\mathbf{F_{vv}}(\omega)| = 0$ is when $R_0 = 0$, which is not possible. Thus, $|\mathbf{F_{vv}}(\omega)| \neq 0$ and hence $\mathbf{K_{vv}}$ has a unique solution. Solving Equation (4.8) with $\mathbf{F_{vv}}(\omega)$, $\mathbf{K_{vv}}$, and $\mathbf{B_{vv}}(\omega)$ gives the expressions for the K_{pvv} and K_{ivv} that correspond to the $j\omega$ axis in the root space. These are given below.

$$K_{pvv}(\omega) = \frac{R_0\,\mu_1\,EA\,(\omega^2\tau_3\,\tau_2 + \omega^2\tau_1\,\tau_2 - \omega^2\tau_3\,\tau_1 + 1)}{\omega^2{\tau_1}^2 + \omega^2{\tau_3}^2 + \omega^4{\tau_3}^2{\tau_1}^2 + 1} \tag{4.25}$$

$$K_{ivv}(\omega) = \frac{\omega^2}{R_0\left(\omega^2{\tau_1}^2 + \omega^2{\tau_3}^2 + \omega^4{\tau_3}^2{\tau_1}^2 + 1\right)}\Big(\omega^4{\tau_3}^2{\tau_1}^2 J_0 \tag{4.26}$$
$$+\omega^2\tau_3\tau_1 {R_0}^2\mu_1 EA\tau_2 - {R_0}^2\mu_1 EA\tau_2 + J_0 + \omega^2 J_0{\tau_3}^2$$
$$+\tau_3 {R_0}^2\mu_1 EA + \omega^2 J_0{\tau_1}^2 + \tau_1 {R_0}^2\mu_1 EA\Big)$$

Using Equations (4.20), (4.25), and (4.26) along with the parameters given in Table 4.1, the stability boundary in the velocity controller parameter space is determined and is shown in Fig. 4.5. The number of unstable closed loop poles for each region are shown on the plot. As can been seen, any ($K_{pvv} > 0$, $K_{ivv} > 0$) pair, as well as some ($K_{pvv} < 0$, $K_{ivv} > 0$) pairs, will stabilize the inner velocity loop. However, only positive velocity loop PI gains will be considered.

Table 4.1: Web Line Parameters

Parameter	Value	Units
A	0.0470	ft^2
E	9.75×10^5	lbf/ft^2
E_v	9.75×10^6	lbf/ft^2
b	5.01×10^7	lbf·s/ft^2
ε_r	1.3208×10^{-3}	ft/ft
J_0	746.0046	slug·ft^2
L_1	26.69	ft
R_0	1.8657	ft
t_r	92	lbf
v_r	1.6667	ft/s

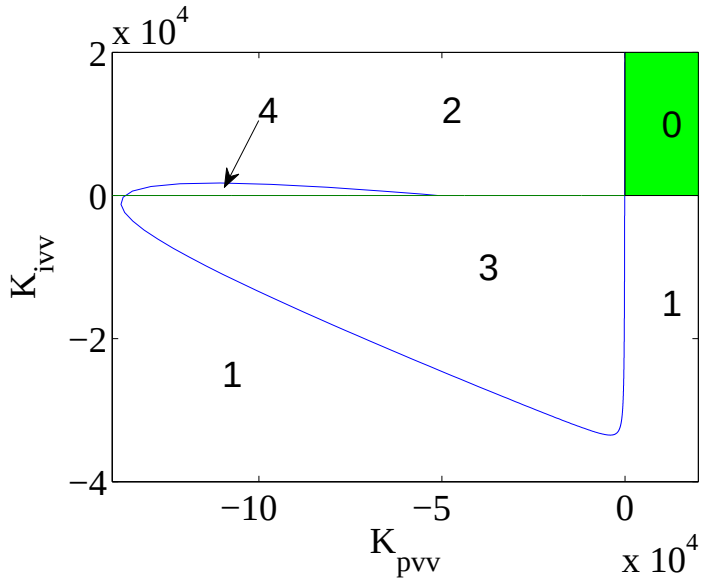

Figure 4.5: Root invariant regions in K_{pvv}-K_{ivv} space for velocity loop (the number of unstable poles in each region is indicated)

4.3.2 Outer Tension Loop Stability Boundary for Velocity Control

The stability boundary in the outer tension PI parameter space is found by assuming the inner velocity loop to be the plant and thus transforming Fig. 4.1 to Fig. 4.6. The results from Section 4.3.1 will be used to select K_{pvv} and K_{ivv} values such that the inner velocity loop is stable. Thus, the controller parameter space that will be analyzed in this section is the K_{ptt}-K_{itt} space.

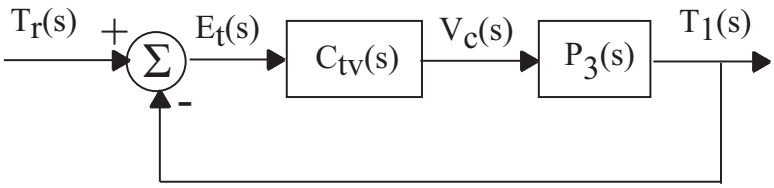

Figure 4.6: Block Diagram of the Outer Tension Loop

From Fig. 4.6, the closed loop transfer function is

$$\frac{T_1(s)}{T_r(s)} = \frac{Tr\ (K_{ptv}\, s + K_{itv})\,(K_{pvv}\, s + K_{ivv})\,(\tau_2\, s + 1)\, R_0\, \mu_1\, EA}{\delta_{tv}(s)} \tag{4.27}$$

where

$$\begin{aligned}\delta_{tv}(s) =& J_0\,\tau_3\,\tau_1 s^5 + (R_0\,K_{pvv}\,\tau_3\,\tau_1 + J_0\,\tau_3 + J_0\,\tau_1)\,s^4 \\ &+ (R_0\,\mu_1\,EA\tau_2\,K_{pvv}\,K_{ptv} + R_0\,K_{ivv}\,\tau_3\,\tau_1 + R_0\,K_{pvv}\,\tau_3 + R_0\,K_{pvv}\,\tau_1 \\ &- {R_0}^2\mu_1\,EA\tau_2 + J_0)\,s^3 + (R_0\,\mu_1\,EAK_{pvv}\,K_{ptv} + R_0\,K_{ivv}\,\tau_3 \\ &+ R_0\,\mu_1\,EA\tau_2\,K_{pvv}\,K_{itv} - {R_0}^2\mu_1\,EA + R_0\,K_{ivv}\,\tau_1 + R_0\,\mu_1\,EA\tau_2\,K_{ivv}\,K_{ptv} \\ &+ R_0\,K_{pvv})\,s^2 + (R_0\,\mu_1\,EAK_{pvv}\,K_{itv} + R_0\,\mu_1\,EAK_{ivv}\,K_{ptv} + R_0\,\mu_1\,EA\tau_2\,K_{ivv}\,K_{itv} \\ &+ R_0\,K_{ivv})\,s + R_0\,\mu_1\,EAK_{ivv}\,K_{itv}\end{aligned} \tag{4.28}$$

is the characteristic equation of the closed loop system. Setting $s = j\omega$ gives

$$\delta_{tv}(j\omega) = \delta_{rtv}(\omega) + j\omega\delta_{itv}(\omega) \tag{4.29}$$

where

$$\begin{aligned}\delta_{rtv}(\omega) =& \left(-\omega^2 R_0\,\mu_1\,EA\tau_2\,K_{pvv} + R_0\,\mu_1\,EAK_{ivv}\right)K_{itv} \\ &+ \left(-\omega^2 R_0\,\mu_1\,EAK_{pvv} - \omega^2 R_0\,\mu_1\,EA\tau_2\,K_{ivv}\right)K_{ptv} + \omega^4 R_0\,K_{pvv}\,\tau_3\,\tau_1 \\ &+ \omega^4 J_0\,\tau_3 + \omega^4 J_0\,\tau_1 - \omega^2 R_0\,K_{ivv}\,\tau_1 - \omega^2 R_0\,K_{ivv}\,\tau_3 + \omega^2 {R_0}^2\mu_1\,EA - \omega^2 R_0\,K_{pvv}\end{aligned} \tag{4.30}$$

$$\begin{aligned}\delta_{itv}(\omega) =& (R_0\,\mu_1\,EAK_{pvv} + R_0\,\mu_1\,EA\tau_2\,K_{ivv})\,K_{itv} \\ &+ \left(-\omega^2 R_0\,\mu_1\,EA\tau_2\,K_{pvv} + R_0\,\mu_1\,EAK_{ivv}\right)K_{ptv} - \omega^2 R_0\,K_{pvv}\,\tau_3 \\ &+ \omega^2 {R_0}^2\mu_1\,EA\tau_2 - \omega^2 R_0\,K_{pvv}\,\tau_1 - \omega^2 J_0 - \omega^2 R_0\,K_{ivv}\,\tau_3\,\tau_1 + R_0\,K_{ivv} + J_0\,\omega^4\tau_3\,\tau_1.\end{aligned} \tag{4.31}$$

From Equation (4.6), the stability boundary at the origin of the root space corresponds to the following in the K_{ptv}-K_{itv} space

$$K_{itv} = 0. \tag{4.32}$$

To derive the stability boundary in the controller parameter space corresponding to the $j\omega$ axis in the root space, Equation (4.8) is used with

$$\mathbf{F}(\omega) = \mathbf{F_{tv}}(\omega) = \begin{bmatrix} -\omega^2 R_0\,\mu_1\,EAK_{pvv} - \omega^2 R_0\,\mu_1\,EA\tau_2\,K_{ivv} \\ -\omega^2 R_0\,\mu_1\,EA\tau_2\,K_{pvv} + R_0\,\mu_1\,EAK_{ivv} \\ -\omega^2 R_0\,\mu_1\,EA\tau_2\,K_{pvv} + R_0\,\mu_1\,EAK_{ivv} \\ R_0\,\mu_1\,EAK_{pvv} + R_0\,\mu_1\,EA\tau_2\,K_{ivv} \end{bmatrix} \tag{4.33}$$

$$\mathbf{K} = \mathbf{K_{tv}} = \begin{bmatrix} K_{ptv} \\ K_{itv} \end{bmatrix} \tag{4.34}$$

$$\mathbf{B}(\omega) = \mathbf{B_{tv}}(\omega) = \begin{bmatrix} -\omega^4 R_0\,K_{pvv}\,\tau_3\,\tau_1 - \omega^4 J_0\,\tau_3 - \omega^4 J_0\,\tau_1 + \omega^2 R_0\,K_{ivv}\,\tau_1 \cdots \\ \omega^2 R_0\,K_{pvv}\,\tau_3 - \omega^2 {R_0}^2\mu_1\,EA\tau_2 + \omega^2 R_0\,K_{pvv}\,\tau_1 \cdots \\ \cdots + \omega^2 R_0\,K_{ivv}\,\tau_3 - \omega^2 {R_0}^2\mu_1\,EA + \omega^2 R_0\,K_{pvv} \\ \cdots + \omega^2 J_0 + \omega^2 R_0\,K_{ivv}\,\tau_3\,\tau_1 - R_0\,K_{ivv} - J_0\,\omega^4\tau_3\,\tau_1 \end{bmatrix}. \tag{4.35}$$

The $|\mathbf{F_{tv}}(\omega)|$ is given below.

$$|\mathbf{F_{tv}}(\omega)| = -{R_0}^2{\mu_1}^2E^2A^2\left(\omega^2{\tau_2}^2 + 1\right)\left(\omega^2{K_{pvv}}^2 + {K_{ivv}}^2\right) \tag{4.36}$$

Thus, the only conditions under which $|\mathbf{F_{tv}}(\omega)| = 0$ are:

1. $R_0 = 0$
2. $t_r = EA$
3. $E = 0$
4. $A = 0$
5. $K_{pvv} = K_{ivv} = 0$

Conditions 1, 3, and 4 are physically impossible and condition 2 is not satisfied for most materials. Thus, as long as at least one of the velocity PI gains is nonzero, $\mathbf{K_{tv}}(\omega)$ will have a unique solution.

Solving Equation (4.8) with $\mathbf{F_{tv}}(\omega)$, $\mathbf{K_{tv}}$, and $\mathbf{B_{tv}}(\omega)$ gives the expressions for the K_{ptv} and K_{itv} that correspond to the $j\omega$ axis in the root space. These relations are given below.

$$\begin{aligned} K_{ptv}(\omega) =& \frac{-1}{R_0\,\mu_1\,EA\,(\omega^2{\tau_2}^2+1)\left(\omega^2{K_{pvv}}^2+{K_{ivv}}^2\right)}\left(-\omega^6\tau_2\,K_{pvv}\,J_0\,\tau_3\,\tau_1\right. \\ &+\left({\tau_2}\,{K_{pvv}}^2R_0\,\tau_1-R_0\,{K_{pvv}}^2\tau_3\,\tau_1+K_{ivv}\,J_0\,\tau_3\,\tau_1-{\tau_2}^2K_{pvv}\,{R_0}^2\mu_1\,EA\right. \\ &-\tau_2\,K_{ivv}\,J_0\,\tau_3+\tau_2\,{K_{pvv}}^2R_0\,\tau_3-K_{pvv}\,J_0\,\tau_3+\tau_2\,K_{pvv}\,J_0-\tau_2\,K_{ivv}\,J_0\,\tau_1 \\ &\left.-K_{pvv}\,J_0\,\tau_1\right)\omega^4+\left(-K_{pvv}\,{R_0}^2\mu_1\,EA-K_{ivv}\,J_0+R_0\,{K_{pvv}}^2-R_0\,{K_{ivv}}^2\tau_3\,\tau_1\right. \\ &\left.\left.+\tau_2\,{K_{ivv}}^2R_0\,\tau_3+\tau_2\,{K_{ivv}}^2R_0\,\tau_1\right)\omega^2+R_0\,{K_{ivv}}^2\right) \end{aligned} \tag{4.37}$$

$$\begin{aligned} K_{itv}(\omega) =& \frac{\omega^2}{R_0\,\mu_1\,EA\,(\omega^2{\tau_2}^2+1)\left(\omega^2{K_{pvv}}^2+{K_{ivv}}^2\right)}\left(\left({\tau_2}\,{K_{pvv}}^2R_0\,\tau_3\,\tau_1\right.\right. \\ &\left.+\tau_2\,K_{pvv}\,J_0\,\tau_3+\tau_2\,K_{pvv}\,J_0\,\tau_1-\tau_2\,K_{ivv}\,J_0\,\tau_3\,\tau_1-K_{pvv}\,J_0\,\tau_3\,\tau_1\right)\omega^4 \\ &+\left(-K_{ivv}\,J_0\,\tau_3-\tau_2\,{K_{pvv}}^2R_0+\tau_2\,K_{ivv}\,J_0-K_{ivv}\,J_0\,\tau_1+R_0\,{K_{pvv}}^2\tau_1+K_{pvv}\,J_0\right. \\ &-{\tau_2}^2K_{ivv}\,{R_0}^2\mu_1\,EA+\tau_2\,{K_{ivv}}^2R_0\,\tau_3\,\tau_1+R_0\,{K_{pvv}}^2\tau_3\Big)\omega^2-\tau_2\,{K_{ivv}}^2R_0 \\ &\left.+R_0\,{K_{ivv}}^2\tau_1-K_{ivv}\,{R_0}^2\mu_1\,EA+R_0\,{K_{ivv}}^2\tau_3\right) \end{aligned} \tag{4.38}$$

Equations (4.32), (4.37), and (4.38) can now be used to delineate the K_{ptv}-K_{itv} parameter space into the various stability regions. Note that the values of the PI gains of the velocity loop influence $K_{ptv}(\omega)$ and $K_{itv}(\omega)$. Consider the following expression for K_{ivv}.

$$\bar{K}_{ivv}=\frac{K_{pvv}\,\left(\tau_2\,K_{pvv}\,R_0\,\tau_3\,\tau_1+\tau_2\,J_0\,\tau_3+\tau_2\,J_0\,\tau_1-J_0\,\tau_3\,\tau_1\right)}{\tau_2\,J_0\,\tau_3\,\tau_1} \tag{4.39}$$

Substituting this expression into Equation (4.38) eliminates the ω^6 term and thus, for large ω, K_{itv} becomes a constant. Selecting $K_{pvv} = 1$ and using the parameters from Table 4.1, the stability boundaries are shaped as shown in Fig. 4.7. However, selecting $K_{ivv} > \bar{K}_{ivv}$ results in a negative ω^6 term and, since $\mu_1 < 0$, $\lim_{\omega\to\infty} K_{itv} = +\infty$. Figure 4.8 displays the root invariant regions for this scenario. Similarly, choosing $0 < K_{ivv} < \bar{K}_{ivv}$ yields a positive ω^6 term and thus $\lim_{\omega\to\infty} K_{itv} = -\infty$. The stability boundaries for this case are presented in Fig. 4.9.

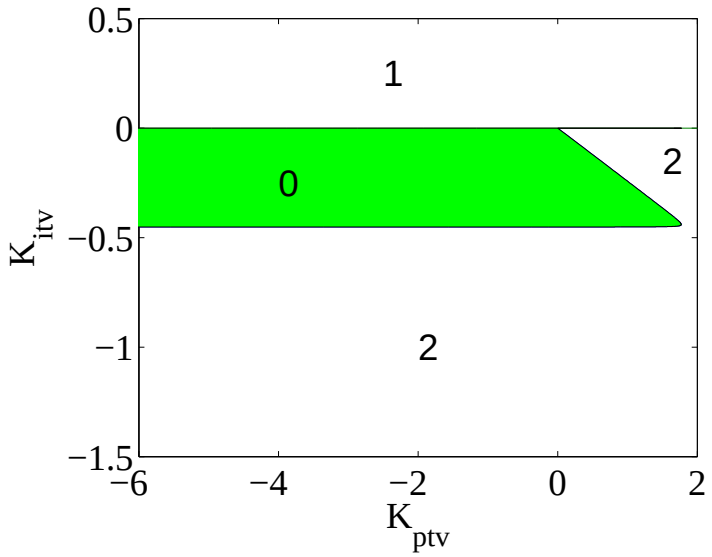

Figure 4.7: Root invariant regions in K_{ptv}-K_{itv} space for $K_{pvv} = 1$ and $K_{ivv} = \bar{K}_{ivv}$ (the number of unstable poles in each region is indicated)

Comparing Figs. 4.7 through 4.9 reveals that the relative values of K_{ivv} and K_{pvv} greatly alter the size and shape of the region in the K_{ptv}-K_{itv} space that contains stable controller gains. Additionally, note that, for each scenario, stability requires $K_{itv} < 0$. It is also noted that there are an infinite number of (K_{ivv}, K_{pvv}) combinations and thus an infinite number of delineations in the K_{ptv}-K_{itv} space. From extensive analysis and trial-and-error, it was determined that the various permutations only add small (on the order of 10^{-4}), unstable regions. The ω values corresponding to these regions

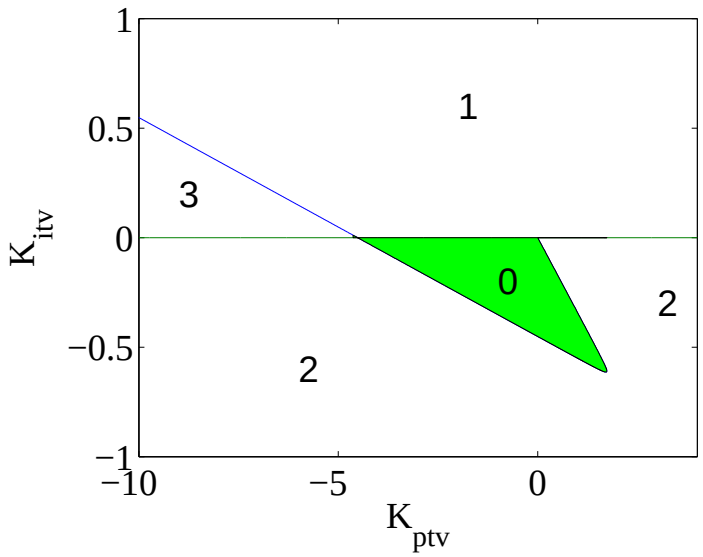

Figure 4.8: Root invariant regions in K_{ptv}-K_{itv} space for $K_{pvv} = 1$ and $K_{ivv} > \bar{K}_{ivv}$ (the number of unstable poles in each region is indicated)

are also small. Nonetheless, the general shape of the boundaries are unchanged and they are consistent with those described above.

4.4 Tension Loop Stability Boundary for Torque Control

The block diagram for the torque controlled unwind roll is shown in Fig. 4.2 where $P_1(s)$ and $P_2(s)$ are as defined above and $C_{tt}(s)$ is the tension PI controller defined below.

$$C_{tt}(s) = \frac{K_{ptt}s + K_{itt}}{s} \tag{4.40}$$

Figure 4.2 indicates that tension feedback is used in the PI controller to produce a braking torque that is applied to the unwind roll as compared to using tension feedback to correct the velocity reference as was seen in the velocity control scenario. Note that the actuator is assumed to be a constant gain.

The characteristic equation for this system is given below.

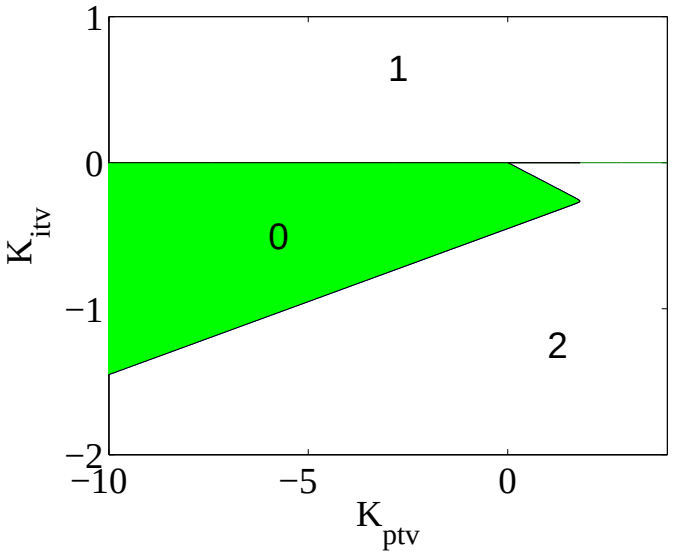

Figure 4.9: Root invariant regions in K_{ptv}-K_{itv} space for $K_{pvv} = 1$ and $K_{ivv} < \bar{K}_{ivv}$ (the number of unstable poles in each region is indicated)

$$\begin{aligned}\delta_{tt}(s) =& J_0\, s^4 \tau_3\, \tau_1 + (J_0\, \tau_1 + J_0\, \tau_3)\, s^3 \\ &+ \left(-\mu_1\, EAR_0\, \tau_2\, K_{ptt} - \mu_1\, {EAR_0}^2 \tau_2 + J_0\right) s^2 \\ &+ \left(-\mu_1\, EAR_0\, \tau_2\, K_{itt} - \mu_1\, EAR_0\, K_{ptt} - \mu_1\, {EAR_0}^2\right) s - \mu_1\, EAR_0\, K_{itt}\end{aligned} \tag{4.41}$$

Setting $s = j\omega$ gives

$$\delta_{tt}(j\omega) = \delta_{ttr}(\omega) + j\omega\delta_{tti}(\omega) \tag{4.42}$$

where

$$\begin{aligned}\delta_{ttr}(\omega) =& J_0\, \omega^4 \tau_3\, \tau_1 + \left(\mu_1\, EAR_0\, \tau_2\, K_{ptt} + \mu_1\, {EAR_0}^2 \tau_2 - J_0\right) \omega^2 \\ &- \mu_1\, EAR_0\, K_{itt}\end{aligned} \tag{4.43}$$

$$\delta_{tti}(\omega) = -\omega^2 J_0\, \tau_1 - \omega^2 J_0\, \tau_3 - \mu_1\, EAR_0\, \tau_2\, K_{itt} - \mu_1\, EAR_0\, K_{ptt} - \mu_1\, {EAR_0}^2. \tag{4.44}$$

Evaluating Equation (4.42) with $\omega = 0$ gives the condition on K_{itt} that corresponds to the origin on the root space. This relation is given below.

$$K_{itt} = 0 \tag{4.45}$$

To find the boundary in the K_{ptt}-K_{itt} space corresponding to the $j\omega$ axis of the root space, Equation (4.8) is used with

$$\mathbf{F}(\omega) = \mathbf{F_{tt}}(\omega) = \begin{bmatrix} \omega^2 \mu_1 \, EAR_0 \, \tau_2 & -\mu_1 \, EAR_0 \\ -\mu_1 \, EAR_0 & -\mu_1 \, EAR_0 \, \tau_2 \end{bmatrix} \tag{4.46}$$

$$\mathbf{K} = \mathbf{K_{tt}} = \begin{bmatrix} K_{ptt} \\ K_{itt} \end{bmatrix} \tag{4.47}$$

$$\mathbf{B}(\omega) = \mathbf{B_{tt}}(\omega) = \begin{bmatrix} -J_0 \, \omega^4 \tau_3 \, \tau_1 - \left(\mu_1 \, EAR_0{}^2 \tau_2 - J_0\right) \omega^2 \\ \omega^2 J_0 \, \tau_1 + \omega^2 J_0 \, \tau_3 + \mu_1 \, EAR_0{}^2 \end{bmatrix}. \tag{4.48}$$

From Section 4.3.2, the $|\mathbf{F_{tt}}(\omega)|$, given below, can never be zero in a physical system unless $t_r = EA$ which is usually not the case. Thus, $\mathbf{K_{tt}}$ has a unique solution.

$$|\mathbf{F_{tt}}(\omega)| = -\mu_1{}^2 E^2 A^2 R_0{}^2 \left(\omega^2 \tau_2{}^2 + 1\right) \tag{4.49}$$

Solving Equation (4.8) with the above $\mathbf{F_{tt}}(\omega)$, $\mathbf{K_{tt}}$, and $\mathbf{B_{tt}}(\omega)$ yields the stability boundary in the K_{ptt}-K_{itt} space corresponding to the $j\omega$ axis in the root space. This boundary is defined by Equations (4.50) and (4.51).

$$K_{ptt}(\omega) = -\frac{\tau_2 \, \omega^4 J_0 \, \tau_3 \, \tau_1 + \left(J_0 \, \tau_3 - \tau_2 \, J_0 + J_0 \, \tau_1 + \tau_2{}^2 \mu_1 \, EAR_0{}^2\right) \omega^2 + \mu_1 \, EAR_0{}^2}{\mu_1 \, EAR_0 \, \left(\omega^2 \tau_2{}^2 + 1\right)} \tag{4.50}$$

$$K_{itt}(\omega) = \frac{\omega^2 J_0 \, \left(-1 + \left(\tau_3 \, \tau_1 - \tau_2 \, \tau_1 - \tau_2 \, \tau_3\right) \omega^2\right)}{\mu_1 \, EAR_0 \, \left(\omega^2 \tau_2{}^2 + 1\right)} \tag{4.51}$$

Equations (4.45), (4.50), and (4.51) delineate the stability boundaries in the PI controller space for this system and divide the space into regions in which each point produces a PI controller with a fixed number of unstable closed loop poles. Using Table 4.1, these regions were constructed as shown in Fig. 4.10 with their corresponding number of unstable closed loop poles.

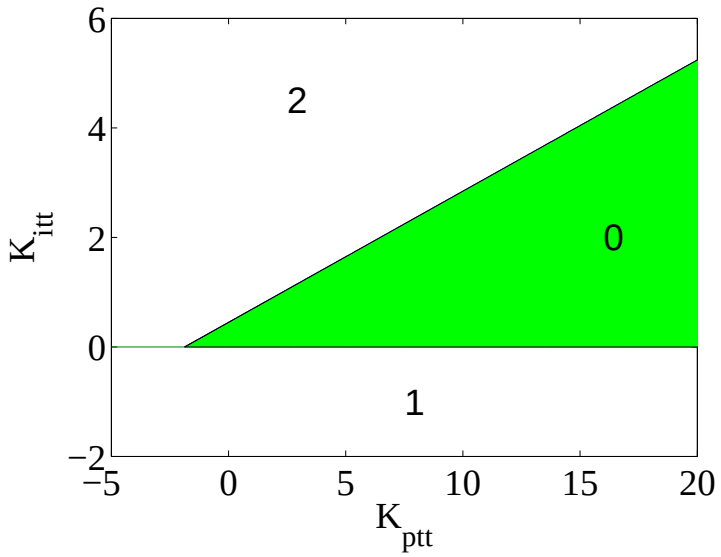

Figure 4.10: Root invariant regions in K_{ptt}-K_{itt} space (the number of unstable poles in each region is indicated)

4.5 Conclusion

This chapter detailed a method to map the $j\omega$ axis in the root space to the PI controller parameter space. This procedure was used to determine the various regions containing stable gains for both a velocity controlled roll with an outer tension loop and a torque controlled unwind roll. From Figs. 4.7 through 4.9 it is observed that the selection of the velocity loop gains can greatly alter the shape and size of the stable region in the tension controller parameter space. If the tension loop controller gains remain constant and the integral gain of the inner velocity loop is changed from being less than $\bar{K_{ivv}}$ to being greater than $\bar{K_{ivv}}$, the once stable system may now

become unstable. Therefore, the selected K_{ivv} should be very different from $\bar{K_{ivv}}$ so that the tension stability regions are not greatly altered when tuning the integral gain of the velocity loop.

It is well known that for web lines that require high performance, a velocity controlled unwind roll is used. This corroborates the findings in this chapter since, although not a direct indication of performance, a comparison of the stability regions for each control strategy shows that there is more flexibility in selecting the gains using velocity control.

CHAPTER 5

Pull Roll 1 and Unwind Accumulator Analysis

5.1 Introduction

This chapter describes the analysis of the current control strategies used to control Pull Roll 1 and the Unwind Accumulator, as well as suggested improvements to enhance the tension control. Pull Roll 1 and the Unwind Accumulator are discussed together because they both use Dancer 1 as feedback for their outer tension loops as discussed in Section 2.5.3. During periods when the accumulator carriage is stationary, the feedback is used solely by Pull Roll 1. Likewise, when Pull Roll 1 is stopped, the accumulator is the only component using Dancer 1 feedback. The feedback is utilized by both Pull Roll 1 and the Unwind Accumulator during three phases: (1) Pull Roll 1 acceleration from zero to line speed, (2) initial portion of the accumulator filling procedure, and (3) final portion of the accumulator filling procedure.

This chapter begins with Section 5.2 which presents the simulation of the system shown in Fig. 5.1 and the associated assumptions. This includes the verification of the system model that compares the results of a simulation of the portion of the CFL under consideration with measured data. Section 5.3 proposes an improvement to the current control strategy: a decrease in the ramp rate of Pull Roll 1 speed reference and a speed profile for Pull Roll 1 with a gradual deceleration to zero speed during the emptying procedure. This chapter closes with a conclusion in Section 5.4.

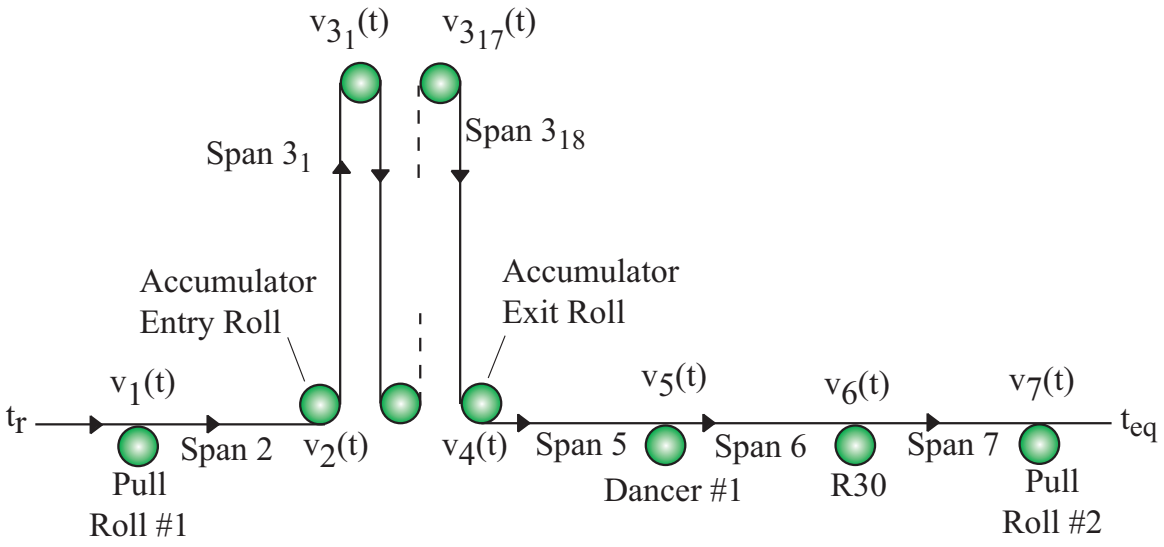

Figure 5.1: Simplified model of the CFL from Pull Roll 1 to Pull Roll 2

5.2 System Simulation Using the Current Control Strategy

The system that was simulated is shown in Fig. 5.1 and includes the elements from Pull Roll 1 to Pull Roll 2. The modeled Unwind Accumulator contained 18 spans; however, the remaining portions of the model were arranged into tension zones. It is assumed that the span prior to Pull Roll 1 and the span downstream of Pull Roll 2 were maintained at constant values. The value of the reference tension in the region upstream of the accumulator is known due to the load cell mentioned in Chapter 2. Hence it was assumed that the tension in the span prior to Pull Roll 1 was well maintained at the reference value. The presence of bearing friction in each roller will cause the equilibrium tension to differ from the reference value. In fact, the equilibrium tension for successive spans with idle rollers will increase. This is verified using Equation (2.3). At equilibrium, the left hand side equals zero, resulting in Equation (5.1) for the tension in the downstream span of an idle roller.

$$t_{i+1,eq} = t_{i,eq} + \tau_f / R_i \tag{5.1}$$

For driven rollers, the torque input from the motor will counteract the friction which enables the equilibrium tension in the spans on either side of the roller to be the same. The only tension sensing element between the accumulator and Pull Roll 2 is Dancer 1, which does not give a numerical value for tension, but rather gives the dancer displacement as a percentage of the maximum stroke. Since the only driven rollers in the system shown in Fig. 5.1 are the first and last rollers, the value of the tension in the spans immediately adjacent to Pull Roll 2 can be calculated using Equation (5.1) starting with the known reference value in the span prior to Pull Roll 1 and successively calculating the equilibrium tension for each subsequent span.

The simulation represents a roll-change scenario which can be described using the Pull Roll 1 speed reference profile shown in Fig. 5.2. At time "A," the material roll is near depletion so Pull Roll 1 begins the stopping procedure. In the CFL, the reference value is not immediately set to zero; the ramp for Pull Roll 1 speed reference will continue to work for 0.5 seconds in order to allow the accumulator carriage to accelerate. After this delay, the reference is set to zero. However, modeling this exact sequence would produce inaccurate results since the simulation would drive the Pull Roll 1 speed to zero at a rate that is not physically possible. Additionally, large overshoots in the velocity would occur as the simulated velocity controller attempted to correct for this sudden change in reference. Therefore, in the simulation, an S-curve was used to facilitate this deceleration in a manner that was consistent with data collected from the CFL. However, this step change in reference was still used in the simulated Unwind Accumulator algorithm; by placing limits on the rate of change in the speed reference, results were obtained that were consistent with measured data from the CFL. This procedure was not used with Pull Roll 1 since the overshoots in speed still persisted even with limiting the rate of reference change. At "B," Pull Roll 1 is completely stopped and the accumulator is at constant velocity, using Dancer 1 feedback in the outer tension loop. This continues until time "C" where the new roll

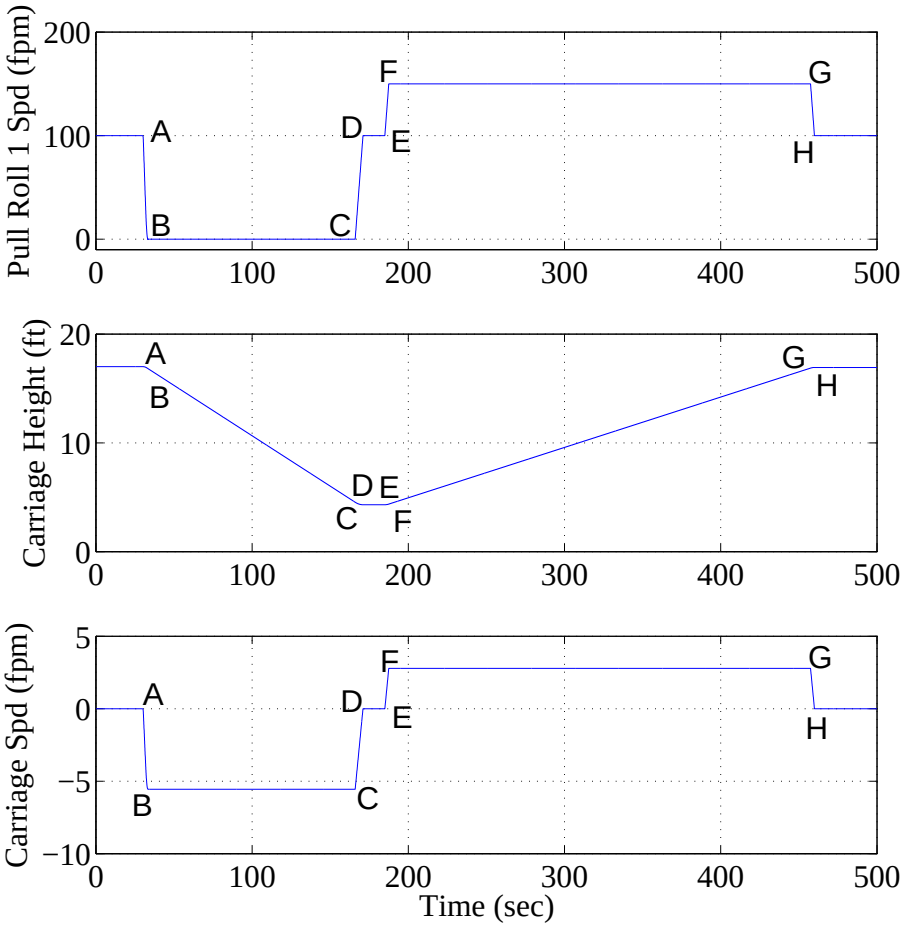

Figure 5.2: Reference profiles for Pull Roll 1 speed and Unwind Accumulator carriage height and velocity (Model Simulation)

has been spliced onto the previous one and Pull Roll 1 begins its acceleration up to line speed, causing the carriage to decelerate. At "D," Pull Roll 1 has reached line speed and the carriage has come to rest at its lowest height. An operator begins the accumulator filling process at "E." The speed reference for Pull Roll 1 is ramped to 50 fpm greater than line speed, causing the accumulator carriage to rise. "F" is the time when the ramping is complete and the nominal speed reference for Pull Roll 1 (and hence the accumulator) is constant with correction provided by the dancer. During this time, the accumulator is only under speed control as discussed in Subsection

2.5.3. The carriage reaches the limit switch at "G" which decelerates the accumulator carriage to zero velocity and ramps the Pull Roll 1 reference speed down to line speed. At "H" the accumulator processes are completed and the system is returned to the nominal condition.

5.2.1 Span Parameters and Initial Conditions

The web properties from Table 3.1 were utilized along with the span parameters from Table 5.1. The controller gains used in the simulation are shown in Table 5.2. Note that Rollers 2 through 6 are idlers and thus have lower inertias than J_1 and J_7 whose respective motor inertias are reflected to the roller side. Conversely, J_c is reflected to the accumulator motor side, resulting in a smaller value. All of the PID gains listed are those used in the actual system except for the speed gains for Pull Roll 1 which were altered to account for the un-modeled dynamics that were causing the simulated Pull Roll 1 speed to differ from data collected from the CFL during the deceleration phase at time "A." The mass of the accumulator carriage was assumed to be 1.5 times greater than the total mass of all of the rollers contained in the carriage. This accounts for the carriage structure since specific dimensions are not available. The friction value was selected based on the results of the friction torque test described in Subsection 2.4.2.

The initial conditions for the simulation are shown in Table 5.3. The accumulator is initially at rest at its maximum height of 17 ft, and the initial dancer position is vertical. The initial conditions of the tension, velocity, and strain were set so that the system was initially at equilibrium. The initial span tensions were calculated using Equation (5.1). The initial roller speeds were calculated in a similar fashion using Equation (5.2) which was derived from the strain equation for each respective web line element.

$$v_{i,eq} = v_{i-1,eq}\left(\frac{1-\varepsilon_{i-1,eq}}{1-\varepsilon_{i,eq}}\right) \tag{5.2}$$

Table 5.1: Parameters Used in the Simulation of the System Shown in Fig. 5.1

Variable	Value Used in Simulation	Units
F	514	lbf
J_c	0.0832	slug·ft^2
J_j	4.51	slug·ft^2
J_1	36.68	slug·ft^2
J_7	49.64	slug·ft^2
L_2	2.015	ft
L_{5n}	6.298	ft
L_{6n}	1.612	ft
L_7	26.4	ft
m_{gc}	363.88	slug
N_{Ac}	18	None
n_c	6.1628×10^{-4}	ft
n_1	33.04	None
n_7	37.99	None
R_c	5.25	in
R_i	5.25	in
R_7	6	in
t_r	96	lbf
v_{ls}	100	fpm
$x_{t,max}$	6	in
τ_f	0.293	ft·lbf
i=1,...,6		
j=2,...,6		

Table 5.2: Controller Gains Used in the Simulation of the System Shown in Fig. 5.1

Variable	Value Used in Simulation	Units
$K_{d,D1}$	10	s
$K_{i,AC}$	3.2	s^{-1}
$K_{i,D1}$	0.01	s^{-1}
$K_{i,PR1}$	5	s^{-1}
$K_{i,PR2}$	2.7	s^{-1}
$K_{p,AC}$	2.6	None
$K_{p,D1}$	5	None
$K_{p,PR1}$	4	None
$K_{p,PR2}$	2.2	None

Table 5.3: Initial Conditions Used in the Simulation of the System Shown in Fig. 5.1

Variable	Initial Condition	Units
v_c	0	fpm
x_c	17	ft
x_t	3	in
$\dot{x}_t$	0	ft/s
v_{1i}	100	fpm
t_{1i}	96	lbf
v_{7i}	100.02	fpm
t_{7i}	110.06	lbf

Since the accumulator and dancer are initially at rest, Equation (5.2) can be obtained for the spans within these components using Equations (2.10) and (2.30), respectively. Similarly, the initial strains for each span are calculated from Equation (2.7) and are given by $\varepsilon_{i,eq} = t_{i,eq}/(AE)$.

5.2.2 Simulation Results

A simulation was conducted using the pertinent equations from Section 2.3 and the control strategies for Pull Roll 1, the Unwind Accumulator, and Pull Roll 2 discussed in Sections 2.5.3 and 2.5.4. The results of the simulation are shown in Figs. 5.3 through 5.5.

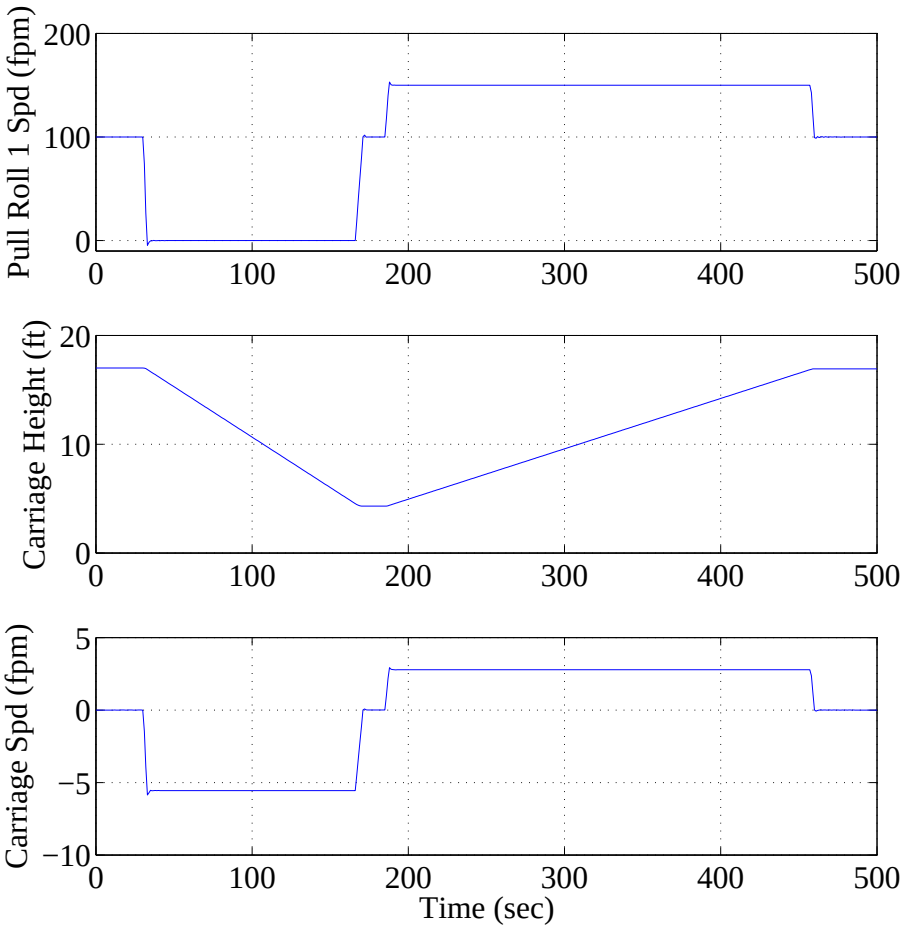

Figure 5.3: Pull Roll 1 speed and Unwind Accumulator carriage height and velocity (Model Simulation)

Comparing Figs. 5.2 and 5.3, Pull Roll 1 and the Unwind Accumulator followed the general trends found in their respective expected profiles. Figure 5.6 shows the actual and reference speed for the accumulator carriage during the initial stages of

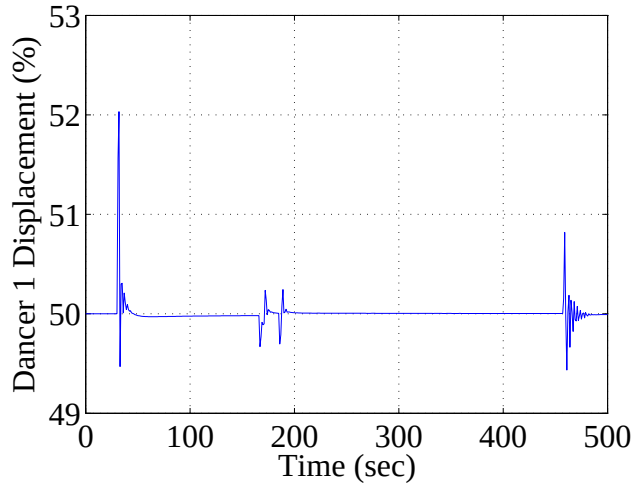

Figure 5.4: Dancer 1 position in percentage of maximum stroke (Model Simulation)

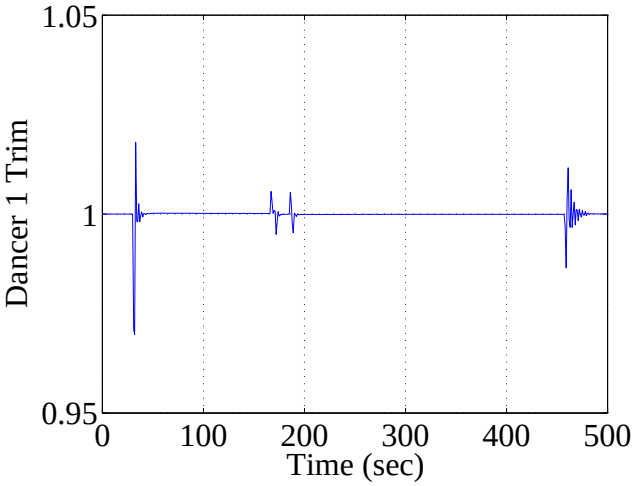

Figure 5.5: Dancer 1 Trim scaling factor (Model Simulation)

the emptying process. As seen from the plot, the speed follows the reference well until the speed reference steps to approximately -5.5 fpm. Due to the acceleration limiter within the carriage motor, the carriage decelerates at a fixed rate with its inner velocity loop providing corrections. Note that during this time, the dancer feedback is altering $v_{cr}(t)$ yet the carriage is not able to react to these corrections due to the acceleration limiter. Thus, the entire system is only under speed control until the actual carriage speed nears the reference speed, an event which does not

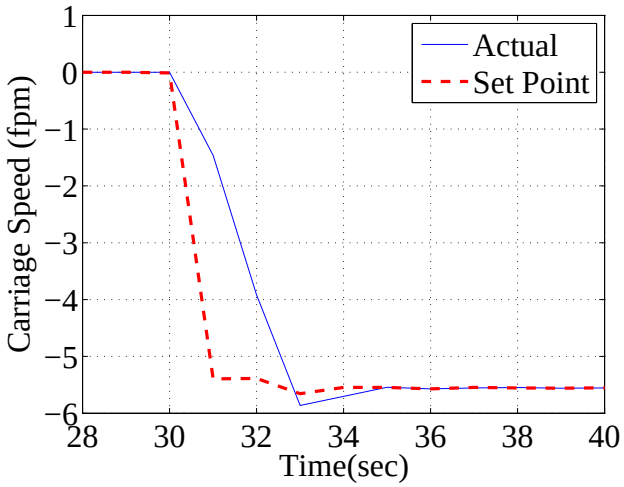

Figure 5.6: Accumulator carriage speed during initial portion of the emptying process (Model Simulation)

occur for several seconds. As seen later, this causes large fluctuations in the Dancer 1 position. When Pull Roll 1 reaches zero speed, the accumulator carriage is near its speed reference value and thus the outer tension control loop is reestablished. The carriage begins descending at a constant speed with corrections being provided by the dancer as given in Equation (2.70). The minimum height achieved by the accumulator carriage is 4.3 ft. When Pull Roll 1 initializes its acceleration back to line speed, the increase in $v_{1r}(t)$ causes a corresponding decrease in $v_{cr}(t)$. This synchronization between these two rates ensures that the rest of the CFL is provided with material at the proper speed without producing large tension fluctuations. After Pull Roll 1 accelerates back to line speed, the carriage is seen to be static at its minimum height, as expected, and it remains at this position until the filling procedure. This is because, at this phase, the Pull Roll 1 speed reference has been ramped to $v_{ls}d_x(t)$, rendering Equation (2.70) to be zero. As Pull Roll 1 accelerates to 50 fpm faster than line speed, the carriage also accelerates, increasing $x_c(t)$ as the filling process begins. At the end of this procedure (the time corresponding to "G" from Fig. 5.2), Pull Roll 1 ramps back to line speed, reducing $v_{cr}(t)$ as the accumulator carriage decelerates to

its original position at its maximum height.

Figures 5.4 and 5.5 show the Dancer 1 position as a percentage of maximum stroke and Dancer 1 Trim, respectively. Comparing these plots with Fig. 5.2 indicates that at every speed change of Pull Roll 1 and Unwind Accumulator, tension fluctuations are produced that cause dancer movement. Just after point "A," the accumulator carriage begins its descent which initially causes a tension decrease due to the shortening of the web spans. The constant force, F, will thus cause Dancer 1 to extend due to the decrease in tension. This motion causes a decrease in Dancer 1 Trim which attempts to slow the descent of the accumulator. However, since the acceleration of the accumulator carriage motor is limited, the dancer movement does not have any effect on the control. In fact, for the following several seconds, the dancer motion is a result of the dynamics of the system under pure velocity control. Once the accumulator carriage speed nears its reference, the dancer feedback is able to adjust this reference value to correct the carriage speed which reduces the tension error. When Pull Roll 1 accelerates back to line speed, the carriage decelerates according to Equation (2.70). This deceleration causes the tension in the latter spans of the accumulator to increase which contracts Dancer 1 since the tensions in Spans 5 and 6 are greater than their equilibrium values. The controller uses this position measurement to increase the speed of both Pull Roll 1 and the Unwind Accumulator by increasing Dancer 1 Trim. After this initial motion, the system oscillates as the controller reduces the tension error. This same trend is seen when Pull Roll 1 accelerates to fill the accumulator. When the filling process is completed and the speed reference for Pull Roll 1 is changed from the filling speed, the accumulator carriage decelerates, causing the tensions in the latter spans to decrease. As described above, this causes the dancer to extend. The controller reacts by decreasing Dancer 1 Trim which slows the speed references for Pull Roll 1 and the accumulator carriage, bringing the tension back towards the reference value. The dancer continues to oscillate as the tension error

reduces to zero.

The above discussion illustrates that the model simulation exhibits the expected behavior from the system shown in Fig. 5.1 during a roll change scenario. To further verify the model, the results will be compared with data collected from the CFL. This task is performed in the subsequent section.

5.2.3 Model Verification Using Measured Data from the CFL

This section presents data collected from the CFL and compares it with the results of the model simulation from Section 5.2. The measured data is shown in Figs. 5.7 through 5.9.

Figure 5.7 shows the Pull Roll 1 speed along with the Unwind Accumulator carriage speed and height. Comparing this plot with Fig. 5.3 illustrates that the measured data followed the same trends as those seen in the model simulation. The Pull Roll 1 speed for the measured data is comparable to the results obtained using the model simulation. The speeds and acceleration rates obtained were similar as well. However, the measured data exhibited more overshoot than the simulation. This can be attributed to un-modeled dynamics present in the CFL that are not accounted for in the simulation. Another characteristic of the Pull Roll 1 data that is present in the measured data and not in the simulated data is the speed error during the accumulator filling process. As will be seen later, the controller attempts to correct for this by decreasing Dancer 1 Trim, but the speed does not decrease. This trend is seen in all of the data collected from the CFL and the cause for this phenomenon is discussed in the future work section in Chapter 6. Note that the measured carriage height from Fig. 5.7 achieved similar values as those seen in the model simulation, with maximum and minimum values of approximately 17 ft and 4.2 ft, respectively. Additionally, the measured data shows the carriage attaining a speed of approximately -6 fpm during the emptying phase and 3 fpm during the filling phase, both

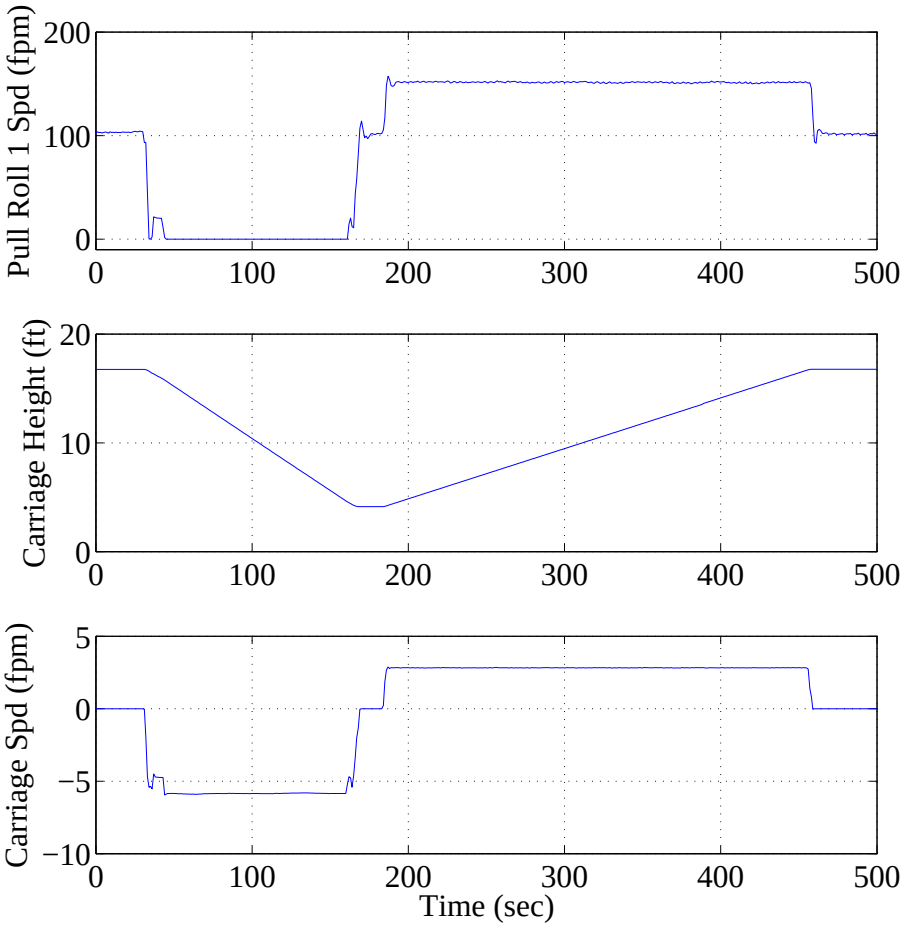

Figure 5.7: Pull Roll 1 speed and Unwind Accumulator carriage height and velocity

of which match the simulation. Figure 5.10 shows the accumulator carriage speed and its corresponding reference during the initial portions of the emptying phase. Comparing this plot with Fig. 5.6 illustrates that both the measured and simulated data display comparable carriage acceleration limitations due to the step change in the carriage reference speed. However, one distinction between these data is seen just after the initialization of the emptying process. In the measured data, Pull Roll 1 speed is increased to 20 fpm for approximately 8 seconds. This increase in speed is used to longitudinally position the web material to a convenient location for splicing and is referred to as "jogging." This process was not modeled in the simulation due to

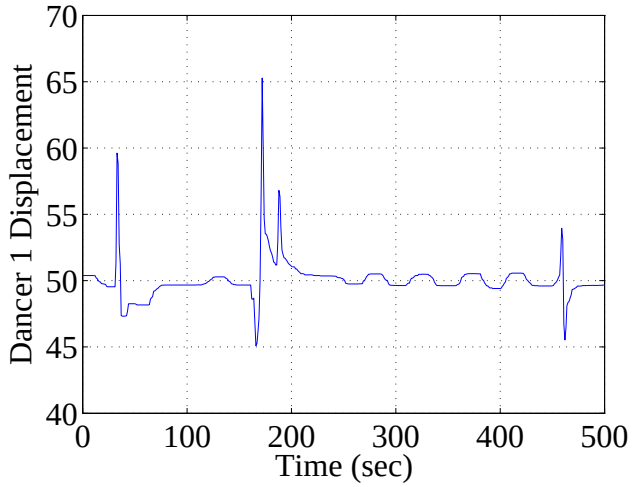

Figure 5.8: Dancer 1 position in percentage of maximum stroke

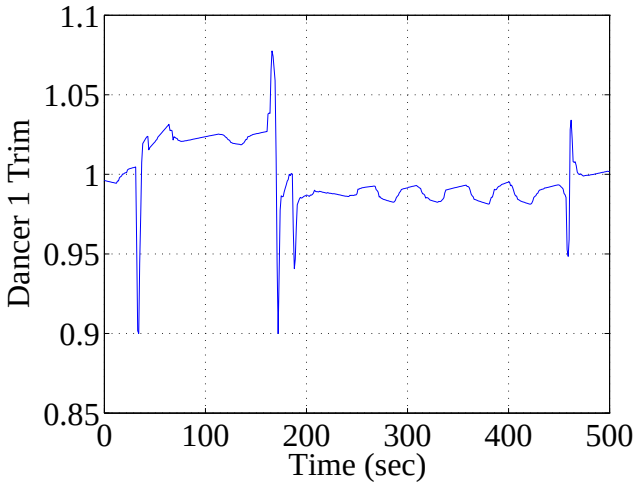

Figure 5.9: Dancer 1 Trim scaling factor

its inconsistency; the duration and occurrence of the jog are both manually controlled by an operator. However, despite the discrepancies seen with the Pull Roll 1 speed overshoots and the absence of the jogging process from the simulation, the measured Pull Roll 1 and Unwind Accumulator data presented above sufficiently match the corresponding model simulation data.

Figures 5.8 and 5.9 display the measured Dancer 1 position as a percentage of maximum stroke and Dancer 1 Trim, respectively. Comparing these results with Figs.

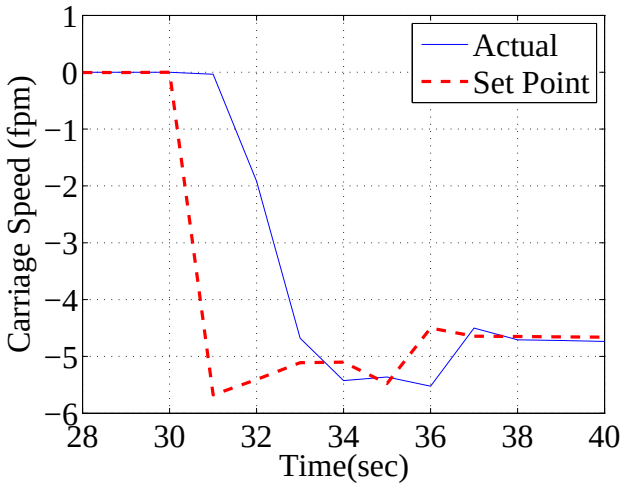

Figure 5.10: Accumulator carriage speed during initial portion of the emptying process

5.4 and 5.5 shows that the measured data follows similar trends seen in the model simulation with only a few exceptions. The simulated dancer movement mimics the motion measured from the Dancer 1 on the CFL during each of the Pull Roll 1 speed transitions. The Dancer 1 Trim behaves likewise. However, the magnitudes seen in the measured data are greater than those present in the simulation for both variables. Additionally, the simulated data for both variables oscillate more than their measured counterparts during accumulator phase transitions. The reason for this is that more damping is present in the physical system, thus reducing the amount of oscillations. Conversely, during non-transitional periods, the simulated data shows the Dancer 1 position and Dancer 1 Trim as being constant whereas the measured data oscillates due to the un-modeled dynamics in the CFL. Another phenomenon present in the measured data that is not shown in the simulation is the errors in the Dancer 1 position and Dancer 1 Trim during the filling of the accumulator, both of which are due to the Pull Roll 1 speed feedback not converging to its reference value. Since the Pull Roll 1 speed is larger than its reference, the tension decreases, causing the dancer to extend. To compensate, the Dancer 1 Trim decreases in an attempt to decrease

the Pull Roll 1 speed. The investigation of this problem is included in the future work section of Chapter 6. However, these differences between the measured and simulated data for the Dancer 1 position and Dancer 1 Trim are minor. Therefore, the data presented in Figs. 5.8 and 5.9 verify the model simulation.

5.2.4 Summary

The model simulation exhibited many of the trends seen in the measured data. The simulated accumulator carriage attained similar speeds during the emptying and filling processes that were witnessed in the CFL. Additionally, the simulated carriage position achieved values comparable to those seen in the measured data. The model simulation was able to sufficiently mimic the motion of Dancer 1 as well. During the phase transitions of the accumulator, the model showed dancer movement that was matched by the measured data.

However, there were aspects that the model did not accurately predict. One such trend was the overshoot exhibited by Pull Roll 1 during accumulator phase changes. The measured data showed significant overshoot whereas the model did not. Additionally, the model did not manifest the Pull Roll 1 speed offset present in the measured data during the accumulator filling process. The model was also unable to match the magnitudes seen in the measured Dancer 1 displacement and Dancer 1 Trim. Furthermore, the model had more oscillations during accumulator phase transitions whereas during the non-transitional segments, it did not exhibit the oscillations that were displayed in the measured data. However, despite these differences, the model simulation sufficiently represents the CFL and can be used to derive improvements to the current control strategy.

5.3 Improvement 1

The above results show that the displacements of Dancer 1 were the largest just after a change in the speed reference for Pull Roll 1 during transitions in accumulator phases. As discussed in Subsection 5.2.2, the sudden change in the respective speeds of these two components will produce variations in tension, resulting in dancer movement. Another consequence of the change in speed reference is that, in an attempt to reach their respective reference speeds, Pull Roll 1 and the accumulator carriage will overshoot their reference values. This causes a speed mismatch between these two components which generates tension fluctuations that create dancer movement. For example, during the initial stages of the emptying process, if the accumulator carriage moves downward at a rate such that web is released into the CFL faster than Pull Roll 1 is supplying web to the accumulator, the tension will rise, resulting in dancer movement. Conversely, if Pull Roll 1 supplies web in the accumulator faster than the accumulator is releasing web, the tension will decrease, also producing dancer movement.

The above discussion implies that the larger the ramp rates of the speed references for Pull Roll 1 and the accumulator, the greater the movement of Dancer 1. A more aggressive acceleration profile will magnify the induced tension fluctuations, creating increased dancer displacement. Additionally, the faster change in the reference will result in increased controller effort as the controller attempts to reduce the speed error. This will produce larger overshoots, causing a greater speed mismatch between Pull Roll 1 and the accumulator carriage, and thus creating larger dancer movement. Therefore, reducing the ramp rates of these two components will result in decreased movement of Dancer 1.

The improvement (Improvement 1) to the current control strategy includes two changes: (1) reduce the ramp rate for Pull Roll 1 speed reference changes and (2) gradually reduce the speed reference of Pull Roll 1 during the initialization of the

emptying procedure. The first component of Improvement 1 will reduce the tension fluctuations due to the sudden change in Pull Roll 1 and accumulator carriage speeds since the changes in speed will be smaller. This will additionally result in lower overshoot amplitudes since the controllers will make smaller adjustments, thus reducing the speed mismatches between Pull Roll 1 and the accumulator and ultimately resulting in smaller dancer movements. In the current control strategy, there is a speed mismatch between Pull Roll 1 and the accumulator during the initial stages of the emptying procedure. 0.5 seconds after the start of the emptying process, Pull Roll 1 decelerates at a rate independent of the accumulator. Additionally, the step decrease in the accumulator speed reference that occurs at this time causes the carriage to accelerate at the limiting rate of its motor instead of a gentler pace that would allow for corrections due to dancer feedback. The second aspect of Improvement 1 will resolve these issues by allowing Pull Roll 1 and the Unwind Accumulator to decelerate and accelerate, respectively, at a controlled rate. This will reduce the speed mismatch between these two components. Additionally, this will decrease the amount of overshoot in the accumulator carriage speed at times "A" and "B" from Fig. 5.2 since the changes in the acceleration rates will be smaller. Note that as Pull Roll 1 is ramped to zero speed, it will only be under speed control and the Unwind Accumulator will regulate the tension. The modifications of Improvement 1 will reduce the dancer movement which indicates increased tension regulation performance.

5.3.1 Model Simulation Using Improvement 1

The speed reference in the current control strategy is calculated as an integer quantity that represents the reference multiplied by 10. During each scan of the RSLogix file (which occurs every 10 msec), the ramp either adds or subtracts two from this integer value (an increase/decrease of 0.2 fpm) according to the reference's need to increase or decrease. Thus, in order for Improvement 1 to be practical and readily applied

into the current RSLogix routine, the new ramp rate is selected to be half of the current one (i.e., the new ramp rate is selected to be 10 fpm/s where each scan of the RSLogix file alters the speed reference integer value by one).

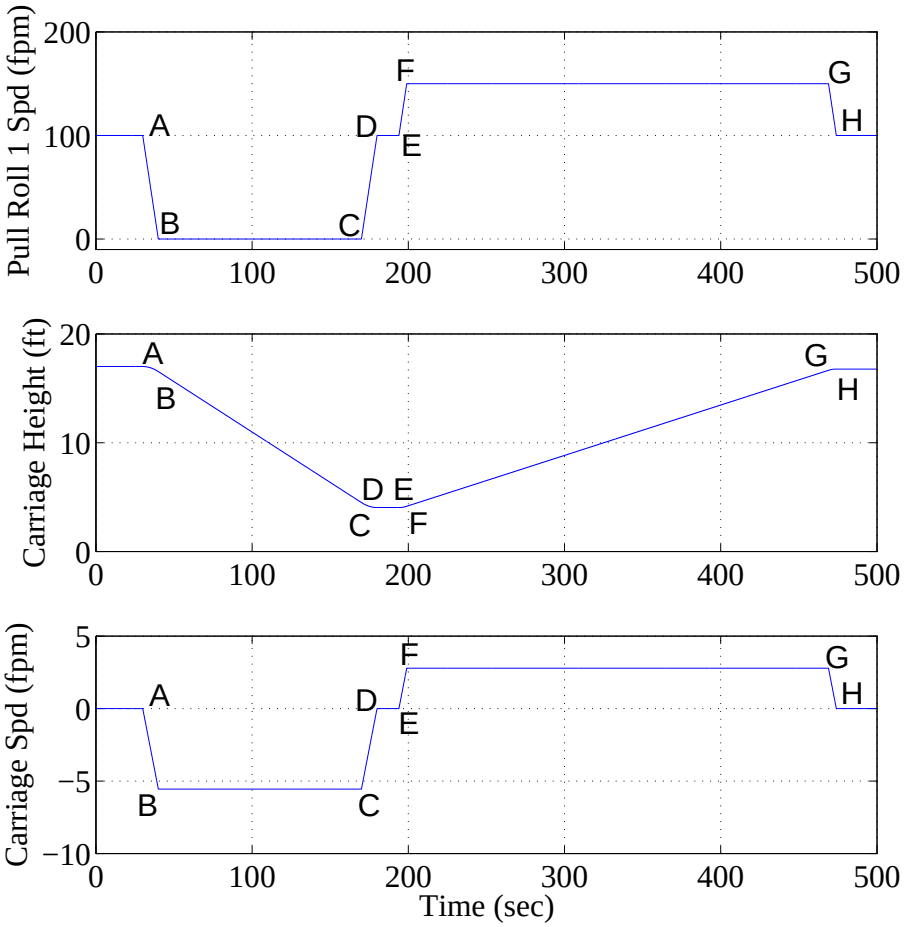

Figure 5.11: Reference profiles for Pull Roll 1 speed and Unwind Accumulator carriage height and velocity using Improvement 1 (Model Simulation)

A simulation was conducted using Improvement 1 with the reference profiles for Pull Roll 1 speed, the Unwind Accumulator carriage height, and the carriage speed displayed in Fig. 5.11. This plot shows the same accumulator phases as in Fig. 5.2 but includes the new ramp rate and the new reference speed profile for Pull Roll 1 during the initial emptying procedure. The parameters and initial conditions from

Tables 5.1 and 5.3 were also utilized. The results of the simulation are shown in Figs. 5.12 through 5.14.

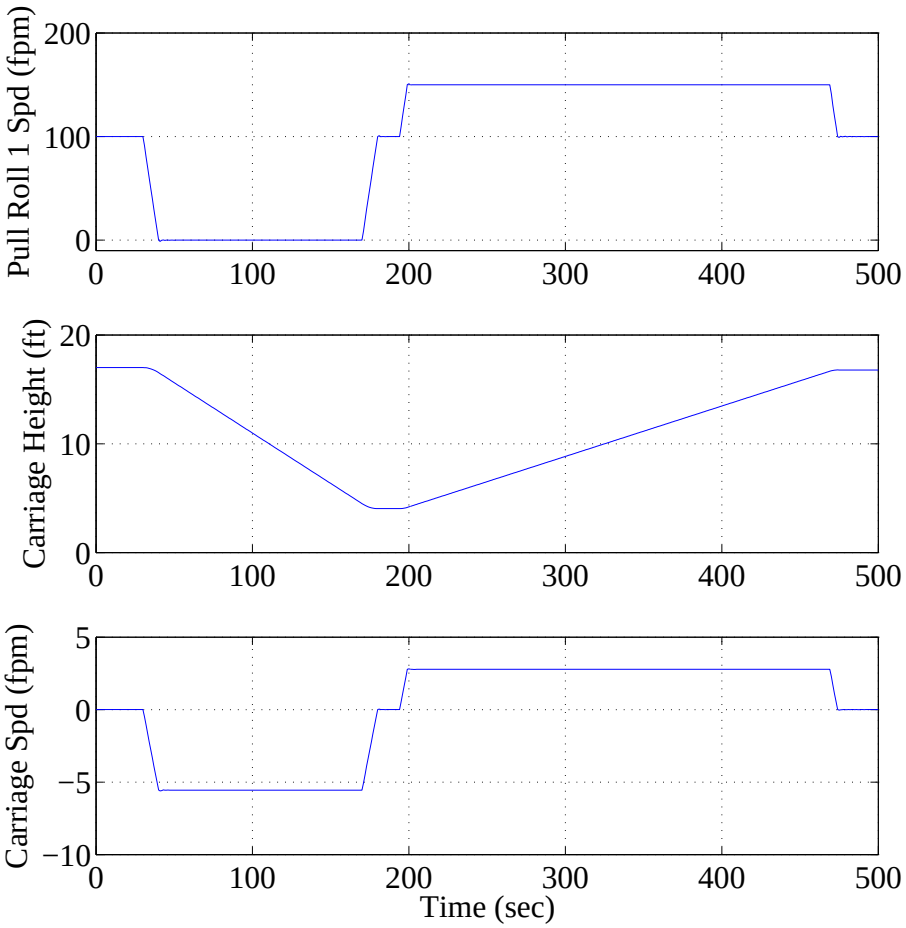

Figure 5.12: Pull Roll 1 speed and Unwind Accumulator carriage height and velocity using Improvement 1 (Model Simulation)

Figure 5.12 shows the Pull Roll 1 speed and the Unwind Accumulator carriage height and speed. Note that Improvement 1 was successful in providing gentle and controlled speed changes for Pull Roll 1 and the accumulator carriage between times "A" and "B." Because the speed reference for Pull Roll 1 is not stepped to zero and the ramp rate is smaller, the deceleration and acceleration limits for Pull Roll 1 and the accumulator, respectively, were not exceeded, reducing the speed mismatch seen

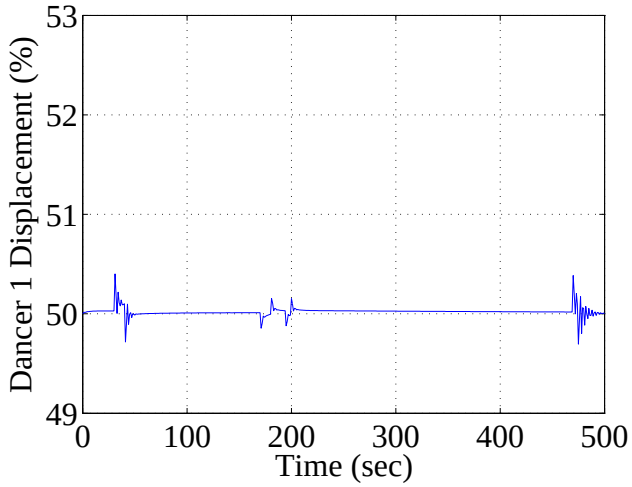

Figure 5.13: Dancer 1 position in percentage of maximum stroke using Improvement 1 (Model Simulation)

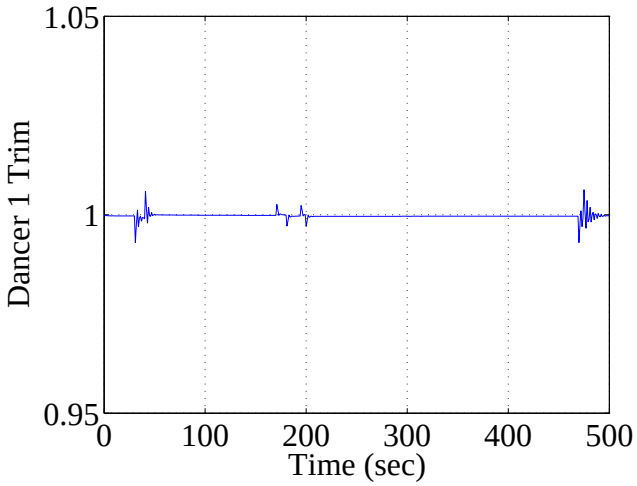

Figure 5.14: Dancer 1 Trim scaling factor using Improvement 1 (Model Simulation)

in the current control strategy. Additionally note that the time between "C" and "D" (denoted "CD"), "EF", and "GH" were extended due to the slower ramp rate. Moreover, the overshoots in the speeds for both Pull Roll 1 and the accumulator carriage were reduced at each of the accumulator phase transitions due to the decreased ramp rate. The accumulator carriage height also remained reasonable throughout the simulation. The minimum height of the carriage was approximately 4.0 ft which is

less than four inches below the minimum value for the current control strategy and within the realm of practicality.

Figures 5.13 and 5.14 show the dancer displacement and Dancer 1 Trim, respectively. Comparing these plots with Figs. 5.4 and 5.5 illustrates that Improvement 1 was successful in reducing the amount of dancer displacement. Therefore, implementing a controller with the Improvement 1 changes increases the tension regulation performance.

However, there are a few disadvantages to the use of Improvement 1. The first problem is that currently, during a roll change procedure, Pull Roll 1 is stopped by an operator when the material roll is depleted and the web is dragging along the floor. With Improvement 1, the "AB" time is longer and may not allow this stopping procedure as the end of the material may be drawn beyond its desired location. Additionally, the increased durations for "AB" and "CD" will reduce the maximum time allowable to perform the splice (time "BC"). The simulation conducted above used a splice time of 130 seconds which is consistent with the time generally required to conduct this operation. However, this time reduction should be considered before implementing Improvement 1 so the accumulator carriage does not reach its minimum limit.

5.3.2 Summary

Improvement 1 used a reduced ramp rate for Pull Roll 1 speed reference changes as well as implemented a procedure where this reference value was gradually reduced to zero during the initial stages of the emptying process. A simulation was conducted and the results showed a decrease in the movement of Dancer 1 which indicates improvement in the tension regulation. Although there are a few minor disadvantages to Improvement 1, it provides a sufficient increase in performance over the current control strategy.

5.4 Conclusion

This chapter presented the analysis for the section of the CFL that contains the elements from Pull Roll 1 to Pull Roll 2. The model simulation using the current control strategy was constructed and the corresponding results were shown for a roll change scenario. The corresponding measured data were compared with these results to verify the model. Subsequently, an improvement to the current control strategy was derived which decreased the ramp rate of Pull Roll 1 and allowed its speed to gradually decrease at the initiation of the emptying procedure. The results of the roll change simulation using this improvement showed increased performance as it reduced the amount of Dancer 1 movement that is seen with the existing strategy.

CHAPTER 6

Conclusions and Future Work

6.1 Conclusions

In the web processing industry, accurate control of web tension is essential to the manufacture of high quality products from the web material. This thesis focused on the analysis and improvement of the existing control strategies for a Coating and Fusion Line (CFL) that produces finished flooring material in order to improve web tension performance. The unwind section of the CFL was separated into two portions: the first portion contained the elements from the Unwind Roll to Pull Roll 1 and the second portion contained the components from Pull Roll 1 to Pull Roll 2. For each section, models were developed that described the relevant dynamics and the current control strategies. These models were used to conduct relevant simulations in each section and the results were verified by comparing the results with data measured from the actual CFL. Improvements to the existing strategies were also developed. New strategies for the control of the Unwind Roll were implemented on the CFL, and they successfully increased the tension performance. The investigation of the Unwind Roll motivated the comparative analysis of a torque and a velocity controlled unwind roll based on the stability regions in the parameter space. A chapter by chapter summary is provided below.

Chapter 2 presented the necessary information to develop a model for the unwind section of the CFL. First, the web velocity dynamics were presented for the Unwind Roll, idle/driven rollers adjacent to spans with fixed length, rollers within the accumulator, and the dancer roller. The web tension and strain dynamics associated

with fixed-length spans, spans within the accumulator, and the spans adjacent to the dancer were also derived, as well as the dynamics of the accumulator carriage and dancer mechanism. Subsequently, the viscoelastic parameters were determined using a curve fitting method with tensile test data. Additionally, the bearing friction torque for the rollers was identified. Finally, the control strategies for the Unwind Roll, Pull Roll 1, Unwind Accumulator, and Pull Roll 2 were presented in this chapter.

In Chapter 3, analysis of the section of the CFL from the Unwind Roll to Pull Roll 1 is discussed. The first task was the development of the model simulation and the validation of this model with data collected from the CFL. To correct some of the deficiencies with the existing control strategy, three separate strategies, named Strategies 1, 2, and 3, were discussed. Each strategy utilized a faster sampling time and tension measurement and controller output resolution. In addition to these modifications, Strategy 2 employed time-varying PI gains that decreased with the Unwind Roll radius. To remove the controller load placed on the integrator in Strategies 1 and 2, Strategy 3 used a PI to provide corrections for feed-forward control. Simulations showed that each of the modified strategies provided improved tension performance.

Strategy 1, Strategy 2, and a modified version of Strategy 2 (called Strategy 2a) were then implemented on the CFL during the manufacture of actual web product. The first and third strategies showed an improvement over the existing strategy. Strategy 2a, which exactly mimics the existing strategy except with varying PI gains, was developed in response to the negative results obtained using Strategy 2. The reason for the adverse performance of Strategy 2 was that the physical configuration of the brake was altered, effectively re-tuning the gains. As the gains for Strategy 2 were based on those used in Strategy 1, this reconfiguration caused unfavorable tension results. Through this experimentation process, it was determined that it is not possible to develop a controller that produces substantial improvements for each brake configuration. In spite of this, two recommendations were given. If the brakes

remain as they are with nonuniform and inconsistent performances, Strategy 2a is the recommended controller since it produced better tension performance than the existing control strategy for multiple brake configurations. However, if the brakes can be modified to have uniform and consistent performances, then Strategy 2 is the recommended controller.

Chapter 4 developed an approach to compare torque and velocity controlled unwind rolls. The stability boundary in the root space was mapped to regions within the controller parameter space via the characteristic equation of the closed loop tension dynamics. For the velocity controlled roll, this was a two step procedure where the stability regions in the velocity controller parameter space were determined and then those for the outer tension loop controller, which are a function of the velocity loop gains, were created. A comparison of the stability regions for the two unwind roll control strategies showed that there is more flexibility in selecting the gains when using velocity control than torque control. Additionally, the size and shape of the tension stability regions greatly depend on the selection of the gains of the velocity loop.

The analysis of the section of the CFL from Pull Roll 1 to Pull Roll 2 was conducted in Chapter 5. A model of this system was created and then verified by comparing the results of the model simulation to data measured from the CFL. One improvement (called Improvement 1) was created in which the ramp rate for Pull Roll 1 speed reference was reduced. Additionally, the emptying procedure was altered so that, instead of a step, a ramp was utilized to reduce the speed reference for Pull Roll 1 to zero. Simulations showed that Improvement 1 reduced the amount of Dancer 1 displacement which was the metric used to judge the tension regulation performance.

6.2 Future Work

In this thesis, a model for the brake was used in which the torque applied to the Unwind Roll was a scalar multiple of the braking pressure. Another relationship should be developed in order to increase the accuracy of the model. A possible improvement would be to develop a stick-slip model for the dynamics relating the force applied to the Unwind Roll by the braking pressure to the corresponding applied friction torque. Additionally, the model should be altered to include a velocity disturbance at Pull Roll 1 and to incorporate the idle rollers that are present between the Unwind Roll and Pull Roll 1. Each of these alterations should result in a more accurate model which will allow for the development of better improvements to the existing control strategy.

It was shown in this thesis that the physical configurations for Brakes 1 and 2 can differ significantly, resulting in inconsistent controller and tension regulation performance. This inconsistency makes it difficult to derive a controller that improves the tension regulation for all brake configurations. The causes of these variations in the brake configuration should be investigated. This would include a study of both the pneumatic device that supplies the pressure to the brake pucks and the friction mechanism that slows the material roll to provide further insight on the brake configuration. In the future, it would be beneficial to modify both brakes so that they have uniform performances. Subsequently, controllers could be developed that would improve the regulation of tension beyond what was achieved in this report.

Experiments should also be conducted using a different material. In this report, all three experiments were executed utilizing the same web material. The performances of Strategies 1 and 2a should be verified with different web materials. Additionally, Strategy 2 should be implemented with re-tuned gains that allow adequate results for multiple brake configurations. The results of this experiment should be compared with the results obtained used Strategy 2a to determine the effectiveness of reducing

the sampling time and increasing the resolution of the control variable.

This thesis compared a torque controlled unwind roll with a velocity controlled unwind roll on the basis of stability regions within their respective controller parameter spaces. These regions should be re-evaluated for various values of system parameters such as unwind roll radius, web reference speed, and web material. This task will provide insight into how sensitive the closed loop stabilities of these two control strategies are with regard to system parameters. Future work should also concentrate on comparing these two methods of control based on tension regulation performance. Additionally, experimental verification of both the stability and performance results would further support this analysis. The comparison of these two strategies is beneficial since it will reveal which strategy regulates tension better.

An improvement to the existing control strategy for Pull Roll 1 was developed in this thesis. This new strategy should be implemented onto the CFL to verify its performance. This task would require creating an algorithm that would automatically decelerate Pull Roll 1 to zero speed during the emptying procedure so that the web stops at a location convenient for splicing, an operation which is currently done manually. Additionally, the measured CFL data presented in this report showed dancer oscillations during the constant speed portions of the accumulator phases and Pull Roll 1 speed errors during the filling procedure. The causes of these phenomena should be investigated and possible solutions to eliminate these problems should be developed.

BIBLIOGRAPHY

[1] P. R. Pagilla, N. B. Siraskar, and R. V. Dwivedula, "Decentralized control of web processing lines," *IEEE Transactions on Control Systems Technology*, vol. 15, January 2007.

[2] P. R. Pagilla, I. Singh, and R. V. Dwivedula, "A study on control of accumulators in web processing lines," *Journal of Dynamic Systems, Measurement, and Control*, vol. 126, pp. 453–461, September 2004.

[3] P. R. Pagilla, E. O. King, L. H. Dreinhoefer, and S. S. Garimella, "Robust observer-based control of an aluminum strip processing line," *IEEE Transactions on Industry Applications*, vol. 36, May 2000.

[4] D. H. Carlson, P. R. Pagilla, and M. D. Weaver, "Modeling and control of web velocity and tension: an industry/university perspective on issues of importance," *Proceedings of the Tenth International Conference on Web Handling*, 2009.

[5] Rockwell Automation, *Logix5000^{TM} Controllers Common Procedures, Publication 1756-PM001H-EN-P*, June 2005.

[6] Rockwell Automation, *Logix5000^{TM} Controllers General Instructions, Publication 1756-RM003H-EN-P*, May 2005.

[7] U. M. Sridhar, R. R. Rhinehart, and S. V. Madihally, "Pseudo-component viscoelastic model of soft tissues," November 2010. presented at 2010 AIChE Annual Meeting, Salt Lake City, UT, USA.

[8] American Society for Testing and Materials, *Standard Test Methods for Tensile Properties of Plastics, ASTM Standard D638-08*, 2008.

[9] R. R. Rhinehart, "Optimization applications." class notes for MAE5703, Department of Mechanical and Aerospace Engineering, Oklahoma State University at Stillwater, October 2010.

[10] V. Padmanabhan and R. R. Rhinehart, "Evaluation of a novel stopping criterion for optimization," *International Association of Science and Technology for Development*, 2008. Paper 622-045.

[11] R. N. Tantaris, *Stability, performance, and robustness using first order controllers*. Ph.D. dissertation, Vanderbilt University, Nashville, TN, May 2004.

[12] M. Ponjanda-Madappa and P. R. Pagilla, "Tensile testing of flooring materials," tech. rep., OCAST Year 1 Project No.: AR091-037, Oklahoma State University, May 2010.

[13] B. Feiertag, "An applications seminar on web handling," Web Handling Research Center, September 2005.

VITA

Benjamin Robert Pacini

Candidate for the Degree of

Master of Science

Thesis: ANALYSIS OF THE UNWIND SECTION OF AN INDUSTRIAL WEB PROCESSING LINE

Major Field: Mechanical and Aerospace Engineering

Biographical:

Personal Data: Born in Columbus, OH, USA on March 7, 1986.

Education:

Received the B.S. degree from University of Colorado at Colorado Springs, Colorado Springs, CO, USA, 2008, in Mechanical and Aerospace Engineering

Completed the requirements for the degree of Master of Science with a major in Mechanical and Aerospace Engineering at Oklahoma State University in May, 2011.

Experience:

Research Assistant at Oklahoma State University from August 2009 to June 2011; Teaching Assistant at Oklahoma State University from August 2009 to May 2011; Engineering Intern at Goodrich Corporation from May 2008 to April 2009 and from May 2007 to August 2007.

Name: Benjamin Robert Pacini Date of Degree: July, 2011

Institution: Oklahoma State University Location: Stillwater, Oklahoma

Title of Study: ANALYSIS OF THE UNWIND SECTION OF AN INDUSTRIAL WEB PROCESSING LINE

Pages in Study: 163 Candidate for the Degree of Master of Science

Major Field: Mechanical and Aerospace Engineering

Scope and Method of Study: The purpose of this thesis is to analyze the control strategies and tension performance of the unwind section of an industrial web processing line that manufactures composite flooring materials. The main elements of the unwind section of the web line include a torque controlled unwind roll, two driven rollers, an accumulator, and a dancer. Dynamic models describing the interaction and control of these web line elements are derived and used to generate improvements to the existing control strategies. The controller structures used are the Proportional-Integral-Derivative type. Experiments are conducted on the improved strategies for the unwind roll to verify their performance. A comparison between a torque controlled unwind roll and a velocity controlled unwind roll is performed. The basis of comparison is the stability regions in their corresponding controller parameter spaces.

Findings and Conclusions: Comparing model simulation results and measured data verifies that the model adequately predicts trends measured in the unwind section. Model simulations and experimentation using the improved unwind roll strategies show improved tension regulation performance. However, it is seen that the variability and inconsistency in the braking mechanisms may limit the effectiveness of these improvements. Simulation results indicate that the modified control strategy for the first pull roll and accumulator also increased tension regulation performance. The analysis of the stability regions for the torque controlled unwind roll and velocity controlled unwind roll show that there is a greater flexibility in selecting the controller gains for the velocity controlled unwind.

ADVISOR'S APPROVAL: _____